

# **The Mechanism of Anticaking Agents for Sodium Chloride**

## **Proefschrift**

ter verkrijging van de graad van doctor  
aan de Radboud Universiteit Nijmegen  
op gezag van de rector magnificus prof. mr. S.C.J.J. Kortmann,  
volgens besluit van het college van decanen  
in het openbaar te verdedigen op donderdag 31 oktober 2013  
om 13.00 uur precies

Door

**Arno Alfred Christiaan Bode**

geboren op 12 december 1981  
te Eindhoven

**Promotor:**

Prof. dr. E. Vlieg

**Copromotoren:**

Dr. W.J.P. van Enkevort

Dr. J.A.M. Meijer (Akzo Nobel)

**Manuscriptcommissie:**

Prof. dr. ir. G.C. Groenenboom

Dr. ir. R. Geertman

Prof. dr. G.J. Witkamp (TU Delft)

©Arno A.C. Bode, 2013

Coverdesign by Silvie A. Meeuwissen

Printed by Ipskamp Drukkers, Enschede, The Netherlands

“The mind is not a vessel to be filled,  
but a fire to be kindled”

– *Plutarch*



# Contents

<b>1</b>	<b>Introduction</b>	<b>7</b>
1.1	Sodium Chloride . . . . .	9
1.2	Goal of the Thesis . . . . .	10
1.3	Habit Modifiers . . . . .	11
1.4	Caking of Crystalline Powders . . . . .	13
1.5	Anticaking Agents for Sodium Chloride . . . . .	14
1.6	The Applied Techniques . . . . .	15
1.7	In this thesis . . . . .	19
<b>2</b>	<b>The anticaking activity of ferrocyanide on sodium chloride explained by charge mismatch</b>	<b>25</b>
2.1	Introduction . . . . .	26
2.2	Experimental . . . . .	27
2.3	Results and Model . . . . .	29
2.4	Discussion . . . . .	34
2.5	Conclusion . . . . .	37
<b>3</b>	<b>Growth inhibition of sodium chloride crystals by anticaking agents: in-situ observation of step pinning</b>	<b>41</b>
3.1	Introduction . . . . .	42
3.2	Experimental . . . . .	45
3.3	Results and Discussion . . . . .	47
3.4	Conclusions . . . . .	60
<b>4</b>	<b>Structure and activity of the anticaking agent iron-(III) <i>meso</i>-tartrate</b>	<b>65</b>
4.1	Introduction . . . . .	66
4.2	Experimental . . . . .	68

4.3	Results and Discussion . . . . .	69
4.4	Conclusion and Outlook . . . . .	82
4.5	Appendix . . . . .	86
<b>5</b>	<b>Influence of anticaking agents on the caking of sodium chloride at the powder and two-crystal scale</b>	<b>87</b>
5.1	Introduction . . . . .	88
5.2	Experimental . . . . .	89
5.3	Results . . . . .	95
5.4	Discussion . . . . .	99
5.5	Conclusion . . . . .	101
<b>6</b>	<b>Sodium Chloride Dihydrate Crystals: Morphology, Nucleation, Growth and Inhibition</b>	<b>105</b>
6.1	Introduction . . . . .	106
6.2	Experimental . . . . .	108
6.3	Results and Discussion . . . . .	114
6.4	Conclusion . . . . .	128
<b>7</b>	<b>Summary</b>	<b>133</b>
<b>8</b>	<b>Samenvatting</b>	<b>135</b>
<b>9</b>	<b>Dankwoord</b>	<b>139</b>
<b>10</b>	<b>List of Publications</b>	<b>143</b>
<b>11</b>	<b>Curriculum Vitae</b>	<b>145</b>

## Chapter 1

# Introduction

Crystals have fascinated mankind for ages because of their geometrically perfect shapes, shiny facets and often colourful appearances. This made jewellery their main application in the past. In addition, throughout history both protective and healing powers have been attributed to crystals, at least since the ancient Egyptians. However, serious scientific studies on the origin and structure of crystals did not start until the 17<sup>th</sup> century.

Presently, crystals are used extensively in science and technology, food and pharmacology. Even though large single crystals have applications in, for instance, the semiconductor industry, most crystals are used as crystalline powder materials. In such materials, each particle is a small single crystal and the material does not have the alluring appearance as many single crystals do. Even though crystals are used extensively and their origin is well understood, the ancient lure of single crystals remains and therefore their use as jewels, and even the belief in their protective and healing powers, persists.



FIGURE 1.1: *Ancient and modern use of crystals: a ruby, a Roman ring set with diamonds, crystalline medical pills and crystalline salt.*

## 1.1 Sodium Chloride

Sodium chloride is a good example of a crystalline material. Historically, salt was a scarce and expensive commodity since it allowed the conservation of foods, while it could only be obtained by evaporating salt water. The production and trade in salt are very old and date back to at least 4000 BC. It is thought that Roman soldiers were at certain times even paid in salt and the word 'salary' is derived from 'sal', the Latin word for salt. Salt was strongly linked to wealth, so Strabo was very much surprised when he described the Arabian town of Gerrha, where he said that citizens built their houses out of salt delved from the salty soil, and repaired their houses using water to 'cake' pieces of salt back against the walls [1]. Pliny the Elder even said that the towers of its city walls were built out of salt blocks [2]. However, though the hot and dry climate of Arabia makes the story quite credible, it could also be that these stories were merely a metaphor for the wealth of this city.

Salt was also important in rituals in the Near East, like salting the soil of conquered cities, a practice starting with the Assyrians [3]. However, this act was completely symbolic, since the amounts required to poison farmlands are completely unfeasible. It was however not a Roman practice, and no historical sources exist suggesting that the Romans ever salted the soil of Carthage, a tale invented in the 19<sup>th</sup> century [4].

Salt is typically a powder, consisting of cubic crystalline particles of about 300  $\mu\text{m}$  in size [6] (see Figure 1.2 [5]). Nowadays, it is a very important raw material for the chemical industry, mainly as a source of chlorine gas. It is abundant in nature as it is the major part of dissolved material in sea water and it also occurs in bedrock, at sites of ancient seas that have disappeared. Sodium chloride is also important in biology, for instance, it is an essential component of all body fluids and it is an electrolyte in brain cell activity. It is therefore a vital component of our diet.

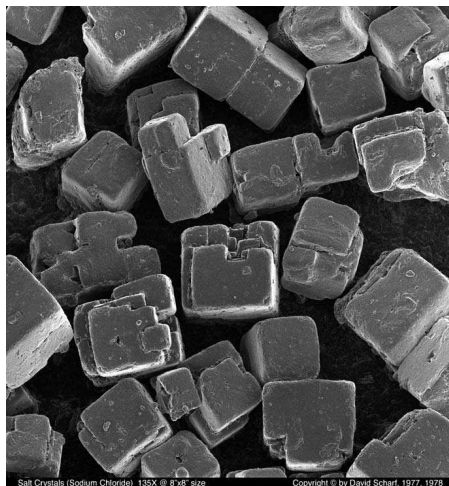


FIGURE 1.2: *Scanning electron micrograph of table salt. From D. Scharf [5].*

There is also a dihydrate form of sodium chloride, ( $\text{NaCl} \cdot 2\text{H}_2\text{O}$ ), next to the well known cubic anhydrous form ( $\text{NaCl}$ ). This dihydrate form is stable in presence of water in freezing conditions, that is at temperatures below  $0.1^\circ\text{C}$ , as is shown in figure 1.3. The crystalline form of the anhydrate is also known as halite and rock salt, while the dihydrate is also known as hydrohalite.

## 1.2 Goal of the Thesis

In this thesis, the advances made in academic research and modern analytical techniques are applied to explain the influence of additives on crystal powder properties at a more fundamental level. We will focus on additives which reduce the caking of powders, i.e. agglomeration or lump formation, so called anticaking agents. Furthermore, because of industrial relevance, our crystalline model systems are sodium chloride and sodium chloride dihydrate. The emphasis is on two anticaking agents for sodium chloride: ferrocyanide and iron(III) *meso*-tartaric acid.

The known anticaking agents for sodium chloride have very different properties: some are transition metal complexes, while others are metal ions or organic molecules. Several different molecular

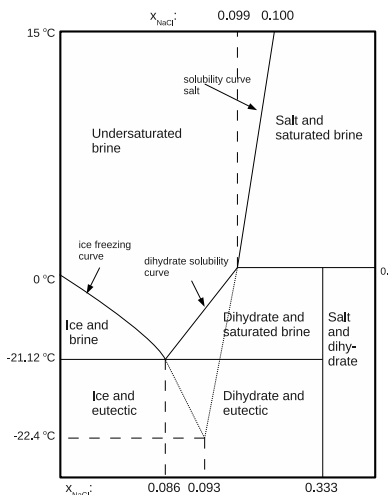


FIGURE 1.3: The phase diagram for the binary water – sodium chloride system. Sodium chloride dihydrate is the stable solid of sodium chloride at temperatures below 0.1 °C.

mechanisms must therefore be at work. The long-term goal is to find an underlying general mechanism by studying some of these additives in detail.

### 1.3 Habit Modifiers

Over the last two centuries, great advances were made in research regarding the growth of crystals. Their growth mechanism is now well understood, as well as the origin of their morphology. Also the influence of impurities on crystal growth has been studied in detail [7]. If added on purpose, such impurities are called additives or, in more technical studies, admixtures. An important class of additives are crystal habit modifiers. The first example of a crystal habit modifier was already reported in the 18<sup>th</sup> century by Romé de l'Isle [8]. Since then, this phenomenon has been explained by crystal growth theory: molecules of the habit modifier are assumed to adsorb differently on the various facets of a crystal, thereby changing the relative growth rates of the crystal facets. Since the relative growth rates of the various crystal facets

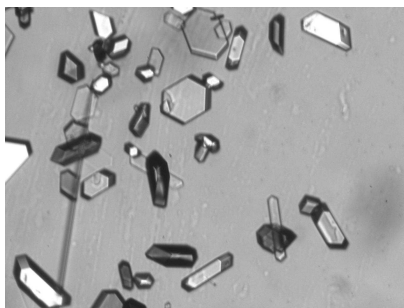


FIGURE 1.4: *Typical shape of sodium chloride dihydrate crystals ( $\text{NaCl}\cdot 2\text{H}_2\text{O}$ ).*

determine the crystal morphology, the habit modifiers cause morphological changes of the grown crystals [9, 10]. However, direct experimental proof of this theory exists only for very few cases [11].

On the other hand, great advances were made in technological applications of crystals during the last century, often in the form of crystalline powders. In technology, the use of admixtures in crystallisation processes was studied extensively because of their influence on material properties. These admixtures influence various powder properties, including flowability, particle size distributions, particle shapes and caking properties [12].

One of the very first examples of a crystal habit modifier reported concerned sodium chloride crystals. In the presence of urea, their habit changes from cubic to octahedral [8]. Since then, many other habit modifiers for sodium chloride have been reported, like chromium chloride [13], manganese, zinc and cadmium chloride [14] and formamide [15]. Many of these were studied in more detail in the 1950's and 1960's [16–18].

Even though the terminology is very different in the two distinct fields of academics and engineering, essentially they study the same phenomenon, be it on a different scale.

## 1.4 Caking of Crystalline Powders

Caking is the process in which a free-flowing powder is transformed into big lumps of solid material, due to agglomeration of the powder particles. This is usually caused by solid bridge formation between particles, though other causes for caking are known [19]. For sodium chloride, solid bridge formation is the major mechanism for caking. Such solid bridges are formed by partial dissolution of the powder material and subsequent recrystallisation in contact areas (see Figure 1.5). This can be caused by temperature and/or humidity variations [20, 21]. Due to its high solubility and high hygroscopicity, sodium chloride powders have a strong tendency to cake [22]. Since caking results in major problems when large quantities are handled, anticaking agents are used to prevent caking. In general, these anticaking agents retard crystal growth [23], thereby preventing solid bridge formation and thus caking.

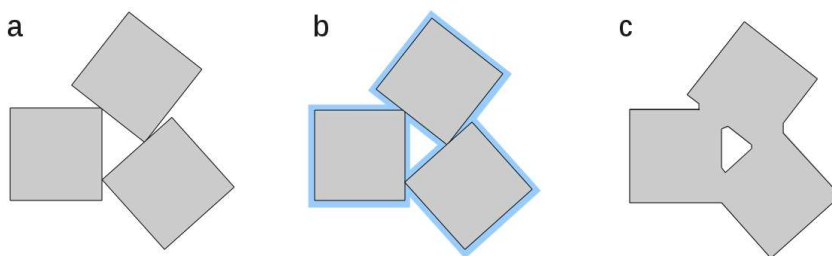


FIGURE 1.5: *Caking induced by solid bridge formation. a) Particles are free-flowing. b) Water is attracted in high humidity conditions and the crystals are slightly dissolved. c) In dry conditions the attracted water is evaporated again. Dissolved material recrystallises at contact points, forming solid bridges: the powder is caked.*

Since anticaking agents retard crystal growth differently for different facets, they are often also crystal habit modifiers. Usually, they inhibit the growth of one or a few crystal faces. This is because the molecules of the anticaking agent interact differently with different crystal faces.

## 1.5 Anticaking Agents for Sodium Chloride

Its high abundance and low price make sodium chloride the major source of chlorine gas, using electrolysis. Therefore, about 250 million tonnes of sodium chloride are produced, stored and shipped annually, creating a high demand of effective anticaking agents for sodium chloride. Because of this demand, many effective anticaking agents are known.

In 1965, a detailed study of the influence of several anticaking agents for sodium chloride was performed [24]. These anticaking agents were sodium and potassium ferrocyanide, nitrilotriacetamide, cadmium chloride and sodium metaphosphate. Their influence on the growth rate, nucleation rate and morphology of sodium chloride crystals was studied. All these anticaking agents also change the habit of sodium chloride crystals.

Parallel to that study, the anticaking agent ferricyanide was studied and the results were compared to ferrocyanide [18]. Though the ions are very similar, ferricyanide is reported to be less effective as an anticaking agent than ferrocyanide.

Ferrocyanide is a very effective anticaking agent for sodium chloride and has been used since the 1950's. However, ferrocyanide has a number of drawbacks. Because of its stability and charge, it is difficult to separate from a sodium chloride solution. During electrolysis, ferrocyanide causes degradation of the electrodes and membrane due to the formation of iron hydroxide (rust). This increases power consumption by the electrolysis cell and also increases maintenance costs. Furthermore, since ferrocyanide contains nitrogen, it is a source of the explosive gas nitrogen trichloride.

Because of these drawbacks, improved anticaking agents are needed. Recently, iron(III) *meso*-tartaric acid was introduced as an anticaking agent for sodium chloride [25]. This anticaking agent is nearly as effective as ferrocyanide. However, it does not contain nitrogen, so no nitrogen trichloride is formed from it. Furthermore, because the complex is less stable than ferrocyanide it can

more easily be removed from the brine prior to electrolysis. It was proposed that the complex forms an iron oxochloride layer and an iron oxide layer on top of the sodium chloride crystal, which inhibit crystal growth [26].

## 1.6 The Applied Techniques

Most studies on anticaking agents and habit modifiers mentioned above only concerned the influence of the compounds on macroscopic or even bulk properties of sodium chloride crystals and powders. Such properties are crystal growth rate, crystal morphology, nucleation rate, caking strength and flowability. In many cases, the influence of the additive is explained by the occurrence of an adsorption layer of the compound on the sodium chloride crystal. However, only very few studies actually found an adsorption layer. In the case of cadmium chloride, a layer of cadmium ions was found on the sodium chloride  $\{111\}$  surface using surface X-ray diffraction [27]. For formamide no adsorption layer of formamide could be identified [11].

Since experimental techniques to determine adsorption layers in solid-liquid systems are scarce, molecular modelling has been applied [28–30]. However, due to the ionic nature of the sodium chloride crystal and many of the additives used, long range interactions between ions are important. This makes modelling of these systems difficult, because most force fields are unreliable for these interactions. This makes the results of several of such studies debatable.

On the other hand, over the past decades a number of new techniques have been developed, which can be applied to study the structure and morphology of surfaces in liquid-solid systems. The techniques applied in this study include atomic force microscopy (AFM) and surface X-ray diffraction (SXRD).

Several other techniques have been used as well. Optical polarisation microscopy was applied to study the growth rates of sodium

chloride dihydrate crystals. To determine the molecular structure of the iron(III) *meso*-tartaric acid anticaking agent, electron paramagnetic resonance (EPR) and magnetic susceptibility measurements were performed, as well as computational modelling methods. A rheometer flow analyser was used in order to determine flowability properties of powders, while the caking strength between individual crystals was measured using a balance and pulley.

### 1.6.1 Atomic Force Microscopy

Atomic Force Microscopy (AFM) is a technique in which a surface is scanned by a very sharp tip, while the interaction force between the tip and the surface is monitored. It was developed in 1986 [31] as an adaptation of the scanning tunnelling microscope (STM) [32, 33]. In contrast to the STM, which requires the substrate of interest to be electrically conductive, the AFM can also be operated on insulator surfaces.

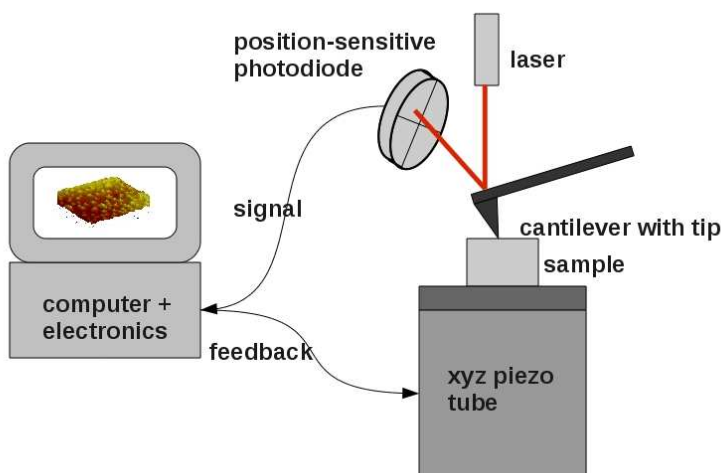


FIGURE 1.6: The basic principle of the Atomic Force Microscope (AFM).

Figure 1.6 shows the basic principle of an AFM. While scanning, the deflection of the tip is monitored by a laser beam, reflected from the back of the cantilever-tip combination onto a position sensi-

tive photodetector. This quadrant photodetector consists of four photodiodes arranged side-by-side. The relative signals of these photodiodes are a measure for the location of the reflected laser spot, and therefore of the angular deflection and torsion angle of the cantiliver, which is a measure for the tip-surface interaction force. This signal is recorded simultaneously with the position of the tip, giving a topographical image of the surface. When an AFM is operated in constant force mode, the force between the tip and surface is kept constant during scanning by varying the sample height. The image obtained in this way has a height resolution in the subnanometer range. The lateral resolution is a little lower, although atomic resolution images have been obtained using AFM.

### 1.6.2 Surface X-Ray Diffraction

Surface X-ray diffraction is a technique used to determine the structure of the surface layer of a crystalline material and of liquid-solid interfaces [34, 35]. The technique is in principle very similar to crystal structure determination by X-ray diffraction. However, since only the top most layers of atoms are of interest, which correspond to only a very small fraction of all atoms present, a very strong X-ray source is required. Otherwise, the weak signal from the surface is too weak compared to the much stronger signal from the crystal bulk. Such intense X-ray radiation is only available at synchrotron light sources.

The surface layers of a crystalline material create a weak signal of diffuse X-ray intensity perpendicular to the surface, so called crystal truncation rods. These rods connect the bulk Bragg reflections and their shape is determined by the structure of the surface layers, see Figure 1.7. By measuring the intensity of the crystal truncation rods, the structure of the surface can be determined [36].

The central rod, the (00) or specular rod, performs a special role as it is only sensitive to ordering in the direction perpendicular to the surface. Therefore, it is also sensitive to liquid layers that are only ordered in the out of plane direction. Such layers do not

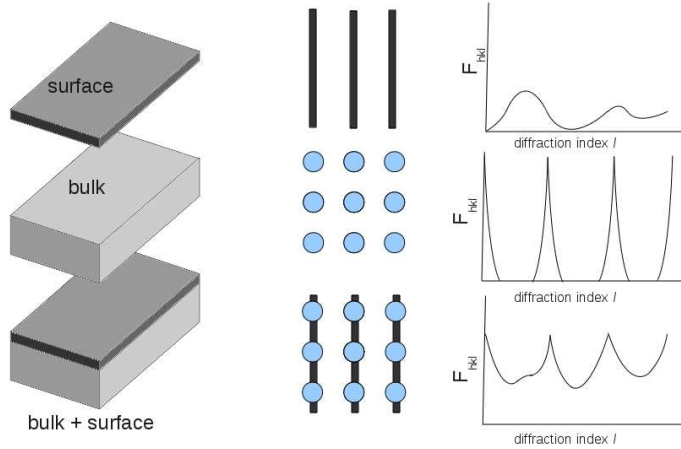


FIGURE 1.7: Diffraction from the 2D surface layer results in rods in reciprocal space (top), while diffraction from the bulk results in Bragg peaks (middle). The combination of the two signals results in crystal truncation rods (bottom).

contribute to the other rods. Only layers with some degree of in-plane ordering contribute to the non-specular rods.

### 1.6.3 Electron Paramagnetic Resonance

Electron Paramagnetic Resonance (EPR, also known as Electron Spin Resonance (ESR)) is a technique which is in principle very comparable to Nuclear Magnetic Resonance (NMR). Both methods study the spin resonance frequencies of a material to an external electromagnetic field. In NMR, the resonance of nuclear spins is studied, while EPR studies the resonance of electron spins. [37]

This resonance is based on Zeeman splitting: if an external magnetic field is present, the energy of the two allowed spin states of the electron is split. Alignment parallel to the field is lowered in energy, the ground state, while the antiparallel alignment is raised in energy and becomes an excited state, as is shown in Figure 1.8 for a free electron.

The exact energy of transition between the two states also depends on the environment of the electron, comparable to the chem-

ical shift in NMR. In EPR, the energy of the transition is measured as a function of the magnetic field strength. Traditionally, not the direct signal versus the field strength, but its first derivative is reported in EPR graphs. This was originally due to an enhanced signal to noise ratio of the detection method [37]. Nowadays, the first derivative is still used, because changes in slope are exaggerated in a derivative curve, making subtle differences more easily visible.

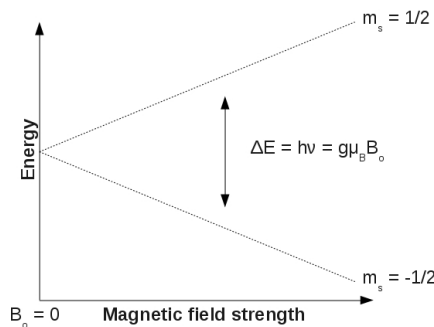


FIGURE 1.8: Zeeman splitting: the energies of the two allowed spin states of a free electron are a function of the external magnetic field strength.

In contrast to NMR, EPR can only be applied on systems containing unpaired electrons, limiting its application. On the other hand, it is very specific since only chemicals with an unpaired electron will show up in an EPR spectrum. The spectrum will contain information about the environment and symmetry around an atom containing an unpaired electron. Furthermore, since NMR signals are broadened by unpaired electrons, NMR on paramagnetic systems is oftenly not useful, and EPR can be used instead [38].

## 1.7 In this thesis

This thesis studies several aspects of anticaking agents for sodium chloride. Each chapter elaborates on a different aspect, like the adsorption mechanism, crystal growth inhibition and the influence on caking.

Chapter 2 shows how the anticaking agent ferrocyanide is adsorbed onto the crystal surface of sodium chloride. This adsorption mechanism was determined by studying the surface of these crystals using surface X-ray diffraction. It was concluded that the shape of the ferrocyanide ion fits into the crystal lattice of sodium chloride, while its charge does not match the ions it replaces.

The inhibition of crystal growth of sodium chloride crystals is discussed in chapter 3. Using atomic force microscopy, it is shown that the anticaking agents inhibit the step flow across the crystal surface by adsorbing onto it and subsequently pinning the steps.

A structure of the iron(III) *meso*-tartaric acid complex is proposed in chapter 4, based on experimental data and molecular modelling. Based on this structure, an adsorption mechanism is proposed for the interaction between this complex and the sodium chloride surface.

In chapter 5 it is shown that anticaking agents have the same effect on single crystals as on powders of sodium chloride, by measuring the cake strength. From this we conclude that the results from chapter 2 and 3, which were obtained on single crystals, are also relevant at the powder scale.

In the final chapter we focus on the dihydrate of sodium chloride. The crystal structure and morphology of this crystal are determined, as well as the growth and nucleation rate. Finally, we studied the interaction of anticaking agents on the growth and nucleation rate of dihydrate crystals.

## References

- [1] Strabo. *Geography*, volume XVI, chapter 2, pages 19–20. (7 BC – 23 AD).
- [2] Pliny the Elder. *Natural History*, volume VI, page 32. (77 – 79 AD).

- [3] M.W. Chavalas. *Ancient Near East: Historical Sources in Translation*, pages 144–145. Wiley, Hoboken, NJ, USA, (2006).
- [4] R.T. Ridley. *Classical Philology*, (1986), **81**, 140–146.
- [5] D. Scharf. *Magnifications, Photography with the Scanning Electron Microscope*. Schocken Books, New York, NY, USA, (1977).
- [6] G.E. Ewing. *Intermolecular Forces and Clusters II*, volume 116 of *Structure and Bonding*, pages 1–25. Springer Verlag, Berlin, (2005).
- [7] K. Sangwal. *Additives and Crystallization Processes*. Wiley, (2007).
- [8] J.B.L. de Romé de L’Isle. *Cristallographie*, page 379. Paris, (1783).
- [9] N. Cabrera and D.A. Vermilyea. The growth of crystals from solution. In R.H. Doremus, B.W. Roberts, and D. Turnbull, editors, *Growth and Perfection of Crystals*, pages 393–410. Wiley, (1958).
- [10] R. Lacmann and I.N. Stranski. The effect of adsorption of impurities on the equilibrium and growth forms of crystals. In R.H. Doremus, B.W. Roberts, and D. Turnbull, editors, *Growth and Perfection of Crystals*, pages 427–440. Wiley, (1958).
- [11] N. Radenovic, D.M. Kaminski, W.J.P. van Enckevort, W.S. Graswinckel, I.A. Shah, M. in ’t Veld, R.E. Algra, and E. Vlieg. *J. Chem. Phys.*, (2006), **124**, 164706.
- [12] J. Nývlt and J. Ulrich. *Admixtures in Crystallization*. VCH, (1995).
- [13] J.W. Retgers. *Z. Physik. Chem.*, (1892), **9**, 267.
- [14] L. Royer. *Compt. rend.*, (1934), **198**, 585.
- [15] F. Gille and K. Spangenberg. *Z. Krist. Miner. Petrograd A*, (1927), **65**, 204.

- [16] R. Kern. *Bull. Soc. Fr. Mineral Crist.*, (1953), **76**, 391.
- [17] M. Bienfait, R. Boistelle, and R. Kern. volume 152, page 577. Centre National de la Recherche Scientifique.
- [18] R. Boistelle. *Contribution à la connaissance des formes de croissance du chlorure de sodium*. PhD thesis, Université de Nancy, (1966).
- [19] H. Rumpf. *Chem-Ing-Tech*, (1958), **30**, 144–158.
- [20] F.G. Donnan. *Trans. Faraday Soc.*, (1918), **14**, 12.
- [21] T.M. Lowry and F.C. Hemmings. *J. Soc. Chem. Ind. (London)*, (1920), **39**, 101T.
- [22] D.W. Kaufmann. *Sodium Chloride: the production and properties of salt and brine*. Reinhold, (1960).
- [23] Y.L. Chen and J.Y. Chou. *Powder Technol.*, (1993), **77**, 1–6.
- [24] M.A. van Damme-van Weele. *Influence of additives on the growth and dissolution of sodium chloride crystals*. PhD thesis, Technische Hogeschool Twente, Enschede, (1965).
- [25] R.M. Geertman. Use of carbohydrate-based metal complexes in non-caking salt compositions. US patent WO 00/59828, (2006).
- [26] R.M. Geertman. *VDI-Berichte*, (2005), **1901**, 557–562.
- [27] N. Radenovic, W.J.P. van Enckevort, D.M. Kaminski, M.C.R. Heijna, and E. Vlieg. *Surf. Sci.*, (2005), **599**, 196–206.
- [28] A. Singh and B. Ganguly. *Mol. Simul.*, (2008), **34**, 973–979.
- [29] A. Singh, M.K. Kesharwani, and B. Ganguly. *Cryst. Growth Des.*, (2009), **9**, 77–81.
- [30] A. Singh, S. Sen, and B. Ganguly. *J. Mol. Graph. Model.*, (2010), **28**, 413–419.
- [31] G. Binnig, C.F. Quate, and Ch. Gerber. *Phys. Rev. Lett.*, (1986), **56**, 930–933.

- [32] G. Binnig and H. Rohrer. *Helv. Phys. Acta*, (1982), **55**, 726.
- [33] G. Binnig, H. Rohrer, Ch. Gerber, and E. Weibel. *Phys. Rev. Lett.*, (1983), **50**, 120.
- [34] R. Feidenhans'l. *Surf. Sci. Rep.*, (1989), **10**, 105.
- [35] I.K. Robinson and D.J. Tweet. *Rep. on Prog. Phys.*, (1992), **55**, 599–651.
- [36] E. Vlieg. *Surf. Sci.*, (2002), **500**, 458–474.
- [37] L.D. Tuck. *J. Pharm. Sci.*, (1964), **53**, 1437–1445.
- [38] R.H. Crabtree. *The Organometallic Chemistry of the Transition Metals*. Wiley, Hoboken, NJ, USA, (2005).



## Chapter 2

# The anticaking activity of ferrocyanide on sodium chloride explained by charge mismatch

*Arno A.C. Bode, Vedran Vonk, Fieke J. van den Bruel, Dirk J. Kok, Anne M. Kerkenaar, Miguel F. Mantilla, Shanfeng Jiang, Jan A.M. Meijer, Willem J.P. van Enckevort and Elias Vlieg*

### Abstract

Sodium chloride crystals have a strong tendency to cake, which can be prevented by treating them with the anticaking agent ferrocyanide. Using surface X-ray diffraction, we show how the ferrocyanide ion sorbs onto the {100} face of the sodium chloride crystal where it replaces a sodium ion and five surrounding chloride ions. The coverage is about 50%. Based on the determined atomic structure, we propose the following anticaking mechanism. Because of the charge of the ferrocyanide ions sorbed on the surface, the crystal can only continue growing by leaving an energetically unfavourable sodium vacancy, or by desorbing the ferrocyanide ion. Therefore, the ferrocyanide effectively blocks further growth of sodium chloride crystals, thereby preventing them from agglomerating and caking.

## 2.1 Introduction

When left untreated, powders of sodium chloride (NaCl) will agglomerate, resulting in lump formation. This process is called caking. Caking causes major problems when handling large quantities and is therefore prevented by applying an anticaking agent [1]. Anticaking agents are generally assumed to be crystal growth inhibitors, preventing crystals from growing together and agglomerating [2]. Often, anticaking agents also act as crystal nucleation inhibitors and crystal habit modifiers because these three phenomena are all caused by crystal growth inhibition. For NaCl, many of these habit modifiers are known [3]. Already in 1783, Romé de L'Isle reported that urea changes the habit of NaCl crystals from cubic to octahedral [4]. Other crystal habit modifiers for sodium chloride are formamide and cadmium chloride. The interactions of these habit modifiers with sodium chloride crystals were extensively studied, both computationally and experimentally [5–10].

The most commonly used anticaking agent for sodium chloride is ferrocyanide,  $[\text{Fe}(\text{CN})_6]^{4-}$ . It has a very strong anticaking effect, but it also inhibits sodium chloride crystal growth and nucleation and modifies the sodium chloride crystal habit. Sodium chloride crystals grow dendritically in presence of even extremely small amounts of ferrocyanide. Because of this, ferrocyanide has also been used in construction materials to reduce damage caused by salt crystallisation in stones [11–13]. Although the influence of this anticaking agent on the crystallisation of NaCl was investigated in detail already in 1965 [14], the fundamental chemical interaction between the ferrocyanide ion and the sodium chloride crystal surface remains unknown.

In 1966, Boistelle *et al.* proposed a mechanism in which a ferrocyanide ion replaces a chloride ion on the  $\{100\}$  surface of NaCl [15]. In their model, one cyanide group replaces the chloride ion and the rest of the ferrocyanide ion sticks out of the crystal. They also assumed that the ferrocyanide ions would be ordered in-plane with four sodium ions per ferrocyanide ion, resembling an epitaxial layer of sodium ferrocyanide. The sorption layer they propose

seems, however, unlikely, since it would result in a charged surface. In 1974, Glasner and Zidon showed by calculation that the ferrocyanide ion has almost exactly the same shape and size as a  $[\text{NaCl}_6]^{5-}$  cluster [16]. The ferrocyanide ion fits therefore very well into the sodium chloride crystal lattice. They argued that a ferrocyanide ion could act as a heterogeneous nucleation site for sodium chloride crystals.

In 2005, Geertman [17] assumed that this good fit allows the ferrocyanide ion to sorb strongly onto the sodium chloride surface and can in this way block the growth of sodium chloride crystals. In this paper, we determine the sorption geometry of ferrocyanide ions on sodium chloride crystal using surface X-ray diffraction, leading to an atomic-scale understanding of the anticaking mechanism.

## 2.2 Experimental

Cubic NaCl crystals (dimensions approximately  $3 \times 3 \times 3 \text{ mm}^3$ ) were grown from a saturated sodium chloride solution, filtered using  $0.2 \mu\text{m}$  Whatman filters. Evaporation was minimised in order to keep the growth rate of the crystals as low as possible, because this results in the best crystals. After removing the crystals from the solution they were dried immediately using a paper tissue to prevent roughening. The resulting crystals were nearly optically defect-free and the cubic  $\{100\}$  surfaces were atomically flat with large terraces and step heights of only one atomic layer ( $2.8 \text{ \AA}$ ) as was verified by atomic force microscopy.

We used surface X-ray diffraction (SXRD) [18, 19] to determine the structure of the ferrocyanide ion on the sodium chloride crystal surface. This technique can be used to investigate the structure of crystal surfaces and sorption layers. SXRD has been used to determine the structure of the adsorbed water layer on the  $\{100\}$  NaCl crystal surface [20] and was also applied to determine the influence of cadmium ions on the growth and morphology of NaCl  $\{111\}$  crystal surfaces [6]. With SXRD, diffracted X-ray intensity is measured along crystal truncation rods [21]. These rods are tails

of diffuse intensity perpendicular to the substrate surface, connecting the bulk Bragg reflections. Their shape is determined by the atomic structure of the crystal surface.

The SXRD-experiments were performed at the beam line of the Max Planck Institute at the ANKA synchrotron in Karlsruhe, Germany and at the ID03 beamline at the ESRF synchrotron in Grenoble, France. The data used in the present analysis were obtained at the ANKA synchrotron. The radiation used had a photon energy of 10 keV. We measured data sets for a blank (100) NaCl crystal surface and a (100) NaCl surface treated with potassium ferrocyanide. The potassium ferrocyanide was applied in a droplet of methanol (12.5  $\mu$ l,  $1.9 \times 10^{-6}$  mol/l) to prevent roughening of the surface by the solvent. The methanol was allowed to evaporate prior to the measurements. The relative humidity (RH) of the environment was approximately 50%.

A set of different rods is needed to determine the structure of the surface completely. The momentum transfer  $\vec{Q}$  depends on the diffraction indices  $hkl$  and the reciprocal lattice vectors  $\vec{b}_i$ , as

$$\vec{Q} = h\vec{b}_1 + k\vec{b}_2 + l\vec{b}_3. \quad (2.1)$$

We choose the orientation of the unit cell such that  $l$  denotes the direction perpendicular to the surface and  $h$  and  $k$  denote the directions parallel to the  $a$  and  $b$  axis. Therefore, we formally study the NaCl(001) surface.

For each condition, blank and with ferrocyanide applied, a data set was acquired consisting of the (00), (11) and (20) rods. The momentum transfer of the (00) rod does not have an in-plane component and therefore this rod is only sensitive to the electron density perpendicular to the surface.

Integrated intensities at various points along the rods were determined by performing rocking scans and integrating the number of diffracted photons detected. The necessary geometrical and resolution corrections were applied to obtain structure factors from

the integrated intensities [22]. The programme ROD was used for fitting and model calculations [23]. The program was modified to take anomalous dispersion effects into account [24].

## 2.3 Results and Model

### 2.3.1 The model

The blank data set consists of 64 non-equivalent reflections and the ferrocyanide data set consists of 46 non-equivalent reflections. Figure 2.1 shows the data. To fit the blank data, the model of the water layers on  $\{100\}$  NaCl found by Arsic *et al.* was used [20]. In this model, oxygen atoms are used to describe the locations of ordered water molecules, since SXRD is not sensitive to hydrogen positions. They found that the water molecules in the first layer are positioned directly above the sodium ions, not above the chloride ions. Depending on the humidity, one to four layers of water molecules were found. In our experimental conditions, with 50% RH, we expect to find three layers of partially ordered water molecules. Water layers beyond the third layer are disordered and therefore invisible in this SXRD study. This model is shown in Figure 2.2a.

Based on the sorption mechanism proposed by Boistelle *et al.* [15] and the good size match of the ferrocyanide ion compared to the  $[\text{NaCl}_6]^{5-}$  cluster [16], the model by Arsic *et al.* was adapted to include sorbed ferrocyanide ions. These ferrocyanide ions are positioned with the iron atom at the sodium ion location, four cyanide ligands are pointing toward the four neighbouring chloride locations in the  $\{100\}$  surface. One cyanide ligand sticks down, replacing a chloride ion in the bulk crystal and one cyanide ligand sticks out into the water layers. The water molecules are still assumed to be positioned above the sodium ions, but some of their positions are now blocked by the cyanide ligands. This model is shown in Figure 2.2b. A top view of this model with the densest possible sorption layer of ferrocyanide ions is shown in Figure 2.2c. This figure shows that due to steric hindrance of the cyanide ligands, only one in four sodium ions at the surface can be re-

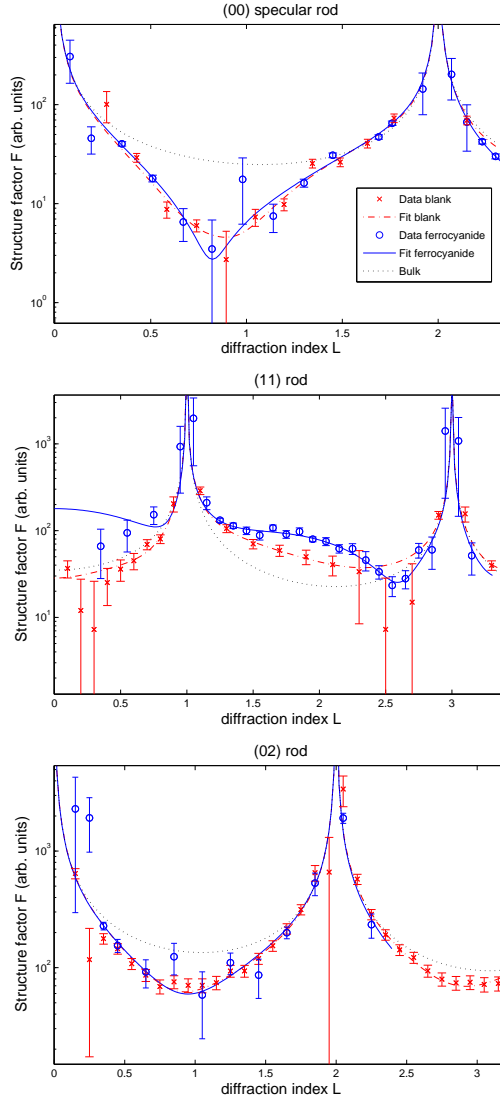


FIGURE 2.1: The specular (top), (11) (middle) and (02) (bottom) rods of  $\text{NaCl}(100)$ . The crosses represent the blank data set and the dash-dotted line represents the corresponding fit. The circles represent the ferrocyanide data set, while the solid line represents the fit to this data set. The dotted curves show calculations for a bulk-truncated surface.

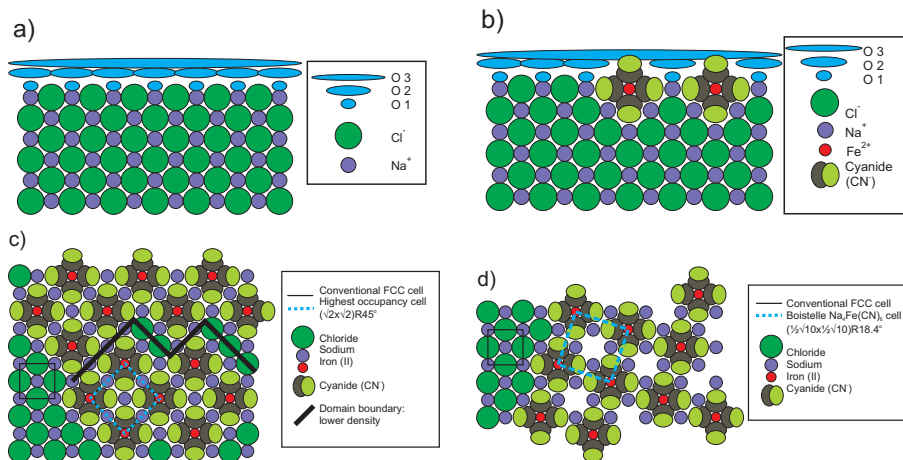


FIGURE 2.2: The models used to fit the data; (a) and (b) are side views, (c) and (d) are top views without the water layers. a) Blank {100} NaCl surface covered with three water layers, represented by oxygen (O) atoms. Water molecules are positioned on top of the sodium ions. b) Ferrocyanide ions sorbed on the sodium chloride surface: the iron atom is positioned at the sodium ion location, the cyanide ligands replace the five neighbouring chloride ions. c) Top view of the {100} surface of sodium chloride with the densest possible sorption layer of ferrocyanide ions. Due to steric hindrance of the cyanide ligands, at maximum one in four sodium ions can be replaced by an iron atom. Domain boundaries lower the density of the layer because of steric hindrance. d) Sorption layer proposed by Boistelle *et al.* [15]. Four sodium ions are sorbed per ferrocyanide ion, forming a superstructure resembling an epitaxial layer of sodium ferrocyanide Na<sub>4</sub>Fe(CN)<sub>6</sub>.

placed by a ferrocyanide ion. This densest layer forces the ions in a  $(\sqrt{2} \times \sqrt{2})\text{R}45^\circ$  reconstruction symmetry, the resulting ferrocyanide density of this layer is  $2.6 \cdot 10^{-6} \text{ mol/m}^2$ .

Also the model proposed by Boistelle *et al.* [15] was fitted to the data. In this model, for each sorbed ferrocyanide ion, also four sodium ions are adsorbed to form an epitaxial layer of sodium ferrocyanide on the sodium chloride crystal. A chloride location is left vacant. This model corresponds to a  $(\frac{1}{2}\sqrt{10} \times \frac{1}{2}\sqrt{10})\text{R}18.4^\circ$  reconstruction and is shown in Figure 2.2d.

In order to detect either of these reconstructions, a large section of reciprocal space in the in-plane direction was scanned at low  $l$  ( $l = 0.1$ ). In this way, at each point in reciprocal space between  $h = 0.2$ – $2.2$  and  $k = 0.2$ – $2.2$  the photon intensity was measured.

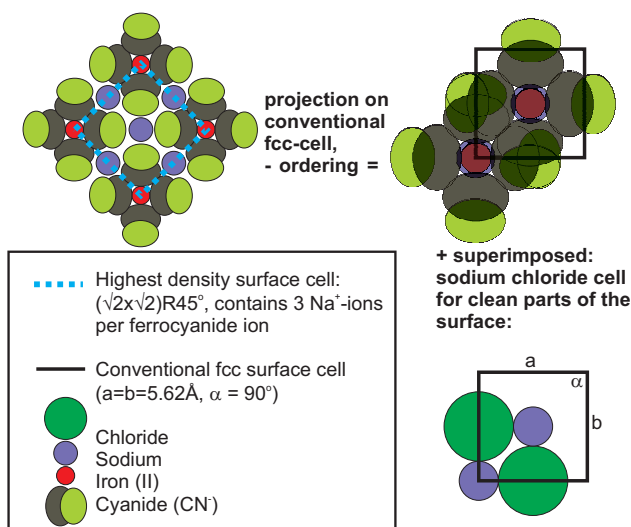


FIGURE 2.3: Unit cell used to fit the data. The conventional sodium chloride unit cell is used. Ferrocyanide ions are modelled superimposed on the sodium chloride ions, all with partial occupancy. The iron atoms of the ferrocyanide ions are at sodium locations and the cyanide groups at chloride locations.

No superstructure peaks were detected, showing that no significant long-range in-plane ordering of the ferrocyanide ions occurs. However, we can not exclude ordering in small domains, too small to be detected in this reciprocal space map.

Since we did not detect any superstructure reflections, we use a  $(1 \times 1)$  surface unit cell. The size of the ferrocyanide ions makes the real (local) unit cell larger than  $(1 \times 1)$ , but all ions in the model are projected onto this unit cell and the surface is modelled with overlapping atoms having partial occupancies. Due to packing considerations, the occupancy of ferrocyanide is less than one per unit cell. Because the conventional fcc unit cell is used, two equivalent positions for each type of atom exist in the model. The surface unit cell contains sodium and chloride ions at their bulk positions which are allowed to relax. Overlapping these atoms, ferrocyanide ions are placed with the iron atom at the sodium location, having their cyanide ligands at the chloride locations. This unit cell is shown in Figure 2.3. Two fitting parameters were used to describe the occupancies of these ions. One occupancy parameter,

$Occ_1$ , describes the sorbed ferrocyanide ions on the surface. To keep the total surface uncharged, each ferrocyanide ion requires three sodium ions, even though the charge of the ferrocyanide ion is  $4^-$ . This is because the cyanide group pointing down is already replacing a chloride ion and its charge is therefore already compensated by a sodium ion in that layer. This results in a  $3^-$  net charge for the top part of the ferrocyanide ion (see Figure 2.2b). Therefore, the occupancy of the ferrocyanide ions also represents three sodium ions at the surface. A second occupancy parameter,  $Occ_2$ , is used to model sodium and chloride ions at the surface if the sorption layer of the ferrocyanide ions is not completely filled. Since we found no in-plane ordering, we do not expect to find a completely filled layer, because domain boundaries result in a lower occupancy of ferrocyanide ions in this model, as shown in Figure 2.2c. Furthermore, because each position can only be occupied once, the two occupancies are related by,

$$Occ_1 + Occ_2 \leq 1. \quad (2.2)$$

### 2.3.2 Fitting results

In order to establish the quality and roughness of the starting surface, the blank data set was fitted using a  $\chi^2$  minimisation routine. Fit parameters were the horizontal and vertical positions of the oxygen atoms and the sodium and chloride ions in the top layer. For this data set,  $Occ_1$  was fixed at 0. Furthermore, in-plane and out of plane Debye–Waller (DW) parameters were fitted as a measure of disorder in these directions. Initial fits showed that the sodium and chloride ions assumed in-plane bulk lattice positions, as expected, so these parameters were fixed in further fitting steps. Only relaxation in the vertical direction was used as a fit parameter. No surface roughness parameter was needed to fit the data, demonstrating the high quality of our starting surface. We obtained a good fit result with a normalised  $\chi^2$  value of 1.29. The resulting fit is shown in Figure 2.1, the corresponding parameters are summarised in Table 2.1. The third water layer does not exhibit any lateral order, and therefore the  $DW_{\parallel}$  parameter for this layer was fixed at 500 (effectively infinite). The  $DW_{\perp}$  parameter of all water layers was fixed at 1, because the water molecules are as-

sumed to be layered [20]. These parameters are in good agreement with the results of Arsic *et al.* at a relative humidity of 45%.

Secondly, the ferrocyanide sorption model was fitted to the data, using the model described above (Figure 2.2c) and the unit cell described in Figure 2.3. Additional fitting parameters were the vertical and horizontal position of the ferrocyanide ions. The ferrocyanide ion itself was assumed to be rigid. Again, initial fits showed that the sodium, chloride and ferrocyanide ions assumed in-plane bulk positions, so these parameters were fixed in further fitting steps. A good fit result was obtained with a normalised  $\chi^2$  value of 1.19. The resulting fit parameters are summarised in Table 2.1, while the fit is shown in Figure 2.1. The signal from the ferrocyanide ions is observed most clearly in the extra intensity around  $l = 1.5$  in the (11) rod.

We also tried to fit the model proposed by Boistelle (Figure 2.2d) to the ferrocyanide data set. The fit result was quite poor compared to our best model, having a normalised  $\chi^2$  value of 2.02. The best fit parameters of the Boistelle model to the ferrocyanide data set are shown in the supplementary information, available online. We also tested whether the ferrocyanide data could be fitted with the blank model. This was not possible, the best fit obtained had a normalised  $\chi^2$  of 2.39 when physically acceptable parameter values were used.

## 2.4 Discussion

The best fit is obtained for the model we assumed from the beginning, in which the iron in the ferrocyanide ion assumes the sodium bulk position, with the cyanide ligands replacing the surrounding chloride ions. The droplet we applied contained approximately enough ferrocyanide ions for a full sorption layer on the top face of the crystal. Our results show an occupancy of  $52 \pm 12\%$ . This means that ferrocyanide strongly attaches to the surface, assuming that due to spreading of the methanol droplet over the crystal, some of the ions have sorbed on the side faces of the crystal. The

	Blank	Ferrocyanide
$\Delta z$ Na ( $\text{\AA}$ )	$0.02 \pm 0.02$	$0.3 \pm 0.17$
$\Delta z$ Cl ( $\text{\AA}$ )	$0.06 \pm 0.03$	$-0.16 \pm 0.18$
$\Delta z$ $[\text{Fe}(\text{CN})_6]^{4-}$ ( $\text{\AA}$ )	–	$-0.20 \pm 0.16$
Occupancy NaCl ( $\text{Occ}_1$ )	$0.87 \pm 0.02$	$0.19 \pm 0.06$
Occupancy $[\text{Fe}(\text{CN})_6]^{4-}$ ( $\text{Occ}_2$ )	0	$0.52 \pm 0.12$
$\Delta z$ $O_1$ ( $\text{\AA}$ )	$1.9 \pm 0.02$	$0.8 \pm 0.3$
$\Delta z$ $O_2$ ( $\text{\AA}$ )	$3.0 \pm 0.06$	$3.1 \pm 0.2$
$\Delta z$ $O_3$ ( $\text{\AA}$ )	$3.7 \pm 0.05$	$3.5 \pm 2.0$
$\text{DW}_{\parallel}(O_1)$	5	5
$\text{DW}_{\parallel}(O_2)$	53	70
$\text{DW}_{\parallel}(O_3)$	500	500
$\text{DW}_{\parallel}([\text{Fe}(\text{CN})_6]^{4-})$	–	1
$\text{DW}_{\perp}(O_1, O_2 \text{ and } O_3)$	1	1
Occupancy $O_1$	$0.56 \pm 0.15$	$0.9 \pm 0.3$
Occupancy $O_2$	$0.61 \pm 0.27$	$0.9 \pm 0.3$
Occupancy $O_3$	$1.0 \pm 0.01$	$0.4 \pm 0.3$
Total water occ.	2.2	2.2
$\chi^2$	1.29	1.19

TABLE 2.1: Summary of best fit parameters for the blank and ferrocyanide data sets.  $\Delta z$  is the position relative to a non-relaxed NaCl top layer, positive values indicate a position above this layer.  $O_1$ ,  $O_2$  and  $O_3$  denote the water layers as shown in Figures 2.2a and b. The Debye–Waller (DW) parameters are in  $\text{\AA}^2$ .

surface between the ferrocyanide ions and the charge neutralizing sodium ions is partially filled by sodium and chloride ions (19%). The top layer of the crystal is therefore not completely filled. This is in agreement with the results by Arsic *et al.*, who found occupancies of the top layer of sodium chloride of approximately 78% [20] at various conditions.

We did not find any in-plane ordering of the ferrocyanide ions, nor did we find an epitaxial layer of sodium or potassium ferrocyanide, as was predicted by Boistelle *et al.* [15]. Since the sorbed ferrocyanide ions are assumed to be immobile they do not rearrange at the surface. This inhibits the formation of large domains of an ordered epitaxial layer. This may also cause the lower than 100% occupancy, because overlap of the ferrocyanide ions is not possible and domain boundaries cause a lower occupancy.

This was tested by a simple Monte Carlo simulation in which ferrocyanide ions sorb onto the  $\{100\}$  surface of NaCl. In this simulation, a random sodium location is chosen for the sorption of a ferrocyanide ion. If the location is free and not sterically hindered by neighbouring ferrocyanide ions, the ferrocyanide ion is sorbed. The simulations showed that an occupancy of  $80\% \pm 3\%$  is reached, so under these conditions the domain boundaries take up about 20% of the surface. The experimental occupancy of 50% is thus caused by a combination of domain boundaries and a reduced concentration.

The structure of the water layers as compared to the blank surface is influenced somewhat by the ferrocyanide ions. There are still three ordered water layers, however, the distance of the first water layer to the crystal is changed. This water layer seems to be very close to the crystal surface ( $0.8 \text{ \AA}$ ). However, due to the large uncertainty in this value of  $0.3 \text{ \AA}$ , a physically more likely value of  $1.1 \text{ \AA}$  is possible. Also the occupancy of the water layers seems higher except for the third water layer. Their degree of in-plane ordering is not significantly changed. The higher occupancy of the water layers may be caused by a change of hygroscopicity of the surface because of an increase of the polarity of the crystal surface, due to the charge of the iron atom. However, the higher occupancy of the water layers could also be caused by a small variation of relative humidity.

The results show that the ferrocyanide ion,  $[\text{Fe}(\text{CN})_6]^{4-}$ , replaces a  $[\text{NaCl}_5]^{4-}$  cluster at the surface, thus maintaining charge neutrality, as proposed by Geertman [17]. The ferrocyanide ion has to be removed for growth to continue. Different from the case of other additives, like tailor-made additives [25–27], it is not the steric interaction of the additive that blocks crystal growth. Sterically, the ferrocyanide ion fits well in the NaCl lattice, the misfit is 0.9%. It is the charge difference that causes the blocking. Since the charge of the ferrocyanide ion,  $[\text{Fe}(\text{CN})_6]^{4-}$ , is lower than the charge of the  $[\text{NaCl}_6]^{5-}$  cluster it would replace in the bulk, a sodium vacancy is needed to keep the crystal electrically neutral. This is energetically unfavourable, and therefore the ferrocyanide ions will not be

incorporated into the sodium chloride crystal. This was confirmed in our laboratory by detailed chemical analysis of crystals grown in the presence of ferrocyanide ions.

Since the ferrocyanide ion is tightly bound, it will not desorb easily. Therefore, the crystals treated with ferrocyanide cannot grow, preventing them from agglomerating. This explains the anticaking activity of ferrocyanide.

## **2.5 Conclusion**

We have applied surface X-ray diffraction to study the sorption of ferrocyanide ions on sodium chloride crystals. Our experiments show how the ferrocyanide ion interacts with the sodium chloride crystal surface. Based on this interaction, a blocking mechanism for crystal growth of sodium chloride crystals by ferrocyanide is suggested. The ferrocyanide ions replace sodium chloride clusters on the surface and block further growth of the sodium chloride crystal due to a difference in ion charge. Since the crystals cannot grow, the formation of interparticle solid bridges is inhibited. This prevents caking of sodium chloride effectively.

## **Acknowledgement**

We would like to acknowledge the beamline staff of beamline ID03 at the European Synchrotron Radiation Facility (ESRF) for their kind assistance during measurements and the Max Planck Institute for Metals Research for the use of the ANKA beamline. Furthermore we would like to acknowledge Akzo Nobel Industrial Chemicals and the Dutch Ministry of Economic Affairs for funding (EOS-KTO program, AgentschapNL).

## **Supporting Information**

Table containing best fit parameters for the Boistelle model. This information is available free of charge via the Internet at <http://pubs.acs.org>.

## References

- [1] D.W. Kaufmann. *Sodium Chloride: the production and properties of salt and brine*. Reinhold, (1960).
- [2] Y.L. Chen and J.Y. Chou. *Powder Technol.*, (1993), **77**, 1–6.
- [3] J. Nývlt and J. Ulrich. *Admixtures in Crystallization*. VCH, (1995).
- [4] J.B.L. de Romé de L’Isle. *Cristallographie*, page 379. Paris, (1783).
- [5] N. Radenovic, W.J.P. van Enkevort, and E. Vlieg. *J. Cryst. Growth*, (2004), **263**, 544–551.
- [6] N. Radenovic, W.J.P. van Enkevort, D.M. Kaminski, M.C.R. Heijna, and E. Vlieg. *Surf. Sci.*, (2005), **599**, 196–206.
- [7] N. Radenovic, D.M. Kaminski, W.J.P. van Enkevort, W.S. Graswinckel, I.A. Shah, M. in ’t Veld, R.E. Algra, and E. Vlieg. *J. Chem. Phys.*, (2006), **124**, 164706.
- [8] A. Singh and B. Ganguly. *Mol. Simul.*, (2008), **34**, 973–979.
- [9] A. Singh, M.K. Kesharwani, and B. Ganguly. *Cryst. Growth Des.*, (2009), **9**, 77–81.
- [10] A. Singh, S. Sen, and B. Ganguly. *J. Mol. Graph. Model.*, (2010), **28**, 413–419.
- [11] C. Rodriguez-Navarro, L. Linares-Fernandez, E. Doehne, and E. Sebastian. *J. Cryst. Growth*, (2002), **243**, 503–516.
- [12] V.Y. Traskine, Z.N. Skvortsova, and A.E. Muralev. *Mat. Sci. Eng. A*, (2008), **495**, 132–137.
- [13] B. Lubelli and R.P.J. van Hees. *J. Cultural Herit.*, (2007), **8**, 223–234.
- [14] M.A. van Damme-van Weele. *Influence of additives on the growth and dissolution of sodium chloride crystals*. PhD thesis, Technische Hogeschool Twente, Enschede, (1965).

- [15] R. Boistelle. *Contribution à la connaissance des formes de croissance du chlorure de sodium*. PhD thesis, Université de Nancy, (1966).
- [16] A. Glasner and M. Zidon. *J. Cryst. Growth*, (1974), **21**, 294–304.
- [17] R.M. Geertman. *VDI-Berichte*, (2005), **1901**, 557–562.
- [18] R. Feidenhans'l. *Surf. Sci. Rep.*, (1989), **10**, 105.
- [19] I.K. Robinson and D.J. Tweet. *Rep. on Prog. Phys.*, (1992), **55**, 599–651.
- [20] J. Arsic, D.M. Kaminski, N. Radenovic, P. Poodt, W.S. Graswinckel, H.M. Cuppen, and E. Vlieg. *J. Chem. Phys.*, (2004), **120**, 9720–9724.
- [21] E. Vlieg. *Surf. Sci.*, (2002), **500**, 458–474.
- [22] E. Vlieg. *J. Appl. Chystallography*, (1997), **30**, 532.
- [23] E. Vlieg. *J. Appl. Crystallogr.*, (2000), **33**, 401–405.
- [24] V. Vonk. *J. App. Crystallogr.*, (2011), **44**, 1217–1221.
- [25] L. Addadi, J. Vanmil, E. Gati, and M. Lahav. *Origins Life Evol. B.*, (1981), **11**, 107–118.
- [26] I. Weissbuch, L. Addadi, M. Lahav, and L. Leiserowitz. *Science*, (1991), **253**, 637–645.
- [27] W.J.P. van Enkevort and J.H. Los. *J. Phys. Chem. C*, (2008), **112**, 6380–6389.



## Chapter 3

# Growth inhibition of sodium chloride crystals by anticaking agents: in-situ observation of step pinning

*Arno A.C. Bode, Shanfeng Jiang, Jan A.M. Meijer, Willem J.P.  
van Enkevort and Elias Vlieg*

### Abstract

We have determined how the growth of sodium chloride crystals is inhibited by the anticaking agents ferrocyanide and iron(III) *meso*-tartaric acid. Using in-situ atomic force microscopy, we show how steps flow on clean crystals and how the step flow is inhibited by the anticaking agents. At sub-monolayer coverages, steps are temporarily pinned, while at higher coverages, no step movement is observed at all. Finally, we found that the two anticaking agents influence the surface morphologies of crystals treated with them differently, providing a possible explanation of the observation that powders treated with ferrocyanide flow freely and those treated with iron *meso*-tartaric acid show slip-stick behaviour.

### 3.1 Introduction

Crystal growth inhibitors are intensively studied since they are important in many applications. They provide control over crystal shape and size distributions, like the prevention of the formation of needle-shaped crystals [1, 2]. They can also be used to prevent agglomeration of crystalline powders, i.e. caking [3]. In the case of the prevention of caking, the inhibitors are called anticaking agents [4].

However, their functioning is not well understood. In essence, two basic theories have been proposed, both assuming adsorption of the inhibitor molecules on the crystal surface: either individual molecules adsorb and block growth by step movement on the crystal surface [5], or the whole surface is covered by a "protecting" adsorption layer [6]. Only in a few cases it is known how a certain growth inhibitor adsorbs onto the crystal surface [7–9]. Here, we investigate the growth inhibition by two anticaking agents for sodium chloride powders, ferrocyanide ( $\text{K}_4\text{Fe}(\text{CN})_6$ ) and iron(III) *meso*-tartaric acid ( $\text{Fe-mTA}$ ; a 1:1 molar mixture of  $\text{FeCl}_3$  and *meso*- $\text{C}_4\text{O}_6\text{H}_6$  at pH 4–5), which are known to be very effective at low concentrations [10, 11].

Sodium chloride ( $\text{NaCl}$ ) is a very important base compound for the chemical industry and therefore it is produced in very large quantities. However, sodium chloride crystals easily cake during storage and transportation [3]. As this makes handling of the material very difficult, caking must be prevented by applying an anticaking agent. For sodium chloride, many anticaking agents are known, including (sodium and potassium) ferrocyanide, nitrilotriacetamide ( $\text{N}(\text{CH}_2\text{CONH}_2)_3$ ), cadmium chloride ( $\text{CdCl}_2$ ) and sodium metaphosphate ( $\text{NaPO}_3$ )<sub>n</sub>,  $n \approx 16$ ). The influence of these anticaking agents on the growth rate, morphology and nucleation rate of sodium chloride crystals was already studied in 1965 [10].

Ferrocyanide is by far the most used anticaking agent for sodium chloride in Europe. It has some drawbacks, however. Most of the sodium chloride produced is used for the production of chlorine

gas by electrolysis. Because of their stability and ionic nature, ferrocyanide ions are difficult to remove prior to electrolysis. During electrolysis, the iron causes the formation of iron hydroxyde ( $\text{Fe}(\text{OH})_3$ ) on the electrodes and at the membranes, raising power consumption. Furthermore, because ferrocyanide contains nitrogen, it is a source of nitrogen trichloride, an explosive gas.

Therefore a new anticaking agent for sodium chloride was introduced: Fe-mTA [11]. This anticaking agent is nearly as effective as ferrocyanide, however, the complex is less stable and therefore the iron can more easily be removed from the brine prior to electrolysis by adding lye. This prevents corrosion of the electrodes and membranes and power consumption is highly reduced. Furthermore, *meso*-tartaric acid does not contain nitrogen and therefore less nitrogen trichloride gas is formed.

Recently, we showed how the anticaking agent ferrocyanide firmly adsorbs on the sodium chloride  $\{100\}$  surface using surface X-ray diffraction [9]. In that study it was concluded that the ferrocyanide ions replace sodium chloride clusters on the surface and block further growth of the NaCl crystal because of the difference in ion charge. In this way, caking is prevented. The required amount of ferrocyanide is  $1.4 \times 10^{-6}$  mol per mol sodium chloride, which corresponds to about  $2 \times 10^{-6}$  mol/m<sup>2</sup>, assuming an average particle size of 200  $\mu\text{m}$ . This amount is almost identical to the maximum coverage of ferrocyanide ions on the (100) surface of sodium chloride [9], which corresponds to  $2.6 \times 10^{-6}$  mol/m<sup>2</sup>. This we define as a coverage fraction  $\theta = 1$ . The required amount for Fe-mTA is in the same range as for ferrocyanide, about  $3 \times 10^{-6}$  mol per mol NaCl. For Fe-mTA the maximum coverage has not been determined, but because the size of the Fe-mTA complex is similar to ferrocyanide, a monolayer will be of the same order of magnitude. Therefore, also for Fe-mTA we define the coverage fraction  $\theta = 1$  as  $2.6 \times 10^{-6}$  mol/m<sup>2</sup>.

A low energy ion spectroscopy (LEIS) study has shown the presence of iron oxochloride and iron oxide layers and a layer of organic material on sodium chloride crystals treated with Fe-mTA [12]. In

that study, performed in vacuum, it was assumed that the iron atoms are transported toward the sodium chloride surface by the Fe-mTA complex, where they form a layer of iron oxochloride and a layer of iron oxide on top. These layers would inhibit the growth of the sodium chloride and thus prevent caking. In this model it was assumed that the only role of the *meso*-tartaric acid molecules is to prevent the formation of iron oxide in solution, by forming an metal-organic complex with the iron.

Here we investigate the growth of sodium chloride crystals by studying step movement on the crystal surface using atomic force microscopy (AFM). Normally, such studies are only possible using a liquid cell [13–17]. However, in 1996 Shindo *et al.* [18, 19] studied the adsorption of water on the sodium chloride {100} surface using AFM. They showed that at relative humidity (RH) of 52% or higher, monatomic steps become mobile. Thereby, they showed that at this humidity, well below the deliquescence point of 75% RH, the adsorbed water layer is thick enough to allow solvation and transport of ions across the surface, even though the water layer is estimated to be only 1 to 4 nm thick [20–22]. Since the water layer is very thin, the AFM-tip is not completely submerged.

In this paper we use this effect to study the growth of sodium chloride crystals and how it is influenced by the two anticaking agents by in situ AFM. Therefore, no liquid cell is needed in these experiments. Step movement occurs by ion transportation through the adsorbed water layer while keeping the RH at 58%. This condition is also close to the industrial usage of anticaking agents.

Apart from the in-situ experiments, we also determined how the anticaking agents change the morphology of the crystal surface at the industrially applied concentration, because in practice it was found that the two anticaking agents change the flow characteristics of sodium chloride powders differently. Flow properties are usually influenced by the surface morphology of a crystalline powder [23]. Even though powders treated with both agents do not cake, a powder treated with ferrocyanide flows freely, while a powder treated with Fe-mTA shows slip-stick behaviour.

## 3.2 Experimental

### 3.2.1 Specimen preparation

Sodium chloride  $\{100\}$  surfaces (approximately  $3 \times 3 \text{ mm}^2$ ) were obtained by cleaving a melt grown sodium chloride crystal, purchased from Ted Pella, Inc. (Redding, California, USA). The cubic  $\{100\}$  faces are the only relevant faces of sodium chloride crystals for anticaking, since the anticaking agents are applied on crystals after their growth. Such crystals have a cubic morphology for sodium chloride.

### 3.2.2 Step flow experiments

A Digital Instruments Nanoscope IIIa MultiMode AFM was operated in contact mode using a J-type piezo scanner. Commercial silicon nitride contact mode cantilevers were used. Both height and deflection signals were recorded. Even though measuring in contact mode, the surface was not altered by the imaging. After measuring, no scan effects were observed, which was checked by making a  $50 \times 50 \text{ }\mu\text{m}^2$  scan around the imaged area. The microscope was placed in a plexi glass box to control the humidity. A dish of a saturated sodium bromide solution in water was placed in the box to keep the RH at  $58 \pm 3\%$ , which was monitored with an EL-USB-2 data logger. The temperature in the box was  $25 \pm 1 \text{ }^\circ\text{C}$ . The variation of the temperature will have little influence on the crystal growth, since the solubility of sodium chloride is nearly independent of the temperature [3].

A large area scan,  $50 \times 50 \text{ }\mu\text{m}^2$ , was performed to select a sloping area containing many monatomic steps. Zooming in on this area,  $4 \times 4 \text{ }\mu\text{m}^2$  images were captured continuously at the same location, creating a film. Each image took 512 seconds to capture (512 lines, 1 Hz) and only images in the same scanning direction were used for the film. Scanning was continued for one to two days, 80 – 160 frames per film. The result is a sped-up film of step flow, at 1024 seconds per frame.

The anticaking agents were applied using small droplets of volatile solvents (ethanol or methanol) in which sodium chloride is poorly soluble, in order to minimise surface roughening by dissolution of the sodium chloride crystal. After evaporation of the solvent, the sample was placed in the humid environment. In order to check solvent influence, films were recorded of moving steps on the surfaces after evaporation of a 2  $\mu$ l droplet of clean ethanol or clean methanol without anticaking agents, applied using a Gilson P20 micropipette. Even though the surfaces treated with methanol showed a little more roughening than those treated with ethanol, no significant difference in step movement rate was observed between these preparations.

Having characterised the properties of the clean system, films of steps and step flow were obtained for several concentrations of applied anticaking agents. For Fe-mTA coverages were used ranging from  $\theta = 0.005$  to 46. Ethanol was used as a solvent for Fe-mTA since the solubility of sodium chloride in ethanol is very low, leading to minimum surface roughening during the evaporation of the solvent droplet. Surface roughening was further limited by using droplets of only 2  $\mu$ l.

For ferrocyanide, the applied coverages ranged from  $\theta = (8 \pm 4) \times 10^{-5}$  to  $\theta = 17$ . The lowest concentrations of ferrocyanide were applied using ethanol as a solvent. Due to the extremely low solubility of potassium ferrocyanide in ethanol, methanol was used as a solvent for the high concentrations of ferrocyanide. This caused a little more surface roughening but did not change the step flow rate. Surface roughening was again limited by applying 2  $\mu$ l droplets.

The industrially applied amounts of anticaking agent on chemical transformation salt correspond to about  $2 \times 10^{-6} \text{ mol/m}^2$  for both ferrocyanide and Fe-mTA, which is approximately one monolayer. The high end of the concentration ranges investigated thus corresponds to very large amounts of the anticaking agent, much more than required in industry for effective anticaking. The lowest

concentrations used were several orders of magnitude lower, chosen such that no difference with clean crystals could be observed anymore.

### 3.2.3 Ex-situ experiments

Cleaved sodium chloride {100} surfaces treated with the anticaking agents were examined in more detail ex-situ, in order to study the surface morphology caused by the anticaking agents. The applied coverages of the anticaking agents were  $\theta = 0.8, 0.4$  and  $0.04$ . The anticaking agents were applied using a  $2\ \mu\text{l}$  droplet of methanol. Methanol was used for both anticaking agents in order to eliminate differences in initial surface roughening by the different solvents.

The methanol was allowed to evaporate and then the crystals were exposed to 58% RH for a few days. After removing the crystals from the plexi glass box, the resulting surface morphology was examined, ex situ, by AFM at a humidity of approximately 40%. Parallel to these experiments, crystals were treated with the same amount of anticaking agents and were examined by AFM immediately after evaporation of the methanol, in order to verify if the morphology change did not result from recrystallisation in the methanol droplet.

These ex-situ observations were performed using a Digital Instruments Dimension 3100 AFM operated in both tapping and contact mode. The resulting surface topography was studied in more detail by acquiring images at various scales, ranging from  $100 \times 100\ \text{nm}^2$  to  $100 \times 100\ \mu\text{m}^2$ .

## 3.3 Results and Discussion

In order to determine whether the anticaking agents are incorporated into the crystal lattice or are desorbed from the surface during growth, NaCl crystals were grown from aqueous solutions in the presence of  $6.1 \times 10^{-5}$  to  $6.1 \times 10^{-2}$  mol/l (1-1000 parts per million) ferrocyanide and Fe-mTA. The resulting crystals were

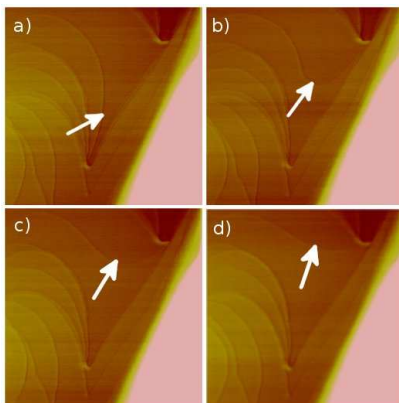


FIGURE 3.1: *Step movement on a clean crystal surface treated with a clean droplet of methanol,  $4 \times 4 \mu\text{m}^2$  AFM height images. a) A step is pinned in lower part of image. b–d) As soon as the pinned point is passed, the highly curved step quickly moves to reduce its negative curvature. Other monatomic steps also move, but at a much lower rate.*

removed from the growth solution, dried and subsequently dissolved in water. The iron content of these solutions was determined using inductively coupled plasma mass spectrometry (ICP–MS), equipped with a collision cell technology (CCT). Only a very small amount of iron could be detected in both cases, corresponding to the iron present in the adhesive water layer. Therefore we conclude that almost no iron is incorporated. The anticaking agents are reversibly adsorbed onto the surface and desorb from the surface when growth continues.

### 3.3.1 Step movement on clean surface

A film was acquired showing the propagation of monatomic steps on a clean sodium chloride crystal surface at  $\text{RH} = 58\%$ . Also when pre-treated with a  $2 \mu\text{l}$  droplet of either ethanol or methanol, monatomic step movement was observed. This result is shown in Figure 3.1 for a surface treated with a droplet of methanol. Several films of step propagation on clean crystal surfaces were recorded, the surfaces having been pre-treated either with methanol or ethanol. Two complete films of step flow on clean crystals are provided as Supporting Information, available online. The measured step height was approximately 0.3 nm, which corresponds to the mon-

atomic step height of  $\frac{1}{2}d_{\langle 100 \rangle} = 0.281$  nm. These observations are in agreement with the results of Shindo *et al.* [19].

In these experiments, we found that the tops of hillocks were dissolving, while the steps near the foot of the same hillock were growing. Therefore, the main driving force for step movement in these experiments is the minimisation of step energy by the elimination of height differences: the surface tends to flatten. This process, surface relaxation [24], has been reported earlier for metal and semiconductor surfaces [25–27], but also for boric acid [28, 29]. It is closely related to Ostwald ripening [30], which is the minimisation of surface energy, or in this case, step energy. We selected locations at the foot of hillocks in order to have the same conditions in all experiments.

If surface relaxation is the main driving force for step movement, the overall supersaturation ( $\Delta\mu$ ) should be close to zero. Therefore, we estimated the overall supersaturation of the solution nanolayer on the clean surface at a humidity of 58%, by measuring the step movement rate and the radius of curvature of freely flowing steps on the clean crystal surface. The step movement rate was found to be independent of the terrace width in all experiments, thus the growth rate is reaction limited. Therefore, according to the Burton Cabrera Frank (BCF) theory of crystal growth [31], the step movement rate and local radius of curvature of a step are related by

$$v_{step}(\vec{r}) = b\Delta\mu_{eff}(\vec{r}) = b\Delta\mu \left( 1 - \frac{\rho_{crit}}{\rho_{curve}(\vec{r})} \right), \quad (3.1)$$

in which  $v_{step}$  is the local step movement rate at location  $\vec{r}$ ,  $b$  a kinetical constant and  $\Delta\mu_{eff}$  the local effective supersaturation, which differs from the overall supersaturation  $\Delta\mu$  due to the local curvature.  $\rho_{curve}$  is the local radius of curvature of the step and  $\rho_{crit}$  the critical radius for two-dimensional nucleation on the surface, given by

$$\rho_{crit} = \frac{\gamma_{step}\Omega}{h_{step}\Delta\mu}, \quad (3.2)$$

in which  $\Omega$  is the volume of a growth unit  $((\frac{1}{2}d_{<100>})^3 = 0.0222 \text{ nm}^3)$ ,  $h_{step}$  is the step height (0.281 nm) and  $\gamma_{step}$  is the step free energy, which is approximately  $1.1 \times 10^{-20} \text{ J/nm}$  for monatomic steps on the  $\{100\}$  face of sodium chloride crystals in contact with an aqueous solution [32].

The propagation rate of the freely moving steps in Figure 3.1, as indicated by the arrows, was determined together with their radius of curvature. In Figure 3.2 the step movement rate of these steps is plotted against the radius of curvature and equations 3.1 and 3.2 are fitted to the data. The best fit gives a supersaturation of  $\Delta\mu = (1.6 \pm 0.6) \times 10^{-24} \text{ J}$ , or  $\frac{\Delta\mu}{kT} = (4 \pm 1) \times 10^{-4}$ , with  $k$  the Boltzmann constant and  $T$  the absolute temperature. This supersaturation is very low, in agreement with the observation that the main driving force for step movement is surface relaxation. The critical radius  $\rho_{crit}$  is  $550 \pm 200 \text{ nm}$ . Because this radius is very large, we can exclude two dimensional nucleation under these conditions, in agreement with our observations. The kinetical constant  $b$  is found to be  $(1.3 \pm 0.6) \times 10^{23} \text{ nm/Js}$ .

The overall supersaturation  $\Delta\mu$  is probably induced by local evaporation of the water layer due to heating caused by the laser light. Another contribution to the supersaturation is the capillary action of the tip. The capillary action increases the local water layer thickness around the tip. When the tip has moved away, the dissolved ions in the attracted water will contribute to the local supersaturation, since the layer thickness will return to its equilibrium value [18].

Even on the clean surface, several steps are pinned by dislocations and other obstacles, because of the extremely large critical radius of curvature of 500 nm [19]. Such steps are shown in the left part of the images in Figure 3.1. We determined the average rate of step propagation and the local radius of curvature of such steps in several films of step propagation on the clean surfaces in order to compare the supersaturation to the value obtained for the freely moving step. Even though the steps are pinned, the step movement is not zero between pinning points (Figure 3.3). Overall, the step rate was  $0.020 \pm 0.005 \text{ nm/s}$ . According to equation

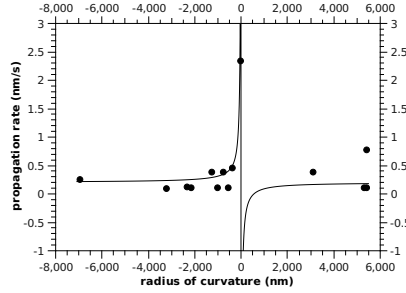


FIGURE 3.2: Propagation rate of the freely moving steps in Figure 3.1 plotted against the local radius of curvature. The continuous line is the best fit of equations 3.1 and 3.2. The data points are single measurements, the error is represented by the dot size.

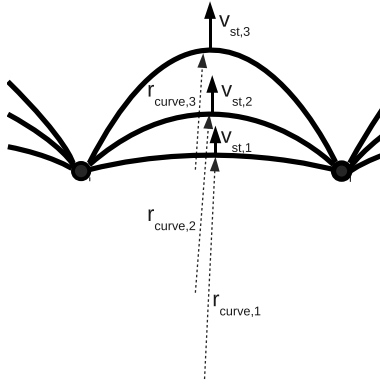


FIGURE 3.3: Step rate and local radius of curvature of a step pinned at two points. Even though the step is pinned, the step movement rate is not zero in between the pinning points.

3.1, this rate corresponds to an averaged radius of curvature of  $550 \pm 200$  nm. This agrees well with the observed radius of curvature of 600-800 nm for these pinned steps. No significant difference was found between ethanol and methanol treated samples.

Many steps emerged from screw dislocations. As their height is  $\frac{1}{2}d_{\langle 100 \rangle}$ , they must have a Burgers vector ( $\vec{b}$ ) component perpendicular to the (100) face of  $\frac{1}{2}[100]$ . This is to be expected because the lowest energy Burgers vector in the sodium chloride F-cell is  $\frac{1}{2}\langle 110 \rangle$ .

### 3.3.2 Growth inhibition by anticaking agents

#### Ferrocyanide

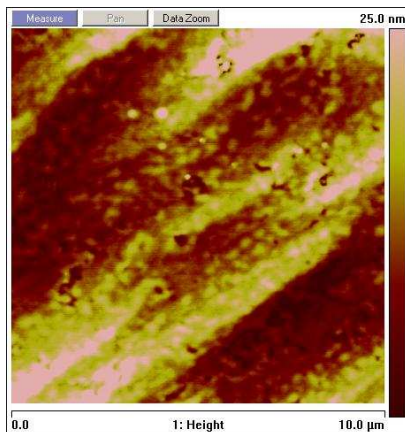


FIGURE 3.4: A sodium chloride surface roughened by the application of a high coverage of Fe-mTA ( $\theta = 47$ ). The surface is very rough and no steps are visible. The surface does not change when exposed to 58% RH. Surfaces roughened by a large amount of ferrocyanide look identical.

Having established the method of observing step movement, we tested how anticaking agents hamper or block step propagation. At high coverages of ferrocyanide, above  $\theta = 3.5$ , the surfaces are found to be very rough and no steps are visible. Figure 3.4 shows a typical surface morphology (obtained using Fe-mTA). A sample treated with ferrocyanide ( $\theta = 0.7$ ), a little less than the industrially applied amount, showed less roughening and some steps that did not move at all at 58% RH.

At a lower coverage of  $\theta = 0.35$ , no roughening was observed. Only monatomic steps were seen on the surface, but they were fully blocked by the ferrocyanide ions. Only at a much lower coverage of  $\theta = 2 \times 10^{-4}$ , step movement was observed, together with their temporary pinning due to the presence of the ferrocyanide ions. This is shown in Figure 3.5; the full film is available online in the Supporting Information.

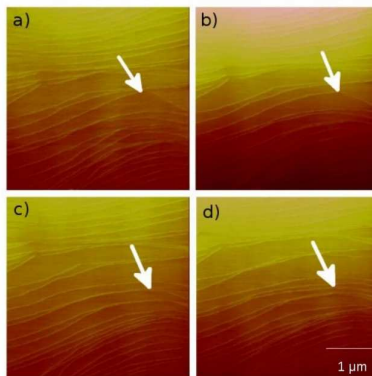


FIGURE 3.5: *Step pinning by ferrocyanide ( $\theta = 2 \times 10^{-4}$ ). Images are  $4 \times 4 \mu\text{m}^2$  AFM height images. In a), the step indicated by the arrow is pinned. In b), the pinning point is passed and the step pins at another point. This sequence repeats in c) and d). Intervals between images are 85 minutes, 50 minutes and 20 minutes respectively.*

The step indicated by the arrows in Figure 3.5 is negatively curved while the step is pinned and its movement is stopped for about one hour. Nevertheless, the net step movement is not retarded at this coverage of ferrocyanide since the highly curved step rapidly catches up with the other steps when the pinning molecule is desorbed. The net propagation rate of this step is approximately 0.02 nm/s. Calculated from the coverage and assuming complete adsorption, only  $5 \times 10^3$  ferrocyanide ions are present on the imaged area, resulting in an average spacing of about 90 nm. Therefore, pinning of steps probably occurs by individual or small clusters of ferrocyanide ions. Extrapolating the observation of step pinning at  $\theta = 2 \times 10^{-4}$  to higher ferrocyanide coverages clearly shows that complete step blocking occurs at such coverages.

When a second step passes the point where a previous step was pinned, it is most often not pinned at the same location; showing that the pinning point is removed. Therefore we conclude that the pinning was caused by molecules that have desorbed and that the pinning of the step was not caused by an edge dislocation.

At an even lower coverage of  $\theta = 8 \times 10^{-5}$ , no significant differences with the clean crystals were detected.

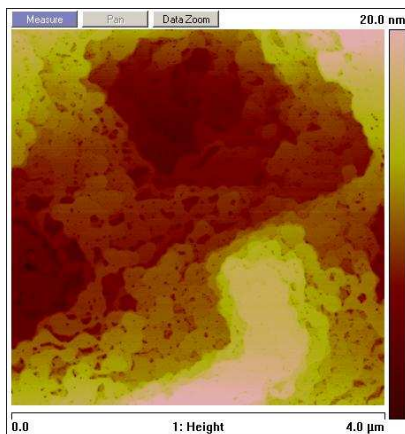


FIGURE 3.6:  $4 \times 4 \mu\text{m}^2$  height image of steps on a sodium chloride crystal treated Fe-mTA,  $\theta = 1$ . Steps are several atomic layers high and are highly curved. They are immobile when exposed to 58% RH air.

### Fe-mTA

A similar series of coverages was used to examine the influence of Fe-mTA on the growth of sodium chloride crystals. At high coverages,  $\theta = 47$  and  $\theta = 5$ , a very thick, rough layer is observed on top of the crystal, as shown in Figure 3.4. No steps are visible at all, nor is there any change in the surface during exposure to humid air (58% RH). At a lower coverage of  $\theta = 1$ , approximately corresponding to the concentration used industrially, steps are visible on the surface. However, they are several atomic layers high and are much less smooth than those observed on clean crystals, see Figure 3.6. Furthermore, they do not move at all upon exposure to humid air (58%RH). The steps are highly curved and are bunched, with small, round holes in the layers. Such a morphology is typical for surfaces blocked by step pinning [14].

At lower coverages, monatomic steps are present, which are mobile. At  $\theta = 0.5$ , movement of these monatomic steps is observed. They are, however, pinned at many locations by the adsorbed Fe-mTA. An example is shown in Figure 3.7, the full film is available

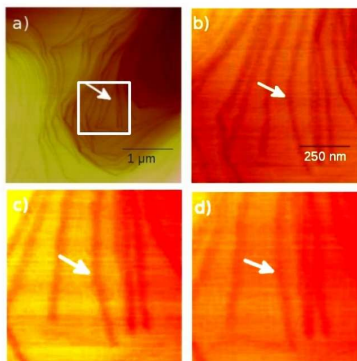


FIGURE 3.7: Step pinning by Fe-mTA: a)  $4 \times 4 \mu\text{m}^2$  height image of a sodium chloride surface treated with Fe-mTA,  $\theta = 0.5$ . Steps are pinned at many locations, most are dislocations. b-d) Zoom in of the indicated  $1 \times 1 \mu\text{m}^2$  area in a: The step indicated by the arrow pinned in b, moving again in c and d. Intervals between images b-d are 34 minutes.

online in the Supporting Information. Even though most pinning points are spiral dislocations, some steps are pinned at sites without a dislocation outcrop. The arrows in Figure 3.7a and b indicate a location where a step is negatively curved, but is temporarily not moving due to pinning. In Figure 3.7c and d the pinning point is removed and the step moves again. Similar to the case of low coverage of ferrocyanide, no net retardation of the step movement is observed. This step moves rapidly after the desorption of the blocking molecules, catching up with the other steps. The net step rate is 0.028 - 0.056 nm/s, which is somewhat higher than expected. This is possibly explained by the relative surface steepness of the location, creating a supersaturation that is locally higher than on flatter areas.

If the coverage of Fe-mTA is lowered further, step pinning is not observed anymore. At coverages of  $\theta = 0.005$  and 0.05, no difference with the clean crystals could be observed.

### 3.3.3 Ex-situ experiments

In order to examine the crystal surfaces after evaporation of the adsorbed water layers, ex-situ AFM was applied. When the

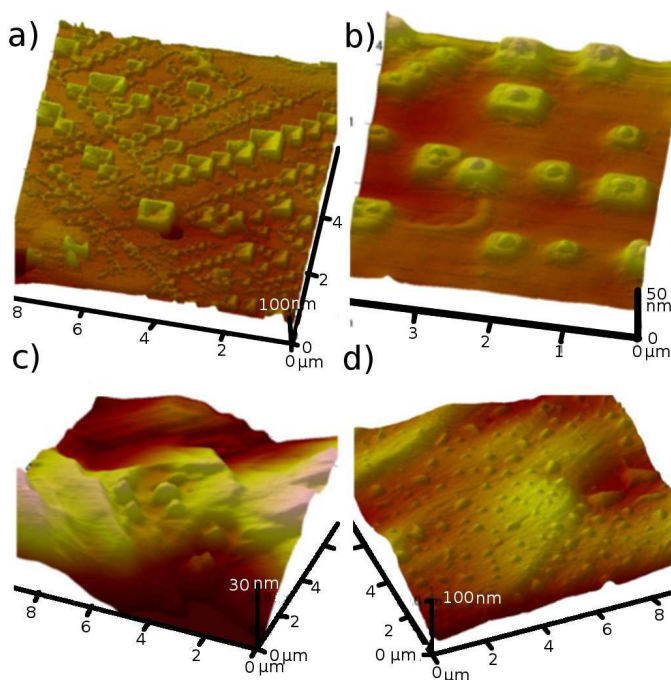


FIGURE 3.8: The surface morphology of sodium chloride crystals treated with anticaking agents and exposed to 58% RH. a) Ferrocyanide,  $\theta = 0.4$ : dendritic growth in the  $\{110\}_c$  directions from one nucleation site. b) Ferrocyanide,  $\theta = 0.04$ : nucleation at multiple sites: inhibition less effective as in (a). c) Fe-mTA,  $\theta = 0.8$ : a rough layer of rounded islands of sodium chloride were formed. d) Fe-mTA,  $\theta = 0.4$ : Many rounded hillocks but less rough than in (c).

crystals were examined directly after application of the anticaking agent, only a little roughening of the surface is detected. After exposure to 58% RH and drying up, the surface morphology is changed dramatically when anticaking agents are present. If no anticaking agent is applied, the surface remains smooth. Applying high amounts of anticaking agents, i.e. coverages of  $\theta = 1$  or higher, results in rough surfaces, like the surface shown in Figure 3.4. The surface morphologies resulting from lower coverages are shown in Figure 3.8. Some more images at different magnifications are given in the Supporting Information, available online.

Figure 3.8a shows the surface morphology induced by ferrocyanide at a coverage  $\theta = 0.4$ . Crystal growth on the surface was

blocked by the ferrocyanide ions adsorbed onto it, therefore dendritic growth of sodium chloride on top of the surface took place, starting from one nucleation site and spreading across the surface in the  $\langle 110 \rangle$  directions. This is comparable to the  $\langle 111 \rangle$  dendritic growth of sodium chloride crystals in presence of ferrocyanide [10]. These dendrites are composed of square, centrally depressed patterns, 20 to 40 nm high and 200 to 900 nm wide.

In Figure 3.8b, the surface is shown as formed after adding ferrocyanide at a coverage  $\theta = 0.04$ . Several isolated hillocks are observed, so probably nucleation at the surface was not inhibited as effectively as in Figure 3.8a. These hillocks are 40 to 80 nm high, which is a little higher than the dendrite patterns of Figure 3.8a. Both the dendrite patterns and the hillocks are nearly square with the edges aligned parallel to the crystal lattice axes.

Crystal surfaces treated with Fe-mTA were influenced very differently. Figure 3.8c shows the surface morphology induced by Fe-mTA,  $\theta = 0.8$ . This surface is very rough, with high steps (up to 30 nm) and hillocks of up to 15 nm high and 500 to 800 nm wide. In contrast to the surfaces treated with ferrocyanide, these features are rounded. At a lower coverage of Fe-mTA,  $\theta = 0.4$ , similar rounded features are observed (Figure 3.8d). However, these hillocks are smaller, 2 to 5 nm high and 200 to 500 nm wide, and are more numerous. This indicates that at a lower concentration, nucleation of sodium chloride was blocked less effectively, resulting in more and smaller surface features.

The observed features were formed during drying after exposure to the humid atmosphere, because these features were not observed when the crystals were studied immediately after application of the anticaking agents. The volume of the observed features is quite high compared to the solubility of sodium chloride and the estimated amount of adsorbed water. However, the thickness of the water layer on sodium chloride crystals at 58% RH is not well known. Estimations range from 3 to 10 water layers [20–22], about 1 to 4 nm thick. Also the solubility of sodium chloride in such a layer can differ from a bulk water solution. So, these features can

indeed be formed during evaporation of the saturated adsorbed water layer.

The surface morphology is very different for surfaces treated with ferrocyanide compared to those treated with Fe-mTA. Surface morphology is very important for powder flow characteristics, therefore this is probably the reason why salt powders treated with ferrocyanide have different flowability properties than powders treated with Fe-mTA.

### 3.3.4 Comparing blocking effects of the anticaking agents

The observed growth inhibition by the anticaking agents ferrocyanide and Fe-mTA is very similar, even though the iron complexes are very different. Both anticaking agents are able to pin monatomic steps on the surface of sodium chloride. At concentrations corresponding to the amounts used industrially for optimal anticaking effectivity, both anticaking agents fully block step movement. These concentrations correspond to a (partial) monolayer of adsorbed iron complexes.

Both anticaking agents can also retard steps. Ferrocyanide ions are able to pin steps at very low coverage ( $\theta = 2 \times 10^{-4}$ ). According to the step pinning model [5], step flow is blocked if the average distance between adsorbed pinning molecules is less than twice the critical radius of curvature. Therefore, the effective concentration of a blocking additive will be highly dependent on the supersaturation.

In industrial applications, a much higher concentration of ferrocyanide is required. This is probably due to the much higher supersaturations reached during storage, because the critical radius decreases with increasing supersaturation (see equation 3.2). Because the critical radius of curvature at high supersaturations is very small for sodium chloride, the distance between adsorbed molecules has to be smaller in order to pin the steps. In the limit in which the critical radius approaches the size of the pinning agent,

the step pinning mechanism is the same as the insulating adsorption layer mechanism. The required concentration is increased because adsorbed impurities can be desorbed from the surface. Even though the original theory on step pinning did not include impurity desorption [5], the theory has been adapted to include this [14, 33].

The higher concentration is also caused by the fact that during storage the overall supersaturation ( $\Delta\mu$ ) is not constant but varies and the time available for caking is longer. The local supersaturation can be even higher near the contact points between adjacent NaCl grains, because of the re-entrant contact angle and the local presence of more water due to the capillary effect. This locally creates an increase of the supersaturation and can lead to solid bridge formation between adjacent particles [34].

For Fe-mTA the concentration needed for the steps to be completely pinned corresponds well with the required amount for effective anticaking. Individual Fe-mTA complexes are not able to pin steps at very low concentrations, in contrast to ferrocyanide ions. At higher coverages ( $\theta = 0.5$ ), step pinning is observed for Fe-mTA. A possible explanation for this difference is that single Fe-mTA complexes are in principle able to pin steps, but most of the Fe-mTA is present as an inactive complex. This inactive part is, for instance, still dissolved in the adsorbed water layer due to a high desorption rate, or immobilised as an inactive iron-mTA complex. It is likely that not all the Fe-mTA is effective since it is light-sensitive. Also, the complexation of Fe-mTA, and therefore its effectivity, depends strongly on the pH and solvent composition. An alternative explanation is that single complexes of Fe-mTA are unable to pin steps, and clusters of Fe-mTA complexes are needed.

Both complexes adsorb onto the  $\{100\}$  surface of sodium chloride. Ferrocyanide ions may be adsorbed stronger, since they are able to pin steps at very low concentrations. The interaction between the Fe-mTA complex and the sodium chloride crystal is probably weaker. For ferrocyanide, we recently determined how this iron complex adsorbs onto this surface using surface X-ray diffraction [9]. However, for the Fe-mTA complex, this is unknown.

Since both complexes pin steps, but finally the steps pass the pinning point unhindered, we conclude that for both anticaking agents the complex is reversibly bound to the surface. When a complex desorbs, the step is of course no longer pinned.

We can also conclude that the earlier proposed growth inhibition mechanism by Fe-mTA [12], i.e. the formation of an iron oxide layer, is unlikely. If such a layer would be formed on the crystal, this would not be a reversible process because of the extremely low solubility of iron oxide. These layers would then need to be incorporated or the crystals would not grow at all. We think that the iron oxide layers are an artefact of the observation technique. Because LEIS is a vacuum technique, it is not possible to study the anticaking agents in contact with the sodium chloride crystal in situ, and the layers were likely formed when the adsorbed water layer was evaporated, depositing the dissolved anticaking agent on the surface followed by oxidation.

### 3.4 Conclusions

We were able to observe monatomic step movement on the  $\{100\}$  faces of sodium chloride crystals in contact with a humid atmosphere at 58% RH using AFM. In this way, we were able to determine step movement rates, the supersaturation and the driving force. Also, we were able to examine how the anticaking agents ferrocyanide and Fe-mTA inhibit the growth of sodium chloride crystals by observing step pinning in situ. Ferrocyanide does this already at a concentration of  $\theta = 2 \times 10^{-4}$ , for Fe-mTA a coverage of  $\theta = 1$  is required.

Furthermore, we have shown that an earlier proposed mechanism for the anticaking effectivity for Fe-mTA [12] is probably incorrect. A surface X-ray diffraction experiment is needed to determine how this iron complex adsorbs exactly on the  $\{100\}$  surface of sodium chloride crystals.

Both anticaking agents influence the surface morphology of the sodium chloride crystals after separation of the crystals from the humid environment and subsequent drying. Ferrocyanide causes the formation of dendrites and cornered, square hillocks on the surface, while Fe-mTA causes the formation of almost hemispherical hillocks. This difference may explain the difference in flowability between ferrocyanide treated or Fe-mTA treated sodium chloride powders.

### Acknowledgement

We would like to acknowledge Akzo Nobel Industrial Chemicals and the Dutch Ministry of Economic Affairs for funding (EOS-KTO program, AgentschapNL). Furthermore, we thank Jelle Eygensteijn for the ICP-MS measurements.

### Supporting Information

Several film files: two films of step propagation on clean sodium chloride crystal surfaces, one pre-treated with ethanol and one with methanol; one film of step pinning by ferrocyanide at a coverage  $\theta = 0.0002$  and one film of step pinning by Fe-mTA at a coverage  $\theta = 0.5$ . Furthermore some image files of surface morphologies, like those in Figure 3.8, at different magnification and a text file explaining the choice of the experimental conditions. This information is available free of charge via the Internet at <http://pubs.acs.org>.

### References

- [1] J. Nývlt and J. Ulrich. *Admixtures in Crystallization*. VCH, (1995).
- [2] K. Sangwal. *Additives and Crystallization Processes*. Wiley, (2007).
- [3] D.W. Kaufmann. *Sodium Chloride: the production and properties of salt and brine*. Reinhold, (1960).
- [4] Y.L. Chen and J.Y. Chou. *Powder Technol.*, (1993), **77**, 1–6.

- [5] N. Cabrera and D.A. Vermilyea. The growth of crystals from solution. In R.H. Doremus, B.W. Roberts, and D. Turnbull, editors, *Growth and Perfection of Crystals*, pages 393–410. Wiley, (1958).
- [6] R. Lacmann and I.N. Stranski. The effect of adsorption of impurities on the equilibrium and growth forms of crystals. In R.H. Doremus, B.W. Roberts, and D. Turnbull, editors, *Growth and Perfection of Crystals*, pages 427–440. Wiley, (1958).
- [7] I. Weissbuch, L. Addadi, M. Lahav, and L. Leiserowitz. *Science*, (1991), **253**, 637–645.
- [8] N. Radenovic, W.J.P. van Enkevort, D.M. Kaminski, M.C.R. Heijna, and E. Vlieg. *Surf. Sci.*, (2005), **599**, 196–206.
- [9] A.A.C. Bode, V. Vonk, D.J. Kok, F.J. van den Bruele, A. Kerkenaar, M. Mantilla, S. Jiang, J.A.M. Meijer, W.J.P. van Enkevort, and E. Vlieg. *Cryst. Growth Des.*, (2012), **12**, 1919–1924.
- [10] M.A. van Damme-van Weele. *Influence of additives on the growth and dissolution of sodium chloride crystals*. PhD thesis, Technische Hogeschool Twente, Enschede, (1965).
- [11] R.M. Geertman. Use of carbohydrate-based metal complexes in non-caking salt compositions. US patent WO 00/59828, (2006).
- [12] R.M. Geertman. *VDI-Berichte*, (2005), **1901**, 557–562.
- [13] H.H. Teng, P.M. Dove, C.A. Orme, and J.J. De Yoreo. *Science*, (1998), **282**, 724–727.
- [14] T.A. Land, T.L. Martin, S. Potapenko, G. T. Palmore, and J.J. DeYoreo. *Nature*, (1999), **399**, 442–445.
- [15] A. Mauri and M. Moret. *J. Cryst. Growth*, (2000), **208**, 599–614.
- [16] C.A. Orme, A. Noy, A. Wierzbicki, M.T. McBride, M. Grantham, H.H. Teng, P.M. Dove, and J.J. DeYoreo. *Nature*, (2001), **411**, 775–779.

- [17] S.J. Wilkins, B.A. Coles, and R.G. Compton. *J. Phys. Chem. B*, (2002), **106**, 4763–4774.
- [18] H. Shindo, M. Ohashi, K. Baba, and A. Seo. *Surf. Sci.*, (1996), **357-358**, 111–114.
- [19] H. Shindo, M. Ohashi, O. Tateishi, and A. Seo. *J. Chem. Soc., Faraday Trans.*, (1997), **93**, 1169–1174.
- [20] S.J. Peters and G.E. Ewing. *J. Phys. Chem. B*, (1997), **101**, 10880–10886.
- [21] M. Foster and G.E. Ewing. *Surf. Sci.*, (1999), **427-428**, 102–106.
- [22] M. Hallquist, N.B. Petrucci, C. Kreuzer, V.P. Ostanin, and R.A. Cox. *Phys. Chem. Chem. Phys.*, (2000), **2**, 4373–4378.
- [23] T. Oshima, Y.L. Zhang, M. Hirota, M. Suzuki, and T. Nakagawa. *Adv. Powder Technol.*, (1995), **6**, 35–45.
- [24] H.C. Jeong and E.D. Williams. *Surf. Sci. Rep.*, (1999), **34**, 171–294.
- [25] N.C. Bartelt, R.M. Tromp, and E.D. Williams. *Phys. Rev. Lett.*, (1994), **73**, 1656–1659.
- [26] N.C. Bartelt, W. Theis, and R.M. Tromp. *Phys. Rev. B*, (1996), **54**, 11741–11751.
- [27] G.L. Kellogg and N.C. Bartelt. *Surf. Sci.*, (2005), **577**, 151–157.
- [28] J.A.S. Cleaver and P. Wong. *Surf. and Interface Anal.*, (2004), **36**, 1592–1599.
- [29] J.A.S. Cleaver, G. Karatzas, S. Louis, and I. Hayati. *Powder Technol.*, (2004), **146**, 93–101.
- [30] W. Ostwald. *Lehrbuch der Allgemeinen Chemie*, volume 2. Engleemann, Leipzig, Germany, (1896).
- [31] W.K. Burton, N. Cabrera, and F.C. Frank. *Proc. Roy. Soc. A*, (1950), **243**, 299–358.

- [32] J. Christoffersen, E. Rostrup, and M.R. Christoffersen. *J. Cryst. Growth*, (1991), **113**, 599–605.
- [33] W.J.P. van Enkevort and J.H. Los. *J. Phys. Chem. C*, (2008), **112**, 6380–6389.
- [34] M. Wahl, R. Kirsch, S. Trapp, and M. Bottlinger. *Chem. Eng. Technol.*, (2006), **29**, 674–678.

## Chapter 4

# Structure and activity of the anticaking agent iron(III) *meso*-tartrate

*Arno A.C. Bode, Sanne J.C. Granneman, Martin C. Feiters,  
Paul Verwer, Shanfeng Jiang, Jan A.M. Meijer, Willem J.P. van  
Enckevort and Elias Vlieg*

### Abstract

Iron(III) *meso*-tartrate, a metal-organic complex, is a new anticaking agent for sodium chloride. A molecular structure in solution is proposed, based on a combination of experimental and molecular modelling results. We show that the active complex is a binuclear iron(III) complex with two bridging *meso*-tartrate ligands. The iron atoms are antiferromagnetically coupled, resulting in a reduced paramagnetic nature of the solution. In solution, a water molecule coordinates to each iron atom as a sixth ligand, resulting in an octahedral symmetry around each iron atom. When the water molecule is removed, a flat and charged site is exposed, matching the charge distribution of the sodium chloride crystal surface. This charge distribution is also found in the iron(III) citrate complex, another anticaking agent. This is the likely adsorption geometry on the crystal surface. This adsorption results in step pinning, which in turn explains the anticaking activity of the iron(III) *meso*-tartrate complex.

## 4.1 Introduction

Sodium chloride (NaCl, rock salt) is a very important base compound for the chemical industry, which is mainly used for the production of chlorine by electrolysis. Therefore, it is produced and transported in vast quantities. Because it is highly hygroscopic, NaCl is prone to caking, which is prevented using anticaking agents [1].

The most commonly used anticaking agents for NaCl are sodium or potassium ferrocyanide ( $[\text{Fe}(\text{CN})_6^{4-}]$ ) salts. These are very effective in preventing caking, requiring only extremely low concentrations of typically a few parts per million [2]. However, ferrocyanide causes problems during electrolysis and it is difficult to remove in advance. Since ferrocyanide contains nitrogen atoms, it causes the formation of nitrogen trichloride ( $\text{NCl}_3$ , an explosive gas) and the iron atoms are deposited in the form of iron hydroxide on the membranes and electrodes, increasing power consumption. Therefore, a new anticaking agent was required.

Iron(III) *meso*-tartrate (Fe-mTA) was introduced as an alternative anticaking agent for NaCl. It is effective at the same concentrations as ferrocyanide, namely a few parts per million [3]. Since Fe-mTA does not contain nitrogen, no nitrogen trichloride is formed from it during electrolysis. Also, the iron can easily be removed prior to electrolysis, by adding lye. Fe-mTA is only effective as an anticaking agent around pH 4 – 5.

Recently, we showed how both ferrocyanide and Fe-mTA prevent caking. Both agents are able to inhibit crystal growth of sodium chloride by step pinning [4]. Inhibiting crystal growth prevents caking, because the agglomeration of particles is caused by the slight dissolution and consecutive recrystallisation of the material during humidity cycling of the environment. Furthermore, we showed how the ferrocyanide ion is adsorbed onto the sodium chloride crystal surface [5], thereby explaining how the ferrocyanide ion pins steps.

For Fe-mTA the mechanism for molecular adsorption on the sodium chloride crystal surface is unknown. Not even the molecular structure of the metal-organic complex is known, though a structure has been proposed without any experimental evidence [6]. However, knowledge of the molecular structure is required to understand the molecular adsorption geometry of Fe-mTA on sodium chloride.

Our goal is to solve the molecular structure of the anticaking agent Fe-mTA and understand its interaction with the sodium chloride crystal. Moreover, we want to understand why the related compounds iron(III) *L*-tartrate (Fe-LTA) and iron(III) *LD*-tartrate (Fe-LDTA) are not effective anticaking agents. From the literature it is known that trivalent metal-tartrate complexes are mostly binuclear complexes and that the carbonyl and hydroxy groups of the tartrate ligands are completely deprotonated [7–11], in contrast to divalent metal-tartrate complexes [12, 13]. A binuclear tartrate complex was suggested for iron(III) *D*-tartrate [14]. The structure of a binuclear metal *meso*-tartrate was determined for chromium(III) [15], showing that the formation of binuclear complexes is in principle also possible with *meso*-tartrate ligands, as was shown earlier for *LD* and *L* complexes.

Iron(III)-tartrates are notoriously difficult to crystallise [16], only one crystal structure of an iron(III) tartrate is known [17] with racemic (*LD*) tartrate ions but this structure is not relevant for the molecular structure in solution and it is not included in the Cambridge Structural Database (CSD). The crystallisation experiments performed in our lab did not produce any single crystals or crystalline powders either, only amorphous powders or gels. Therefore, we studied Fe-mTA in solution combining electron paramagnetic resonance (EPR, also known as electron spin resonance, ESR), UV-VIS spectroscopy, magnetic susceptibility data and molecular modelling techniques. Nuclear Magnetic Resonance (NMR) spectroscopy was not applied, since unpaired electrons broaden NMR signals, usually making NMR unsuitable in paramagnetic systems [18]. We compare our data on Fe-mTA to the iron(III) citrate complex (Fe-citrate), which is also an anticaking agent for sodium

chloride, of which the molecular structure and magnetic properties are known [19, 20]. Based on all this information, a complex structure is proposed together with a possible adsorption geometry of this complex on the sodium chloride crystal surface.

Furthermore, we show that Fe-mTA is a binuclear complex at the pH-range of 4–7, i.e. the range at which it is an effective anti-caking agent. At a lower pH, a mononuclear complex is formed, while at a higher pH iron hydroxide is formed.

## 4.2 Experimental

The magnetic properties of the various complexes in solution were studied by measuring the magnetic susceptibility to determine whether the complex is mononuclear or binuclear. In order to get more information on the complexation, the solutions were also studied using UV-VIS spectroscopy and molecular information about the complexes was obtained using EPR. In addition, a single crystal of Fe-citrate was grown with pyridine as counter ion, in order to check the structure obtained by Shweky *et al.* [19]. A single crystal was mounted in air on a glass fibre. Intensity data were collected at -65 °C. A Nonius KappaCCD single-crystal diffractometer was used (phi and omega scan mode) using graphite monochromated Mo-K $\alpha$  radiation. Intensity data were corrected for Lorentz and polarisation effects. SADABS multiscan correction was applied [21]. The structure was refined with standard methods using SHELXL97 [22].

Aqueous solutions of Fe-mTA, Fe-LTA, Fe-LDTA and Fe-citrate were prepared at various pH-values, by dissolving equimolar amounts of iron(III) chloride (FeCl<sub>3</sub>) and *meso*-, *L*- or *LD*- tartaric acid (C<sub>4</sub>O<sub>6</sub>H<sub>6</sub>) or trisodium citrate (Na<sub>3</sub>C<sub>5</sub>O<sub>7</sub>H<sub>5</sub>) in MilliQ-grade water. As a reference, aqueous iron(III) chloride solutions without ligands were prepared at various pH-values. The pH was set by adding hydrochloric acid or sodium hydroxide.

For the magnetic susceptibility measurements, the concentration used was approximately 0.2 mol/l. The magnetic susceptibility measurements were performed using a Sherwood Scientific Magnetic Susceptibility Balance. UV-VIS spectra were obtained using a PerkinElmer Lambda 35 UV/VIS spectrometer. The concentration used was approximately  $1 \times 10^{-3}$  mol/l. The EPR-spectra were recorded using a Bruker ER220 X-band spectrometer at 4.2 K. For the EPR measurements 0.01 mol/l solutions were prepared. Both the UV-VIS and magnetic susceptibility measurements were corrected for solvent influence by subtracting a clean signal. Diamagnetic corrections were performed for the magnetic susceptibility measurements. The magnetic susceptibility was also measured in saturated sodium chloride solutions. The exact concentrations, after pH calibration, were determined using inductively coupled plasma mass spectroscopy (ICP-MS).

EPR data were recorded for Fe-mTA, Fe-LTA, Fe-LDTA around pH 4.5, and for Fe-mTA and Fe-citrate around pH 2, 4 and 6. The UV-VIS spectra and the magnetic susceptibility were obtained for Fe-mTA and Fe-citrate from pH -1 to 8, for FeCl<sub>3</sub> from pH -1 to 7 and for Fe-LTA and Fe-LDTA at pH 0 and pH 4.5.

Molecular modelling used the structure proposed for Fe-mTA [6] as a starting point, since this binuclear structure is a possible fit to our experimental results. The structure was first minimised in a box of water molecules using Molecular Mechanics. A 5000 ps simulation was performed at 373 K using the programme Materials Studio 4.3 with the Discover Module and the Compass force field. The number of particles, the volume and the temperature were kept constant. The resulting structure was refined using Molecular Dynamics, which includes quantum mechanical effects.

### 4.3 Results and Discussion

Since the Fe-mTA complex will not crystallise, various techniques are used to obtain information about the complex structure. Fe-mTA is compared to Fe-citrate, which is also an effective anti-

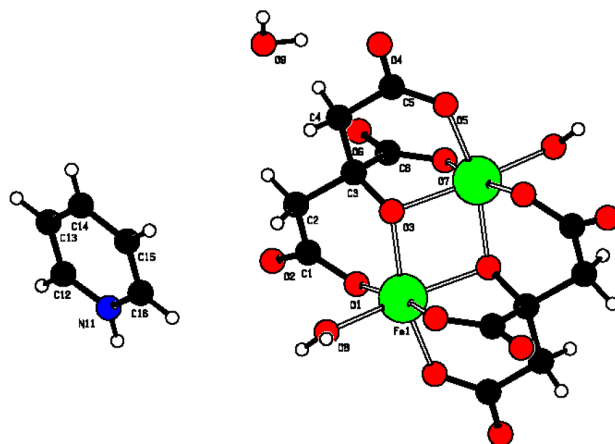


FIGURE 4.1: The crystal structure of Fe-citrate with pyridine as a counter ion. The structure is identical to the one obtained by Shweky *et al.* [19]. The 2:2 binuclear complex is clearly visible. The citrate ligand is completely deprotonated, including the hydroxy-group, which coordinates to both iron ions, forming a bridge. This bridging explains the antiferromagnetic coupling.

caking agent for sodium chloride [3] and citrate is a comparable ligand in the sense that it has four deprotonatable  $\text{-OH}$  groups. The structure and magnetic properties of the Fe-citrate complex are known [19, 20]. The experimental data are used to test a proposed structure for Fe-mTA [6], which is similar in structure to Fe-citrate. In addition, we compare our data on Fe-mTA and Fe-citrate to the enantiopure Fe-LTA and the racemic Fe-LDTA, which do not have anticaking effects.

### 4.3.1 Single crystal X-ray diffraction

The structure found by Shweky *et al.* [19] was tested using single crystal X-ray diffraction. Figure 4.1 shows the obtained crystal structure of Fe-citrate with pyridine as a counter ion, which is identical to the structure found in the literature. The Fe-citrate structure clearly shows a 2:2 binuclear complex, with two iron(III) ions and two bridging, completely deprotonated citrate ligands. Each carboxylate group is coordinated to an iron ion, while the deprotonated hydroxyl group coordinates to both iron ions, forming a bridge. Each iron ion therefore has three coordinating car-

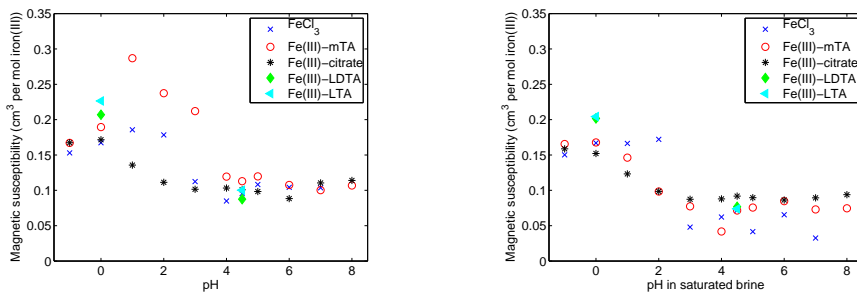


FIGURE 4.2: The molar magnetic susceptibility ( $\chi_m$ ) of Fe-mTA, Fe-citrate and  $\text{FeCl}_3$  at pH -1 – 7 or 8, and Fe-LTA and Fe-LDTA at pH 0 and 4.5. Left: in water. Right: in saturated brine.

boxylate groups and two deprotonated hydroxyl groups. A water molecule coordinates to each iron ion as a sixth ligand, resulting in a favourable octahedral environment of the iron ion. The two octahedrons are edge-shared, explaining the antiferromagnetic coupling of the iron ions [20, 23]. Antiferromagnetic coupling is very common in bridged, binuclear metal complexes, while ferromagnetic coupling is rare and requires precise ligand design [24, 25].

### 4.3.2 Magnetic susceptibility

The magnetic susceptibility was measured for the iron tartrates and iron citrate to test whether the iron tartrate complexes also show antiferromagnetic coupling. Figure 4.2 shows the molar magnetic susceptibility ( $\chi_m$  in SI units,  $\text{cm}^3 \text{mol}^{-1}$ ) as a function of pH for all iron tartrates and iron citrate solutions, both in brine and in water. There is a clear transition between low and higher pH for Fe-mTA: at low pH the magnetic susceptibility of Fe-mTA is quite high, indicating that the iron ions are not antiferromagnetically coupled. At higher pH, the magnetic susceptibility drops, even though the solutions remain clear: no iron hydroxide is formed. This indicates the formation of an antiferromagnetically coupled binuclear complex. Thus there is a change in structure around pH 4. This corresponds well to the fact that Fe-mTA is a good anticaking agent at pH 4–5, while it is inactive at low pH. At pH 0 and -1, the magnetic susceptibility also decreases, especially in water, an observation that we cannot easily explain. The same

trend is observed both in brine and in water, indicating that sodium chloride does not influence the complexation.

The influence of the pH is not as strong for Fe–citrate as for Fe–mTA, so this complex is probably more stable at very low pH. The magnetic susceptibility is relatively low, so probably the iron ions in this complex are also antiferromagnetically coupled. Iron chloride has a high  $\chi_m$  at pH 2 and lower. At pH 3 and higher,  $\chi_m$  drops, which is readily explained by the formation of iron hydroxide, as confirmed by the fact that the solution becomes turbid.

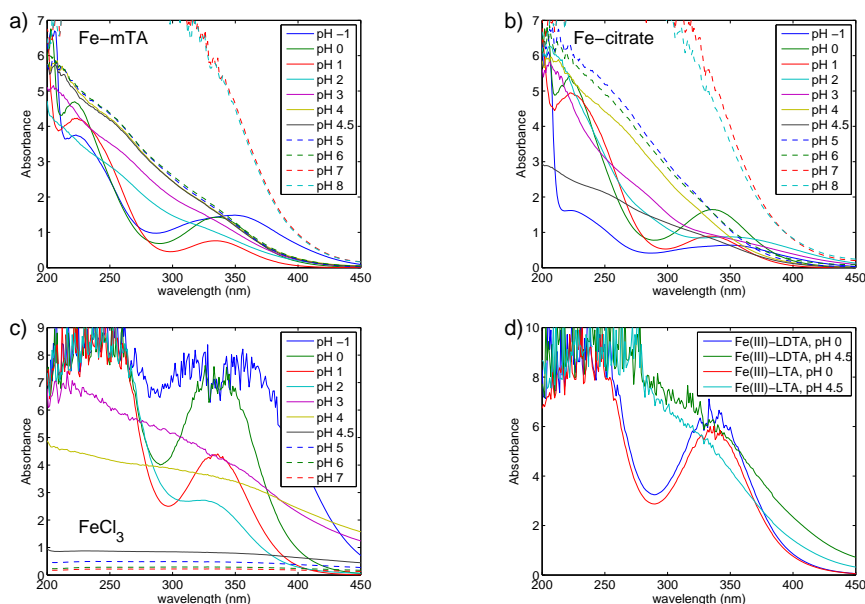


FIGURE 4.3: UV-VIS spectra of the iron(III) tartrates, iron(III) citrates and iron(III) chloride at pH -1 to 7 or 8. a) Fe–mTA, b) Fe–citrate, c) FeCl<sub>3</sub> and d) Fe–LTA and Fe–LDTA, at pH 0 and 4.5.

Interestingly, Fe–LTA and Fe–LDTA show the same magnetic behaviour as Fe–mTA: at low pH the magnetic susceptibility is high, indicating no antiferromagnetic coupling, while at pH 4.5, the magnetic susceptibility is lower even though there is no iron hydroxide formation. Therefore we assume that also *L*– and *LD*–tartrate iron(III) complexes are binuclear and antiferromagneti-

cally coupled at pH 4.5, which is in agreement with results obtained by Timberlake [14]. Even though these complexes are also binuclear, they are not active anticaking agents. An explanation for this is given in section 4.3.5.

The spin state of the iron atoms was calculated to test whether the transition at pH 4 can be contributed to the formation of binuclear complexes at pH above 4. The spin state of mononuclear complexes should be similar to that of free iron(III) ions, since antiferromagnetic coupling is not possible. The spin state can be calculated from the molar magnetic susceptibility ( $\chi_m$ ) of the solutions, applying diamagnetic corrections for the ions present [26]. The effective magnetic moment,  $\mu_{eff}$  expressed in Bohr magnetons ( $\mu_B$ ), depends on  $\chi_m$  as follows:

$$\mu_{eff} = \sqrt{\frac{3k_b T \chi_m}{N_A \mu_0 \mu_B^2}}, \quad (4.1)$$

in which  $k_b$  is the Boltzmann constant,  $T$  the temperature in Kelvin,  $N_A$  the Avogadro constant and  $\mu_B$  the Bohr magneton. The magnetic moment of the iron atoms,  $\mu_{spin\ only}$ , is usually the main contribution to the effective magnetic moment of the entire molecule, so

$$\mu_{eff} \cong \mu_{spin\ only}. \quad (4.2)$$

Subsequently,  $\mu_{spin\ only}$  depends on the spin state  $S$  of the iron atoms as:

$$\mu_{spin\ only} = g_e \sqrt{S(S+1)}, \quad (4.3)$$

in which  $g_e$  is the electron g-factor. The high values for  $\chi_m$  around pH -1 – 3 are approximately  $0.17\text{ cm}^3\text{mol}^{-1}$ , corresponding to an effective magnetic moment of  $5.7\ \mu_B$  and a spin state  $S$  of 2.4. This value is in good agreement with the spin state for free iron(III) atoms,  $S = 5/2$ , indicating that at this pH range the complexes are mononuclear, in contrast to the high pH range. The highest values for  $\chi_m$ , around  $0.28\text{ cm}^3\text{mol}^{-1}$ , are probably due to other contributions to the magnetic moment next to the spin, like orbital contributions, making the assumption in equation 4.2 invalid.

### 4.3.3 Optical observations and UV–VIS spectroscopy

Colour transitions in metal–organic solutions indicate changes in the complex structure and therefore they should correspond to the transitions detected using the magnetic susceptibility. The colours of the iron tartrate and iron citrate solutions vary strongly with the pH. However, the colour of the solutions did not depend on the concentration, therefore the complexation does not depend strongly on the concentration. The solutions of all complexes are orange at pH -1 and are yellow at pH 0 and 1. In pH-regime from 3 to 5, Fe–mTA solutions turn green. This interval corresponds to the regime in which it is an active anticaking agent. At higher pH, from 6 to 8, the Fe–mTA solutions turn brownish to red though they remain clear, probably due to the formation of iron hydroxide clusters.

A similar trend is observed for Fe–citrate: from pH 2 to 4, the solution turns from red to greenish, and at higher pH values, the solutions turn red. Fe–LTA and Fe–LDTA are not green around pH 4.5, but red. The green colour is probably typical for iron(III) complexes which have the right iron environment for anticaking activity, since the green colour is observed for both Fe–mTA and Fe–citrate in the pH range at which they are active anticaking agents. Photographs of the solutions are given in the appendix.

The complexation of the iron tartrates and citrate was also studied using UV–VIS, to show that the mononuclear complexes disappear at a pH above 3. Mononuclear complexes of these compounds have a characteristic absorption at 300 – 400 nm [14]. In Figure 4.3 the UV-VIS absorbance spectra of all solutions at low concentrations are shown. The absorbance at wavelength  $\lambda$ ,  $A_\lambda$ , is plotted against this wavelength.  $A_\lambda$  is defined as

$$A_\lambda = {}^{10}\log \left( \frac{I}{I_0} \right), \quad (4.4)$$

in which  $I$  is the transmitted intensity and  $I_0$  is the incident intensity at wavelength  $\lambda$ . At 225 – 250 and 300 – 400 nm a broad peak is observed for both Fe–citrate and Fe–mTA at pH -1 to 1 (Figures 4.3 a and b). At pH 2 and 3, weak traces of these peaks can be

STRUCTURE AND ACTIVITY OF THE ANTICAKING AGENT IRON(III)  
MESO-TARTRATE

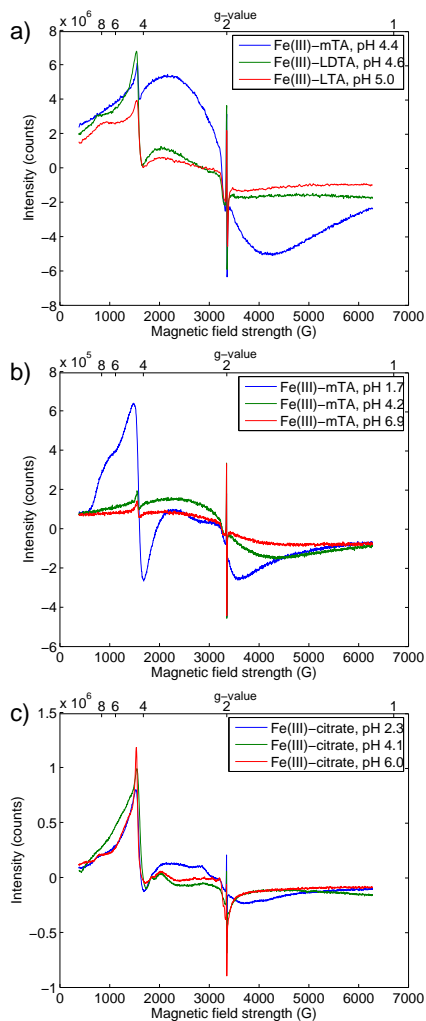


FIGURE 4.4: EPR spectra of aqueous solutions of iron(III)-tartrates and iron(III)-citrates. a) Fe-mTA, Fe-LTA and Fe-LDTA at pH 4. b) Fe-mTA at pH 1, 4 and 6. c) Fe-citrate at pH 1, 4 and 6.

seen for Fe-mTA though not for Fe-citrate, and the peaks are not present at higher pH values. Iron(III) chloride also shows a peak in absorbance in the 300 to 400 nm regime at pH -1 to 2 (Figure 4.3c). At higher pH values, the total absorbance decreases due to precipitation of iron hydroxide. Also for Fe-LTA and Fe-LDTA (Figure 4.3d), a clear peak at 300 – 400 nm is observed at pH 0. The peak at 300 – 400 nm indicates a mononuclear complex [14], having no antiferromagnetic coupling. This peak disappears at the high pH-ranges at which the complexes show a lowered magnetic susceptibility, further proof of a complex structure transition.

#### 4.3.4 EPR

In Figure 4.4 the EPR spectra are shown. All spectra have as the most important feature a signal around 1600 Gauss ( $g = 4.3$ ), which indicates the presence of high-spin Fe(III) ( $S = 5/2$ ) with a high rhombicity. The signals in the region around 3000 Gauss, i.e. the sharp radical-like signal at 3200 Gauss ( $g = 2$ ) and the copper-(II) impurity signal in Figure 4.4c at 3000 Gauss, are background signals which can be ignored for the discussion.

It is difficult to compare the intensity of the EPR signals, as estimated from the amplitude at  $g = 4.3$ , of the three data sets (in Figures 4.4a, b and c). This can be seen from the different intensities though identical shapes of the signals of Fe-mTA at pH 4.4 and 4.2 in Figures 4.4a and b respectively. Probably this is due to different sample alignment or preparation: all signals in Figure 4.4b are relatively weak. However, within each data set comparisons can be made. In Figure 4.4b, the signal from Fe-mTA at pH 1.7 is relatively strong, compared to Fe-mTA at pH 4.2 and 6.9. These weaker signals at pH 4.2 and 6.9 probably originate from antiferromagnetically coupled complexes, which therefore are almost EPR silent. In contrast, the relatively strong signal from Fe(III)-mTA at pH 1.7 originates from mononuclear complexes, which do not show antiferromagnetic coupling. Therefore, this signal is more intense. The intensity of the iron citrate samples is independent of the pH between pH 2.3 and 6.0 (see Figure 4.4c).

These results are consistent with the measurements of the magnetic susceptibility (Figure 4.2), from which it was concluded that the antiferromagnetic coupling of the Fe-mTA was broken at pH 3 and below, whereas that of the Fe-citrate was still stable at pH 2. This can be explained by the  $pK_a$  values of the ligands, since protonation of a ligand will destabilise the binuclear complexes. It can be expected that at low pH a tartrate ligand is more easily protonated than a citrate ligand: a tartrate ligand has two deprotonated hydroxy groups and two carboxyl groups, where a citrate ligand has three carboxyl groups and only one deprotonated hydroxy group. So both the iron tartrate and the iron citrate complexes show antiferromagnetic coupling, however at a slightly different pH range.

The spectra of Fe-mTA at pH 4.4 and 4.2, in Figures 4.4a and b respectively, appear to contain an additional very broad signal that is approximately centred around  $g = 2$  and of which the origin is unknown.

Figure 4.4a shows the spectra of Fe-mTA, Fe-LTA and Fe-LDTA at pH values in the range 4.5 – 5. It can be seen that the environment of the iron in the Fe-LTA and Fe-LDTA complexes is different from that in the Fe-mTA complex, since there is a shoulder at  $g = 8 - 10$ , which is not present in the Fe-mTA spectrum. In Figure 4.4b, the spectrum of Fe-mTA at pH 1.7 has a similar shoulder at  $g = 8 - 10$ , indicating that the iron environment is different from that at pH 4.2 and 6.9, and is probably similar to the iron environments in the Fe-LTA and Fe-LDTA complexes at pH 4.5 – 5 (Figure 4.4a). These shoulders indicate a somewhat lower rhombicity of the iron environment compared to the Fe-mTA complex at pH 4.2 – 6.9 [27]. So, the lower rhombicity in the iron tartrate complexes correlates with inactivity as an anticaking agent (Fe-LTA and Fe-LDTA at pH 4.5 – 5 and Fe-mTA at pH 1.7).

For the Fe-citrate spectra in Figure 4.4c, the signal does not change drastically between pH 2.3 and 6, except for the higher intensity at  $g = 4.3 - 10$  at pH 4.1, so the environment of the iron ion has a little lower rhombicity at this pH [27]. All magnetic fields and corresponding  $g$  values for the signals observed on the

low-field side of the  $g=4.3$  signal fall within the range observed for a rhombogram calculated for  $S=5/2$  systems [27], so all signals can be explained as due to high-spin iron(III) with subtly different environments and the oxidation state of the iron atoms is not changed.

#### 4.3.5 Molecular Modelling of the Fe–mTA complex

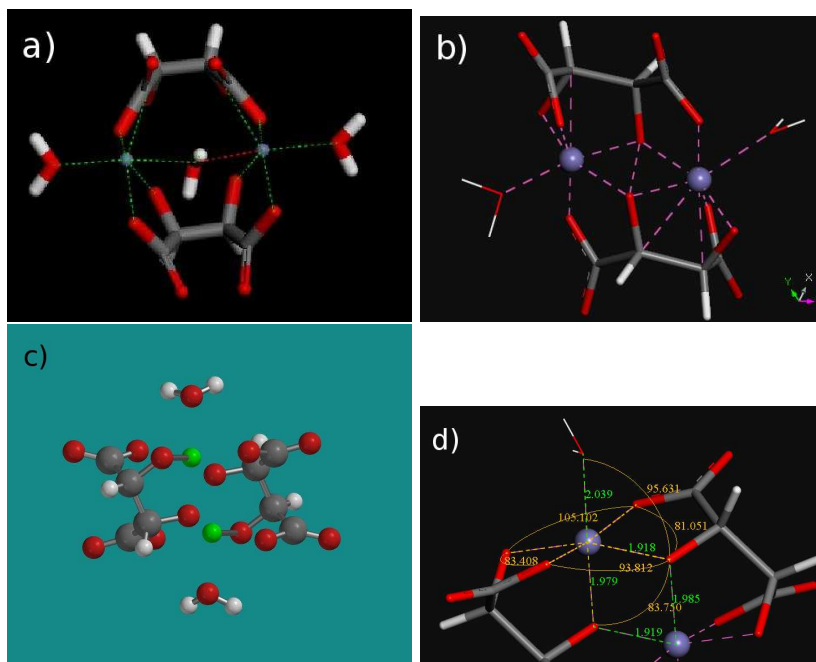


FIGURE 4.5: Subsequent steps in the molecular modelling of the Fe-mTA complex. a) the initial structure as proposed by Geertman [6]. b) The structure after a molecular mechanics simulation of 5000 ps. c) The structure after minimisation using molecular dynamics. d) Same structure zoomed in on the iron environment. Colour codes in the graphs: grey: carbon, red: oxygen, white: hydrogen, iron: green or blue.

Molecular modelling was performed for the Fe–mTA complex structure at pH 4.5, based on the experimental results. The pH cannot be explicitly modelled, so the tartrate ligands are modelled as completely deprotonated at pH 4.5, based on iron citrate crystal structure and the literature [7–11]. Furthermore, the Fe–mTA structure shows antiferromagnetic coupling and is therefore a bin-

uclear complex at this pH. This is in agreement with the proposed molecular structure of Fe-mTA [6]. Therefore, we used this structure as a starting point for the molecular modelling (see Figure 4.5a).

The water molecule in the centre of the proposed complex (Figure 4.5a) immediately leaves the structure during the molecular mechanics simulation. The oxygen atoms of the *meso*-tartrate ligands also rearrange. This results in the structure shown in 4.5b. For one *meso*-tartrate ligand, one carboxyl oxygen and one hydroxy oxygen atom coordinate to one iron atom. The second hydroxy group forms a bridge between the two iron atoms, by coordinating to both atoms. The second carboxyl oxygen coordinates only to the second iron atom. This ligand is therefore coordinated to one iron atom with three bonds, and to the other iron atom with two bonds. The other ligand coordinates identically, but is inversed centrosymmetrically. Therefore, each iron atom has five coordinating oxygen atoms from the *meso*-tartrate ligands. Each iron atom is exposed to the outside of the complex, allowing one water molecule to coordinate to each iron atom as a sixth ligand. Six-fold octahedral coordination is a favourable environment for iron atoms.

Refining this structure using molecular dynamics, which takes quantum mechanical effects into account, results in the structure shown in Figure 4.5c, while Figure 4.5d shows a zoomed-in image of the environment of an iron atom in this complex. The six coordinating oxygen atoms form a distorted octahedron around each iron atom. The O-Fe-O angles vary between 83 and 105° and the Fe-O bond lengths vary from 1.92 to 2.04 Å. The distortion is in agreement with the high rhombicity of the iron environment in Fe-mTA, as was detected using EPR (see Figure 4.4). The two octahedrons in the Fe-mTA complex are edge-shared through the bridging deprotonated hydroxy groups, similar to the Fe-citrate complex (compare Figures 4.1 and 4.5c). This explains the antiferromagnetic coupling [23] that was observed in Figure 4.2. So, the simulated structure is in excellent agreement with our experimental results.

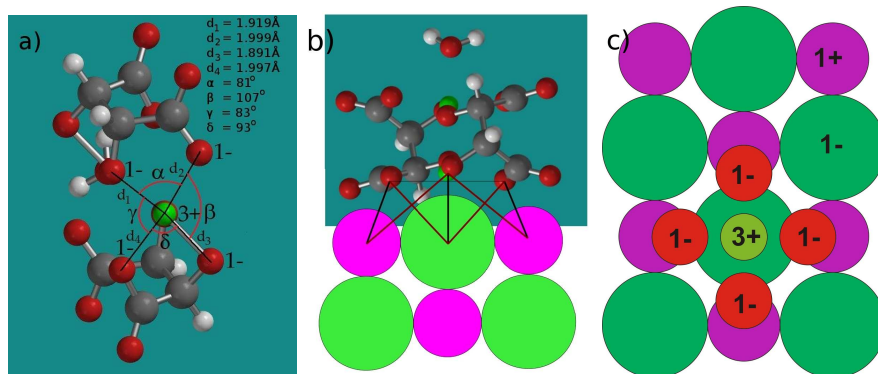


FIGURE 4.6: The proposed adsorption geometry. The Fe–mTA complex shown in Figure 4.5c is very flat when the water molecule is removed. a) Removal of the water molecule reveals a highly charged site. The charges are almost at right angles and the distances are approximately 2 Å. This charge distribution may allow adsorption onto the sodium chloride {100} surface, of which the angles Na–Cl–Na are 90° and the Na–Cl distances are 2.8 Å. b) Side view of the proposed adsorption geometry. c) Top view of this geometry, only showing the NaCl surface and the iron and oxygen atoms involved in the adsorption. Colour codes in the graphs: grey: carbon, red: oxygen, white: hydrogen, small green: iron, purple: sodium and large green atoms: chloride.

### 4.3.6 Adsorption geometry of the Fe–mTA complex

Recently, it was shown that the Fe–mTA complex is able to block crystal growth of sodium chloride by pinning the propagation of steps on the NaCl {100} surface [4]. This indicates that this complex is firmly adsorbed on this surface. When studying the structure obtained from molecular modelling, a possible binding mechanism is found. It is based on the observation that the top side of the complex where the water molecule is adsorbed is very flat. When this water molecule is removed, a surface is revealed with the positively charged iron atom at the centre, surrounded by four negatively charged oxygen atoms, as is shown in Figure 4.6a. These charges are distributed at roughly 90° angles to each other, resembling the symmetry of the {100} NaCl surface.

It is proposed that the water molecule of the Fe–mTA complex desorbs, and subsequently the iron atom coordinates to the NaCl surface above a chloride ion. The surrounding oxygen atoms will coordinate to the sodium ions adjacent to the chloride ion. This

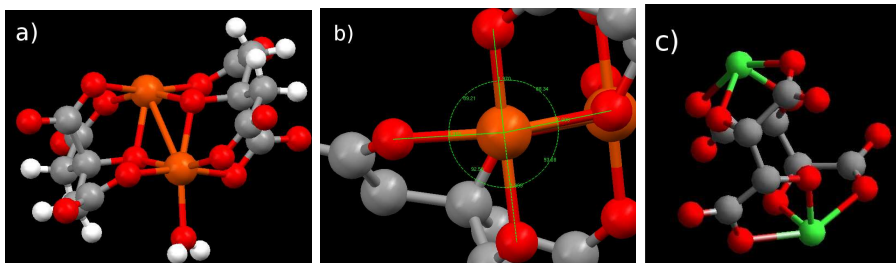


FIGURE 4.7: Other binuclear complexes to be compared with the Fe-mTA structure of Figure 4.5 and 4.6. a) Flat side of the Fe-citrate complex, comparable to Figures 4.6b and c. Though a part sticks out, the iron site is exposed and should be able to attach to the NaCl {100} surface, especially at step sites. b) Expansion of the coordination site in the Fe-citrate complex. The structure is very similar to Figure 4.6a. Fe-O bond lengths are 1.97 – 2.00 Å and the angles are 88 – 93° c) Binuclear complex of antimony with LD-tartrate [7]. This complex does not have bridging oxygen atoms and the metal atoms stick out. The Fe-LDTA and Fe-LTA complexes are expected to be very similar. Colour codes: grey: carbon, red: oxygen, white: hydrogen, orange: iron and green: antimony.

adsorption geometry is shown in Figures 4.6b and c. Another argument for this adsorption geometry is that the Fe-citrate complex, which is also an active anticaking agent, has a very similar charge distribution when the adsorbed water molecule is removed, as is shown in Figures 4.7a and b. Thus the adsorption geometry of the Fe-citrate complex is probably similar to the adsorption geometry proposed for the Fe-mTA complex.

For the proposed geometry to work, one water molecule has to be removed from the Fe-mTA complex. Furthermore, four water molecules have to be removed from the sodium chloride crystal surface, since there is one water molecule adsorbed onto each sodium ion on the clean sodium chloride {100} surface at high humidity [28]. Energetically this is favourable, since an electrostatic Madelung calculation showed that the bonding energy between the complex and the surface is in the order of 2000 kJ/mol. In contrast, the bonding energy of a water molecule to an iron(III) ion is approximately 170 kJ/mol [29] and the bonding energy of a water molecule on a sodium chloride crystal is also approximately 170 kJ/mol [30].

An alternative adsorption geometry of the Fe–mTA complex is that it is embedded in the first layer; this cannot be excluded from our present observations. However, it is unlikely that the complex is fully incorporated into the crystal, because of its overall charge. The charge can be neutralised at the surface by sodium ions from the liquid phase, but this cannot happen in the crystal. Therefore, the adsorbed complex will inhibit crystal growth.

A preliminary molecular mechanics simulation was performed in which the proposed adsorption geometry was tested. The complex was placed in contact with a sodium chloride {100} surface with a monatomic step. Though the molecule remains at the surface for a while, a water molecule adsorbs to it and the complex desorbs from the surface. This is probably due to the inaccuracy of the force field for binding energies between metals and ions, since molecular mechanics simulations are not very reliable for long-range interactions, which are important in ionic systems.

#### 4.3.7 Inactivity of Fe–LTA and Fe–LDTA

Figure 4.7c shows the crystal structure of a binuclear antimony *LD*–tartrate complex [7]. It is likely that the Fe–LTA and Fe–LDTA complexes are similar to this compound. This structure does not have bridging oxygen atoms and the metal atoms stick out. This complex does not show a square planar structure like Fe–mTA and Fe–citrate, as shown in Figures 4.6b and 4.7b. This probably explains why both Fe–LTA and Fe–LDTA are not active as anticaking agents for sodium chloride, in contrast to Fe–mTA and Fe–citrate.

### 4.4 Conclusion and Outlook

From our experiments we can conclude that the active anticaking agents Fe–mTA and Fe–citrate are both binuclear high spin iron(III) complexes, bridged by deprotonated hydroxy groups from their corresponding ligands. Simulation results indicate that a flat, almost square-planar coordination symmetry around the iron atom is typical for the anticaking activity of these complexes, since this

site allows adsorption to the NaCl {100} surface. In addition, the results show that the inactive iron tartrate complexes (Fe-LTA and Fe-LDTA) are also binuclear complexes, though the EPR experiments and comparison with the literature indicate that their internal structure is different, lacking the bridging hydroxyl groups and square-planar coordination symmetry. Therefore these complexes are not active anticaking agents at any pH.

Further research should be performed to confirm that the Fe-LTA and Fe-LDTA complexes indeed resemble the antimony-tartrate structure. Also, the proposed adsorption geometry on the NaCl {100} surface should be checked by molecular dynamics or density functional theory calculations, instead of molecular mechanics, since they are more reliable and do not depend on the force field. Finally a surface X-ray diffraction experiment should be performed to confirm our proposed adsorption geometry experimentally.

## Acknowledgement

The authors would like to thank Bas de Bruin and Paul Schlebos for performing the EPR experiments. Furthermore, we would like to acknowledge Paul Tinnemans for determining the iron(II)-mTA crystal structure, Jan Smits for the determination of the iron(III)-citrate crystal structure, Jelle Eygensteyn for performing the ICP-MS measurements and Rob Geertman for fruitful discussions. Finally, the authors acknowledge Akzo Nobel Industrial Chemicals and the Dutch Ministry of Economic Affairs for funding (EOS-KTO program, AgentschapNL).

## References

- [1] D.W. Kaufmann. *Sodium Chloride: the production and properties of salt and brine*. Reinhold, (1960).
- [2] M.A. van Damme-van Weele. *Influence of additives on the growth and dissolution of sodium chloride crystals*. PhD thesis, Technische Hogeschool Twente, Enschede, (1965).

- [3] R.M. Geertman. Use of carbohydrate-based metal complexes in non-caking salt compositions. US patent WO 00/59828, (2006).
- [4] A.A.C. Bode, S. Jiang, J.A.M. Meijer, W.J.P. van Enkevort, and E. Vlieg. *Cryst. Growth Des.*, (2012), **12**, 5889–5896.
- [5] A.A.C. Bode, V. Vonk, D.J. Kok, F.J. van den Bruele, A. Kerkenaar, M. Mantilla, S. Jiang, J.A.M. Meijer, W.J.P. van Enkevort, and E. Vlieg. *Cryst. Growth Des.*, (2012), **12**, 1919–1924.
- [6] R.M. Geertman. *VDI-Berichte*, (2005), **1901**, 557–562.
- [7] G.A. Kiosse, N.I. Golovastikov, and N.V. Belov. *Proc. Nat. Acad. Sci. USSR*, (1964), **155**, 545.
- [8] J.G. Forrest and C.K. Prout. *J. Chem. Soc. A*, (1967), **8**, 1312–1317.
- [9] B. Kamenar, D. Grdenic, and C.K. Prout. *Acta Cryst. B*, (1970), **26**, 181–188.
- [10] R.E. Tapscott, R.L. Belford, and I.C. Paul. *Coordin. Chem. Rev.*, (1969), **4**, 323–359.
- [11] R.E. Tapscott. *Inorg. Chim. Acta*, (1974), **10**, 183–189.
- [12] D.X. Li, D.J. Xu, and Y.Z. Xu. *Acta Cryst. E*, (2004), **60**, m1982–m1984.
- [13] In our laboratory, we determined that Fe(II)–mTA is isomorphic to the crystal structure of Co(II)–mTA[12] by mathing the XRPD spectrum of Fe(II)–mTA to a calculated XRPD spectrum. This spectrum was calculated from its crystal structure, which was obtained by replacing the cobalt(II) ion by an iron(II) ion in the crystal structure of Co(II)–mTA. The element replacement is justified since Co(II) and Fe(II) are adjacent in the periodic table, are both bivalent and have a comparable ionic radius, (88.8 and 92 pm).
- [14] C.F. Timberlake. *J. Chem. Soc.*, (1964), **Apr**, 1229–1240.

- [15] G.L. Robbins and R.E. Tapscott. *Inorg. Chem.*, (1976), **15**, 154–159.
- [16] M. Bobtelsky and J. Jordan. *J. Am. Chem. Soc.*, (1947), **69**, 2286–2290.
- [17] M.A. Ivanov and A.L. Kosoy. *Acta Cryst. B*, (1975), **31**, 2843–2848.
- [18] R.H. Crabtree. *The Organometallic Chemistry of the Transition Metals*. Wiley, Hoboken, NJ, USA, (2005).
- [19] I. Shweky, A. Bino, D.P. Goldberg, and S.J. Lippard. *Inorg. Chem.*, (1994), **33**, 5161–5262.
- [20] X. Hao, Y. Wei, and S. Zhang. *Transit. Met. Chem.*, (2001), **26**, 384–387.
- [21] G.M. Sheldrick. SADABS Program for Empirical Absorption Correction, (1996).
- [22] G.M. Sheldrick. SHELXL-97. Program for the refinement of crystal structures, (1997).
- [23] Y.G. Wei, S.W. Zhang, and M.C. Shao. *Polyhedron*, (1997), **16**, 2307–2313.
- [24] O. Kahn. *Inorg. Chim. Acta*, (1982), **62**, 3–14.
- [25] O. Kahn. *Angew. Chem. Int. Edit.*, (1985), **24**, 834–850.
- [26] C.E. Housecroft and A.G. Sharpe. *Inorganic Chemistry*. Pearson/Prentice Hall, 2<sup>nd</sup> edition, (2005).
- [27] W.R. Hagen. *Dalton Trans.*, (2006), 4415–4434.
- [28] J. Arsic, D.M. Kaminski, N. Radenovic, P. Poodt, W.S. Graswinckel, H.M. Cuppen, and E. Vlieg. *J. Chem. Phys.*, (2004), **120**, 9720–9724.
- [29] M. Rosi and Jr. C.W. Bauschlicher. *J. Chem. Phys.*, (1989), **12**, 7264–7272.
- [30] P.B. Barraclough and P.G. Hall. *Surf. Sci.*, (1974), **46**, 393–417.

## 4.5 Appendix



*Solutions of complexes in saturated brine. Top row: Fe(III)-mTA at pH -1 to 8. Second row: Fe(III)-citrate at pH -1 to 8. Third row: Fe(III) chloride at pH -1 to 7. Bottom row: Fe(III)-LTA (left) and Fe(III)-LDTA (right) at pH 0 and 4.5.*

## Chapter 5

# Influence of anticaking agents on the caking of sodium chloride at the powder and two-crystal scale

*Arno A.C. Bode, Melvin Verschuren, Martin Jansen, Shanfeng Jiang, Jan A.M. Meijer, Willem J.P. van Enckevort and Elias Vlieg*

### Abstract

The effectivity of the anticaking agents Ferrocyanide, Ferricyanide and Iron(III) *meso*-Tartaric Acid on the caking of sodium chloride was studied at the powder scale and on a two-crystal scale. Using the integrated stirring energy as a measure of caking strength of the powders gives results that agree well with industrial experience with these anticaking agents. For two single crystals, the required separation force was used as a measure for the caking strength. In this case, higher dosages of anticaking agents are required to prevent caking. This is caused by an increase in the number of contact points between the crystals, as was concluded from the surface morphology of the sodium chloride crystals, which we studied using atomic force microscopy. This change of the surface morphology is in turn caused by the applied anticaking agents. This shows that it is not only the surface area but also the number of contact points, and thus the particle size distribution, which are critical in determining the optimal dosage of anticaking agents on caking powders.

## 5.1 Introduction

Caking, or the agglomeration of a free-flowing powder into lumps, is a major problem when handling solid hygroscopic crystalline materials, and has therefore been studied for a long time [1, 2]. It is caused by partial dissolution and subsequent recrystallisation of the solid during humidity variation of the environment. When handling small amounts of material, caking can be prevented by keeping the material dry, or by adding a drying agent like rice or silica gel particles. However, at large scale this is no longer possible, and anticaking agents are required.

Sodium chloride (NaCl) is a well known example of such a material. When used as table salt, caking can easily be prevented by adding some rice to a salt shaker. However, most of the sodium chloride produced is used by the chemical industry for the production of chlorine gas ( $\text{Cl}_2$ ) by electrolysis, for which many tonnes of salt are shipped. At this scale, caking must be prevented by an anticaking agent. For sodium chloride, many anticaking agents are known [3]. Anticaking agents are usually crystal growth inhibitors [4]: by inhibiting crystal growth the crystals agglomerate much less. Since the 1950's, (sodium or potassium) Ferrocyanide ( $[\text{Fe}(\text{CN})_6]^{4-}$ ) has been the most common anticaking agent for sodium chloride globally, and its influence on the growth of this crystal was already studied in 1965 [5]. The related compound (sodium or potassium) Ferricyanide ( $[\text{Fe}(\text{CN})_6]^{3-}$ ), though very similar in structure to Ferrocyanide, is not used as an anticaking agent. Ferricyanide also influences the growth of sodium chloride crystals [6].

Even though Ferrocyanide works very effectively as an anticaking agent, it has some drawbacks during electrolysis. The iron causes iron hydroxide ( $\text{Fe}(\text{OH})_3$ ) formation on the membrane and electrodes, and the nitrogen forms nitrogen trichloride ( $\text{NCl}_3$ ), an explosive gas. Because of its stability and ionic nature, Ferrocyanide is also difficult to remove prior to electrolysis. Therefore, a new anticaking agent, Iron(III) *meso*-Tartaric Acid (Fe-mTA, a 1:1 molar mixture of  $\text{FeCl}_3$  and *meso*- $\text{C}_4\text{H}_6\text{O}_6$ , active at pH 4 – 5), was developed [7, 8]. This anticaking agent is nearly as effective as

Ferrocyanide, but less stable and therefore the iron can more easily be removed prior to electrolysis by adding lye. Also, it does not contain nitrogen, so no nitrogen trichloride gas is formed from it. Recently, we showed how both agents inhibit the crystal growth of sodium chloride at the nanometre scale [9, 10].

However, the translation from growth inhibition at the nanometre scale to the prevention of caking at a bulk scale is not trivial. The nanometre scale experiments were performed in idealised systems and on very smooth surfaces. It is known that also parameters like water adsorption, deliquescence and moisture migration [11–14], as well as the contact angle and the amount of contact points between particles are very important in caking [15]. Caking has been studied mainly at the powder scale, by measuring the flowability of a material [16, 17].

While the process of solid bridge formation is the major caking mechanism in hygroscopic crystalline powders [18], only a few studies have been performed that looked at the actual contact point between individual, polycrystalline, particles and studied the solid bridge formation between those particles [19–22]. Also the effect of anticaking agents on the caking of powders has been studied surprisingly little [23, 24].

In this paper we investigate the process of caking and the influence of anticaking agents thereon at the powder and at the two-crystal scale, in order to show that growth inhibition on the crystal surface at the nanometre scale and anticaking of materials at the powder scale are essentially the same phenomena.

## **5.2 Experimental**

Two different types of experiments were performed. Caking was studied at the powder scale using a rheometer test. At the two-crystal scale, we used cleaved sodium chloride crystals and measured the bond strength between them using a pulley and a balance. In both cases, the force needed to break the bonds between

the caked crystals is measured. This force has been measured for untreated sodium chloride and for sodium chloride treated with increasing amounts of anticaking agent. Various anticaking agents and related compounds were tested.

### 5.2.1 Powder Cake Strength

A method using a rheometer (Powder Flow Analyzer type TA-XT21, Stable Micro Systems) was developed to compare the caking behaviour of sodium chloride samples. The rheometer measures the torque required to turn a two-fold segmented, twisted blade through a (caked) powder while slowly moving downward, forcing the powder to flow in a reproducible manner. The forces required for the deformation and flow of the powder were recorded and plotted against the distance travelled by the blade through the sample. The integral of this curve is proportional to the dissipated energy, which is a measure for the cake strength.

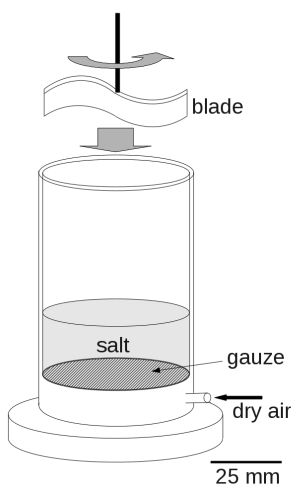


FIGURE 5.1: The used aeration cylinders. The sample was placed in the cylinder on top of the gauze, compressed and afterwards dried by the air flow from the bottom.

In each experiment, the blade rotated at 0.2 rad/s while moving down at a rate of 0.43 mm/s, until it reached a depth of 10 millimetre into the powder. The torque was recorded continuously. The

integral of the force versus travelling depth was calculated from 4 to 8 millimetres into the sample, ignoring the surface of the sample, since the surface is often strongly, but irreproducibly caked. This integral, which represents the energy required to break the caked powder, was taken as a measure for the cake strength of the sample.

Samples were prepared by filling a sealable plastic bag with  $49 \pm 0.1$  g of sodium chloride of high purity. An identical particle size distribution for all samples was obtained by "splitting" a larger sample. The average particle size was  $300 \pm 20 \mu\text{m}$ . To this bag one gram of demineralised water was added, in which the anticaking agent had been dissolved. This corresponds to 2.5% water content, which is comparable to salt production conditions. The bag was closed and the salt and water were mixed for about 5 minutes, until a visually homogeneous mixture was obtained. Then, the salt was transferred to an aeration cylinder (see Figure 5.1).

In the cylinder the sample surface was smoothened and the sample was compressed using the rheometer. A pestle was placed on top of the sample and pressure was applied by the rheometer up to 1 kg, while rotating the pestle at 0.4 rad/s. After compressing, the pestle was removed and the sample was dried by dry air, which was introduced through a gauze at the bottom of the cylinder, at 1.5 litres per minute for at least 80 minutes. The sample was weighed before and after drying, in order to ensure the water had completely been evaporated.

After drying, the cylinder was transferred to the rheometer and the cake energy was measured. To check the reproducibility of the data, each sample condition was measured at least 4 times. The average caking energies were compared with the caking energy for clean sodium chloride, resulting in Relative Caking Energies (RCE), which were used for the evaluation of the results.

RCE values were measured for several anticaking agents at several concentrations, given in parts per million (ppm). In the pow-

der cake experiments, ppm is defined as mol active substance per  $10^6$  mol solid sodium chloride. For potassium Ferrocyanide the concentrations were 0.8, 1.1 and 2.0 ppm and for potassium Ferri-cyanide the concentrations were 0.07, 0.14, 0.3 and 0.6 ppm. Further concentrations were measured, but using a different batch of NaCl. Even though each set of data is internally consistent, it is not possible to compare data between batches, because the difference in the particle size distribution and particle roughness lead to systematic differences. For the analysis, we used the most complete data set.

Since tartaric acid has two identical chiral centres, it has three stereoisomers: the optically active *L* and *D* isomers, and the optically inactive *meso* isomer. A racemic mixture of the *L* and *D* isomers is referred to as *LD*-tartaric acid [25]. Since *L* and *D* tartaric acid are each others mirror images, they cannot have a different effect on an achiral crystal like NaCl. Therefore, we only studied the pure *L*-isomer. The racemic mixture *LD*-tartaric acid can form mixed complexes and therefore can have different properties than the *L*-isomer. Analogous to the definition of Fe-mTA, iron(III) *L*-tartrate is denoted as Fe-LTA and iron(III) *LD*-tartrate as Fe-LDTA.

Fe-mTA and its stereoisomerically related compounds Fe-LTA and Fe-LDTA were studied at pH 2 and pH 4.5. At pH 2, Fe-mTA, Fe-LTA and Fe-LDTA were studied at 3.15 and 6.3 ppm. At pH 4.5, Fe-mTA was studied at 2.1, 4.2, 6.3 and 8.4 ppm, while Fe-LTA and Fe-LDTA were studied at 12.6 ppm.

### 5.2.2 Two-crystal Cake Strength

In addition to the experiments on powders, experiments were performed on two individual crystals to investigate the caking bond strength and the influence of the anticaking agents on this bond strength. In these experiments, caking was simulated by first placing the crystals in a humid environment for one hour, and afterwards drying them using a dry nitrogen flow. Cubic, {100}-facetted crystals were used, cleaved from melt-grown sodium chloride

crystals, which were purchased from Ted Pella, Inc (Redding, Ca, USA).

The crystals had an approximate size of  $3 \times 3 \times 4$  millimetre<sup>3</sup>, and the contact surfaces were polished using a polishing cloth, in order to make them equally rough. The bottom crystal was glued to a small weight, and an aqueous solution ( $12.5 \mu\text{l}$ ) containing the anticaking agent was applied to the top face of this crystal. After the droplet had almost completely evaporated, the upper crystal, on top of which a small hook was glued, was placed on top of the bottom crystal. The top crystal was rotated by  $45^\circ$  in order to avoid epitaxial matching, since this would greatly increase the cake bond strength and will rarely occur in a bulk sample.

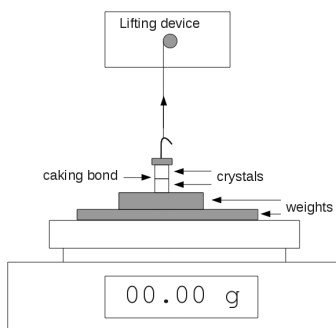


FIGURE 5.2: *Sketch of the set-up used to investigate the caking bond strength between individual crystals.*

After preparation, the stack of crystals was placed in a desiccator at a relative humidity (RH) of 75%, to simulate caking at high humidity. This humidity was maintained by a saturated sodium chloride solution at the bottom of the desiccator. The desiccator was slightly warmed up by placing it on a hot plate set at  $50^\circ\text{C}$  for one hour in order to speed up evaporation. The temperature in the desiccator increased only a few degrees, which did not influence the experiments since both the solubility and deliquescence humidity of sodium chloride are almost independent of the temperature. Under these conditions, the crystals attract water and will slightly dissolve.

Afterwards, the crystals were removed from the desiccator, and placed in a different one in which the crystals were dried by a constant dry nitrogen flow for at least one hour. In this period, the attracted water is evaporated and the dissolved sodium chloride will recrystallise, forming a solid bridge between the two crystals. After drying, the stack was removed from the dry environment and subsequently placed on a balance in order to measure the cake bond strength (see Figure 5.2).

The cake bond strength was measured by attaching the hook at the top crystal to a home-built lifting device and attaching a second, heavier weight to increase the maximum pulling force. This crystal stack-weight assembly is weighed by the balance during pulling. The lifting device pulls at a very slow, but constant rate, avoiding breaking of the caking bond by an initial shock. The hook and the pulling direction were centred exactly to prevent tilting of the crystals and thereby introducing a torsion force to the system. The reading of the balance is recorded at the moment the bond breaks. Like the powder caking experiments, we report the cake bond strength relative to the value for the clean crystals, as a relative caking force (RCF).

To compare the results of the two-crystal experiments with the powder caking experiments, a method is required to compare the applied concentrations of the anticaking agents, because the surface to volume ratio is very different in both experiments, and anticaking agents are surface active substances. Therefore, the concentrations were rescaled to the surface of the powder particles. For cubic particles with an average size of  $300\text{ }\mu\text{m}$ , 1 mol of NaCl represents an area of  $0.54\text{ m}^2$ . Therefore, 1 ppm of anticaking agent is equivalent to a coverage of  $1.85 \times 10^{-6}\text{ mol/m}^2$ . This coverage is defined as 1 ppm in the two-crystal (and surface morphology) experiments.

The two-crystal caking experiments were performed with three different anticaking agents: Ferrocyanide, Ferricyanide and Fe-mTA. Ferrocyanide was studied at 0.7, 14, 17.5, 21, 24.5, 28, 35 and 70 ppm, Ferricyanide at 7, 14, 17.5 and 35 ppm and Fe-mTA at 5,

53 and 182 ppm. The anticaking agents were applied using a small 12.5  $\mu\text{l}$  water droplet in order to minimise surface roughening.

### 5.2.3 Surface Roughening

The crystal surface roughening was studied using atomic force microscopy (AFM). Anticaking agents (14 ppm) were applied to cleaved single crystal surfaces and then treated according to the procedure followed for the two-crystal experiments, except for the stacking of the crystals. The resulting surface morphology was mapped using a Dimension 3100 AFM in contact mode, with commercial silicon nitride tips.

## 5.3 Results

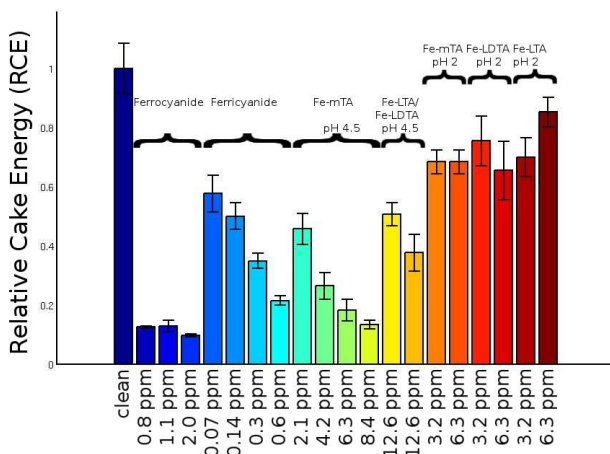


FIGURE 5.3: RCE values for all studied anticaking agents: Ferro- and Ferricyanide, iron(III) tartrates at pH 4.5 and at pH 2. Both Ferro- and Ferricyanide are effective anticaking agents. At pH 2, none of the iron tartrates are effective anticaking agents, while at pH 4.5 Fe-mTA is effective. The other tartrates are much less active even at higher dosages. For Fe-mTA and Ferricyanide we found that reducing the concentration reduces the effectivity, although the effectivity of Ferrocyanide is not improved further at dosages above 0.8 ppm.

### 5.3.1 Powder Cake Strength

Figure 5.3 shows the results of the rheometer experiments on powder caking. The method using the integrated energy gives relatively small experimental variation, 2 – 18%, at 4 experiments per condition. Such errors are small compared to other test methods, especially in the case of heavily caked powders [16]. The results are in agreement with industrial experience, since 1.4 and 5 ppm are used for Ferrocyanide and Fe-mTA respectively. In Figure 5.3 it can be seen that Ferrocyanide is a very good anticaking agent at a dosage of 0.8 ppm. Raising the dosage further does not result in significantly better anticaking. Figure 5.3 also shows that Ferricyanide is approximately just as effective as Ferrocyanide: at a dosage of 0.6 ppm, it is nearly as good as Ferrocyanide at 0.8 ppm. Lowering the dosage of Ferricyanide shows a reduction in anticaking effectivity. We were not able to compare the data to the low concentrations of Ferrocyanide, since these were obtained on an other batch of NaCl. However, it is very probable that the anticaking effectivity for Ferrocyanide also decreases at lower concentrations, as this is also known from industrial practice.

From Figure 5.3 it can be seen that Fe-mTA is a good anticaking agent at pH 4.5, with an increasing effectivity for increasing dosage. Even though the dosages of Fe-LTA and Fe-LDTA at pH 4.5 are relatively high, their anticaking effect is still limited. It can be seen that none of the iron(III) tartrates are good anticaking agents at pH 2. The caking strength is reduced by only 20 – 30% as compared to clean NaCl, which is insufficient to prevent caking.

### 5.3.2 Two-crystal Cake Strength

The results from the two-crystal caking experiments are shown in Figure 5.4. This method results in larger experimental variation than the rheometer method, therefore more experiments (10–20) were performed per condition. The results were tested for significance using the Mann-Whitney U-test [26], the significance criterion used was 5%. The experimental variation becomes especially large at the concentration where the anticaking agents start working, since at these concentrations about half the samples were

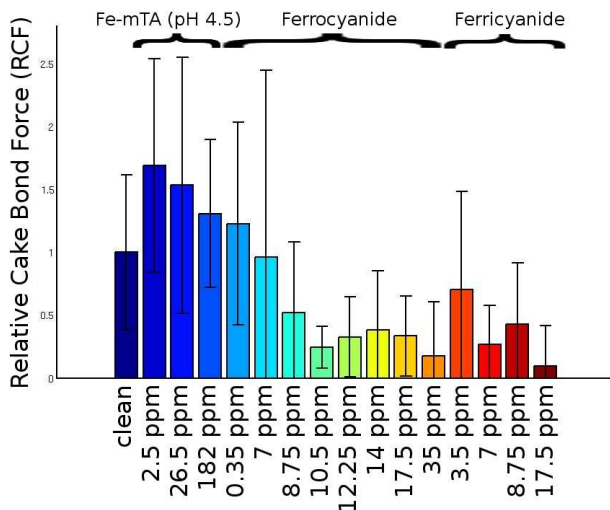


FIGURE 5.4: RCF values for crystals treated with various amounts of Ferrocyanide, Ferricyanide and Fe-mTA at pH 4.5. No significant decrease of caking is found for Fe-mTA, whereas Ferrocyanide and Ferricyanide strongly reduce caking. However, both Ferro- and Ferricyanide require a much higher dosage than required to reduce powder caking (see Figure 5.3).

nearly uncaked, while the other half of the samples were strongly caked.

Figure 5.4 as well as statistical analysis clearly show that Ferrocyanide and Ferricyanide both reduce the caking bond strength, while Figure 5.4 also shows that Fe-mTA is not effective. Ferrocyanide reduces the cake strength significantly at 8.75 ppm and higher. Ferricyanide also reduces the cake strength significantly, at 7 ppm and higher. Fe-mTA does not reduce cake strength at the applied concentrations and even seems to enhance it. However, this enhancement is not statistically significant. Since Fe-mTA did not reduce caking in the two-crystal experiments, the inactive Fe-LTA and Fe-LDTA compounds were not studied using this method.

### 5.3.3 Surface Roughening

Figure 5.5 shows the surface morphology of NaCl, clean and after treatment with anticaking agents and after exposure to humid (RH

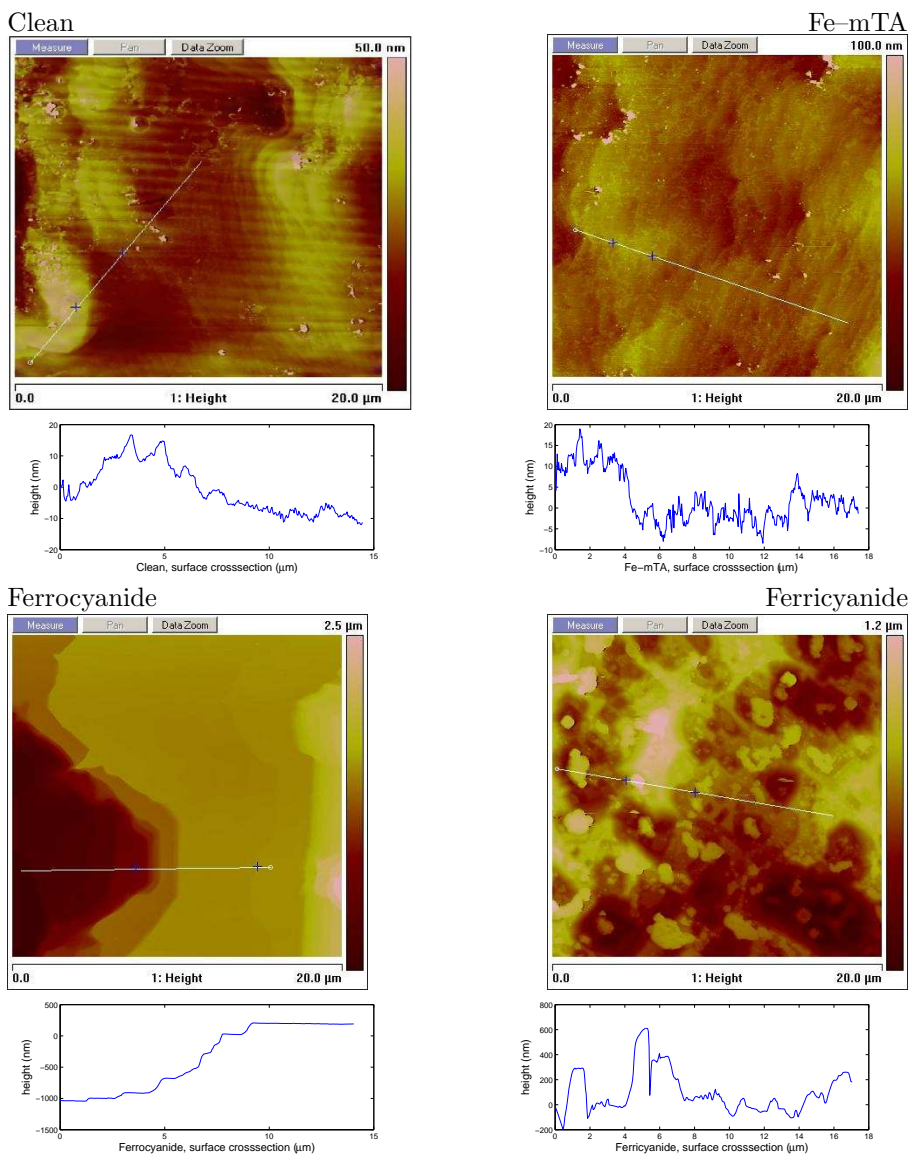


FIGURE 5.5: Surface morphology and cross-sections of the clean NaCl surface and after application of anticaking agents (14 ppm), both after exposure to 75% RH. Top left) clean surface; top right) Fe-mTA; bottom left) Ferrocyanide; bottom right) Ferricyanide.

= 75%) air. As expected, dissolution in the adsorbed water layer and subsequent recrystallisation of the surface layer, causes some roughening, even on the clean crystals. For clean surfaces, some spikes are formed of 100 – 500 nm height. In between these, the surface is relatively smooth, with macrosteps of 5 – 10 nm height.

Surfaces treated with Fe-mTA look quite similar to the clean surface. Similar spikes are formed, though more than on the clean surface. They are somewhat lower, 100 – 250 nm. In between, the surface is also relatively smooth, with features of 5 – 10 nm height.

Ferrocyanide and Ferricyanide cause a very different surface morphology. The surfaces look very rough, with macrosteps and hillocks of 100 – 500 nm high. The surface treated with Ferrocyanide has less macrosteps than the surface treated with Ferricyanide, and it has large, smooth terraces in between the macrosteps, on which the steps are 2 – 5 nm high. The surface treated with Ferricyanide does not have these terraces, and consists of many more hillocks.

## **5.4 Discussion**

At the powder scale, the anticaking agents behave more or less as expected. The dosage required for good anticaking corresponds well to the industrial experience. For Ferricyanide and Fe-mTA (at pH 4.5), the anticaking effect is found to decrease at lower dosage. For Ferrocyanide and Fe-mTA, we found that increasing the dosage above the industrially applied amount (1 ppm and 5 ppm respectively) does not improve the anticaking effectivity significantly. Also Ferricyanide is found to be a good anticaking agent, only slightly weaker than Ferrocyanide.

The fact that Fe-mTA is not effective at pH 2 is probably caused by a difference in the complexation, since the colour of the solution changes from yellow (pH 2) to green (pH 4–5). The colour of the Fe-LTA and Fe-LDTA also changes, namely from yellow (pH 2) to red (pH 4–5), but both complexes are almost inactive as an anticaking agent at each pH condition. The relation between the

complexation of the iron tartrates and their anticaking activity will be elaborated on elsewhere [27].

At the two-crystal scale, the results deviate from those at the powder scale. Ferro- and Ferricyanide do reduce the caking bond strength, however they require a much higher concentration than in the powder scale experiments: 20 – 30 ppm versus 1 ppm at the powder scale. Fe-mTA does not seem to work at all.

This difference can be explained from the surface roughness, because it increases the number of contact points between the crystals. The more contact points, the stronger the crystals will cake [28]. At the powder scale, the number of contact points will be approximately one per side face, as the crystals are expected to form mainly edge/vertex-surface contacts. This also explains that the particle size distribution is very important in preventing caking, since small particles will have the same amount of contact point per particle, but more contact points per unit of mass.

In the two-crystal experiments, the crystal surfaces are in near-perfect contact and therefore will have much more contact points, depending on the surface roughness. The surfaces roughened by the anticaking agents Ferro- and Ferricyanide will have contact points at each local maximum. Therefore, a higher concentration of anticaking agent is required than at the powder scale.

The smoother surfaces formed by Fe-mTA will have even more contact points, since there are relatively few spikes of only 100 – 250 nm: almost every hillock will be in contact with the other crystal. Therefore, even more contact points are present than in the case of Ferro- and Ferricyanide, requiring an even higher concentration of Fe-mTA. Unfortunately, this amount is above the solubility of Fe-mTA in water at pH 4.5, so we were not able to apply Fe-mTA in this amount.

## **5.5 Conclusion**

It is shown that both caking strength and the influence of anticaking agents on caking can be studied quantitatively and reproducibly at the powder scale and on the two-crystal scale. The experimental variation is very small at the powder scale, compared to other testing methods, and therefore the integrated energy method is recommended for caking strength measurements. The caking strengths are very reproducible within a single batch, but comparison between different batches is not possible owing to variations in particle size and roughness.

The effectivity of the anticaking agents at the powder scale is in good agreement with industrial experience. For Fe-mTA, the pH of the solution is critical for its anticaking effectivity. Furthermore, Ferricyanide is nearly as effective as an anticaking agent as Ferrocyanide.

Even though the same trends in anticaking effectivity can be detected at the two-crystal scale as on the powder scale, a higher amount of anticaking agent is required at the two-crystal scale. This is caused by the amount of contact points between the crystals and therefore by the surface roughness. However, from a qualitative point of view, no essential differences were found between the micro- and macroscopic scales. The observed differences are due to differences in surface morphology. Thus growth inhibition induced by the anticaking agents as observed in situ by AFM in the idealised microscopic systems [10] is the mechanism by which anticaking agents work at the bulk scale.

## **Acknowledgement**

The authors would like to acknowledge G. Smit and R. Vaessen for the development of the cake strength test using the rheometer. Furthermore, the authors acknowledge Akzo Nobel Industrial Chemicals and the Dutch Ministry of Economic Affairs for funding (EOS-KTO Program, AgentschapNL).

## References

- [1] T.M. Lowry and F.C. Hemmings. *J. Soc. Chem. Ind. (London)*, (1920), **39**, 101T.
- [2] J.R. Adams and A.R. Merz. *Ind. Eng. Chem.*, (1929), **21**, 305.
- [3] D.W. Kaufmann. *Sodium Chloride: the production and properties of salt and brine*. Reinhold, (1960).
- [4] Y.L. Chen and J.Y. Chou. *Powder Technol.*, (1993), **77**, 1–6.
- [5] M.A. van Damme-van Weele. *Influence of additives on the growth and dissolution of sodium chloride crystals*. PhD thesis, Technische Hogeschool Twente, Enschede, (1965).
- [6] R. Boistelle. *Contribution à la connaissance des formes de croissance du chlorure de sodium*. PhD thesis, Université de Nancy, (1966).
- [7] R.M. Geertman. Use of carbohydrate-based metal complexes in non-caking salt compositions. US patent WO 00/59828, (2006).
- [8] J.A.M. Meijer. *9<sup>th</sup> Int. Symp. on Salt*, (2009), **1**, 108–116.
- [9] A.A.C. Bode, V. Vonk, D.J. Kok, F.J. van den Bruele, A. Kerkenaar, M. Mantilla, S. Jiang, J.A.M. Meijer, W.J.P. van Enkevort, and E. Vlieg. *Cryst. Growth Des.*, (2012), **12**, 1919–1924.
- [10] A.A.C. Bode, S. Jiang, J.A.M. Meijer, W.J.P. van Enkevort, and E. Vlieg. *Cryst. Growth Des.*, (2012), **12**, 5889–5896.
- [11] M.C. Leaper, M.S.A. Bradley, J.A.S. Cleaver, I. Bridle, A.R. Reed, H. Abou-Chakra, and U. Tüzün. *Adv. Powder Technol.*, (2002), **13**, 411–424.
- [12] M. Mathlouthi and B. Rogé. *Food Chem.*, (2003), **82**, 61–71.
- [13] S.W. Billings, J.E. Bronlund, and A.H.J. Paterson. *J. Food Eng.*, (2006), **77**, 887–895.
- [14] A.K. Salameh and L.S. Taylor. *Pharm. Dev. Technol.*, (2006), **11**, 453–464.

- [15] Y.Wang, R.W. Evitts, and R.W. Besant. *Can. J. Chem. Eng.*, (2008), **86**, 192–198.
- [16] J. Schwedes. *Gran. Matt.*, (2003), **5**, 1–43.
- [17] J.J. Fitzpatrick, N. Descamps, K. O’Meara, C. Jones, D. Walsch, and M. Spitere. *Powder Technol.*, (2010), **204**, 131–137.
- [18] H. Rumpf. *The strength of granules and agglomerates*, page 379. John Wiley and Sons, New York, NY, (1962).
- [19] J.A.S. Cleaver, G. Karatzas, S. Louis, and I. Hayati. *Powder Technol.*, (2004), **146**, 93–101.
- [20] U. Bröckel, M. Wahl, R. Kirsch, and H.J. Feise. *Chem. Eng. Technol.*, (2006), **29**, 691–695.
- [21] M. Wahl, R. Kirsch, S. Trapp, and M. Bottlinger. *Chem. Eng. Technol.*, (2006), **29**, 674–678.
- [22] M. Wahl, U. Bröckel, L. Brendel, H.J. Feise, B. Weigl, M. Röck, and J. Schwedes. *Powder Technol.*, (2008), **188**, 147–152.
- [23] R.A. Lipasek, L.S. Taylor, and L.J. Mauer. *J. Food Sci.*, (2011), **76**, C1062–C1074.
- [24] A. Biskupski, P. Malinowski, P. Biskupski, and P. Rusek. *Przem. Chem.*, (2011), **90**, 696–698.
- [25] R.E. Tapscott, R.L. Belford, and I.C. Paul. *Coordin. Chem. Rev.*, (1969), **4**, 323–359.
- [26] F. Wilcoxon. *Biometrics Bull.*, (1945), **1**, 80–83.
- [27] A.A.C. Bode, S.J.C. Granneman, M.C. Feiters, P. Verwer, J.A.M. Meijer, W.J.P. van Enckevort, and E.Vlieg. Manuscript in preparation.
- [28] Y.Wang, R.W. Evitts, and R.W. Besant. *Can. J. Chem. Eng.*, (2008), **86**, 199–206.



## Chapter 6

# Sodium Chloride Dihydrate Crystals: Morphology, Nucleation, Growth and Inhibition

*Arno A.C. Bode, Paul G.M. Pulles, Martin Lutz, Ward J.M. Poullisse, Shanfeng Jiang, Jan A.M. Meijer, Willem J.P. van Enkevort and Elias Vlieg*

### Abstract

Sodium chloride powders have a strong tendency to cake at freezing temperatures, which is caused by the formation of sodium chloride dihydrate solid bridges in between the powder particles. Using the crystal structure, which was redetermined and improved, the morphology of the dihydrate crystals was determined. In addition, the growth rate of the most important facets of these crystals was measured, as well as the influence of a number of anticaking agents and related additives on the growth rate. A likely candidate for the inhibition of dihydrate growth was found: a mixture of iron(III) and *L*-tartaric acid, probably forming a metal-organic coordination complex. The nucleation rate of dihydrate was found to be extremely low and to increase with time. This is probably caused by the formation of a metastable prenucleation phase, which inhibits the nucleation of dihydrate crystals. The influence of the same additives on the nucleation rate was found to be limited. An increase in the nucleation rate was found in presence of a mixture of iron(III) and *meso*-tartaric acid, probably also forming a metal-organic coordination complex. It was found that Ferricyanide delays the nucleation of dihydrate crystals.

## 6.1 Introduction

Without precautions, sodium chloride (NaCl) crystalline powders easily agglomerate into lumps during storage, a process called caking [1]. This must be prevented because caked sodium chloride does not flow freely, seriously hampering its handling. Under normal conditions, caking can be prevented effectively using so-called anticaking agents. For sodium chloride, many effective anticaking agents are known, like potassium ferrocyanide and nitrilotriacetamide [2]. Recently, iron(III) *meso*-tartaric acid was introduced as an environmentally friendly alternative [3] to potassium ferrocyanide. These agents are applied in very low dosages of 1 to 5 parts per million (ppm) and are able to prevent caking very effectively by interacting with the crystal surface and thus inhibiting crystal growth [4–6].

Though caking of sodium chloride can be prevented very well at normal conditions, the used anticaking agents are not very effective under freezing conditions. This hampers the handling of sodium chloride powders in winter, especially in deicing applications. Therefore, a much higher dosage of the anticaking agent, up to 75 ppm for ferrocyanide, is required on deicing salt (road salt), raising concerns about damage to the environment [7].

The lower effectivity of the anticaking agents is likely linked to the formation of sodium chloride dihydrate,  $\text{NaCl} \cdot 2\text{H}_2\text{O}$  or hydrohalite, which is a stable form of sodium chloride in presence of water at temperatures below  $0.1^\circ\text{C}$  [8], see the phase diagram in Figure 6.1. This dihydrate form of sodium chloride has been studied surprisingly little. In 1974, its crystal structure was solved using X-ray diffraction [9]. The crystal is monoclinic,  $\beta$  is  $114.41^\circ$  and has space group  $P2_1/c$  and point group  $2/m$ . From the point group it can be concluded that the dihydrate crystals will have a twofold symmetry axis parallel to the b-axis and a mirror plane perpendicular to it.

Freezing out dihydrate crystals has been used as an alternative to evaporative crystallization of anhydrous NaCl [10]. Furthermore,

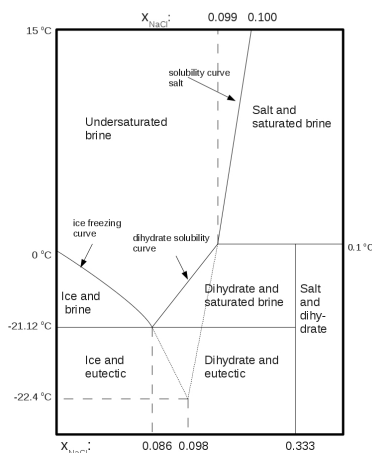


FIGURE 6.1: The phase diagram for the water – sodium chloride system [1]. Sodium chloride dihydrate forms at temperatures below 0.1 °C in the presence of water. Note that the figure is not to scale.

dihydrate formation may have been relevant in ice ages, forming a reflective crust of dihydrate crystals on the surface of sea ice, causing further cooling of the Earth surface [11].

While dihydrate crystals rapidly recrystallise to anhydrous NaCl and brine at temperatures above 0.1°C, NaCl does not easily recrystallise to the dihydrate form at lower temperatures, even in contact with a saturated sodium chloride solution. During storage, recrystallisation to the dihydrate form is limited by the availability of water. However, it is likely that the surface of the NaCl crystals is covered by a thin layer of the dihydrate, since there is always 3–5 w% water present in industrial conditions. Because of the presence of the dihydrate layer, the anticaking agents cannot interact with the NaCl surface but have to inhibit the growth of the dihydrate layer. Since the crystal structure of the dihydrate is very different from the structure of NaCl [9], it is likely that a molecule that interacts strongly with the NaCl surface, will not fit well on the dihydrate crystal surface. Therefore ferrocyanide probably does not inhibit the formation of the dihydrate, but inhibits the dissolution of the anhydrous NaCl, so less NaCl is available for

the formation of the dihydrate [2].

From an anticaking point of view, there are at least two ways to prevent caking of sodium chloride crystals at low temperature. The growth of dihydrate can be inhibited, thereby preventing dihydrate covered sodium chloride crystals from caking, or the formation of the dihydrate layer is prevented by inhibiting the nucleation of the dihydrate crystals. In this manner, caking can be prevented by anticaking agents for anhydrous sodium chloride, since no dihydrate layer is formed.

Therefore, we determined if a dihydrate layer is formed on the NaCl crystal surface below 0.1°C. Furthermore, the crystal structure and morphology of the dihydrate crystals was determined in order to investigate which faces are relevant for crystal growth inhibition by an anticaking agent for dihydrate. We investigated the influence of known anticaking agents for sodium chloride and several other additives on the crystal growth rate of these faces. Finally, we studied the influence of the same additives on the nucleation kinetics of dihydrate crystals.

## 6.2 Experimental

### 6.2.1 Crystal structure determination

First, we examined if the crystal structure of the dihydrate, as determined by Klewe *et al.* in 1974 [9] was correct using single crystal X-ray diffraction. Dihydrate crystals were grown by placing a vial containing a saturated sodium chloride solution in a freezer operating at -18 °C. A crystal was removed from the growth solution and was mounted under a low temperature nitrogen stream. [12] 36989 Reflections were measured on a Nonius KappaCCD diffractometer with rotating anode and graphite monochromator ( $\lambda = 0.71073$  Å) up to a resolution of  $(\sin \theta / \lambda)_{max} = 1.08$  Å<sup>-1</sup> at a temperature of 150(2) K. Intensity data were integrated with the Eval15 software. [13] Absorption correction and scaling was performed based on multiple measured reflections with SADABS [14] (0.69 – 0.75 correction range). 3972 Reflections were unique ( $R_{int} = 0.025$ ), of

which 3655 were observed [ $I > 2\sigma(I)$ ]. The initial coordinates for the refinement were taken from the literature. [9] They determined that the crystals are monoclinic, with space group is  $P2_1/c$ . The cell parameters they obtained were  $a = 6.3313(5)$  Å,  $b = 10.1178(9)$  Å,  $c = 6.5029(6)$  Å and  $\beta = 114.407(7)^\circ$ .

Least-squares refinement was performed against  $F^2$  of all reflections with the program SHELXL-97. [15] Non-hydrogen atoms were refined with anisotropic displacement parameters. Hydrogen atoms were located in difference Fourier maps and refined freely with isotropic displacement parameters. 54 Parameters were refined with no restraints.  $R1/wR2$  [ $I > 2\sigma(I)$ ]: 0.0156 / 0.0383.  $R1/wR2$  [all refl.]: 0.0176 / 0.0390.  $S = 1.069$ . Residual electron density between -0.44 and 0.49 e/Å<sup>3</sup>. Geometry calculations and checking for higher symmetry was performed with the PLATON program. [16]

### 6.2.2 Dihydrate growth on sodium chloride crystals

We checked our hypothesis that anhydrous sodium chloride crystals get covered by a layer of dihydrate in presence of water under freezing conditions. For this, a growth cell was used, shown in Figure 6.2, which was cooled using a Julabo F-25 recirculating cooler filled with a 40% ethylene glycol water mixture. The crystals were placed between two glass plates, in order to observe the growth using an optical microscope (Zeiss Axioplan 2). The glass plates were treated with Repelcote and dry nitrogen gas was flowed over them in order to prevent ice formation by water attracted from the air. A thermocouple was placed in the growth cell to determine the local temperature.

A small cubic crystal of anhydrous sodium chloride, about  $5 \times 5 \times 5$  mm in size, was placed in the growth cell and covered with a thin film of saturated sodium chloride solution. The cell was cooled down and micrographs were taken of the crystal surface in order to observe the dihydrate crystals forming on the surface.

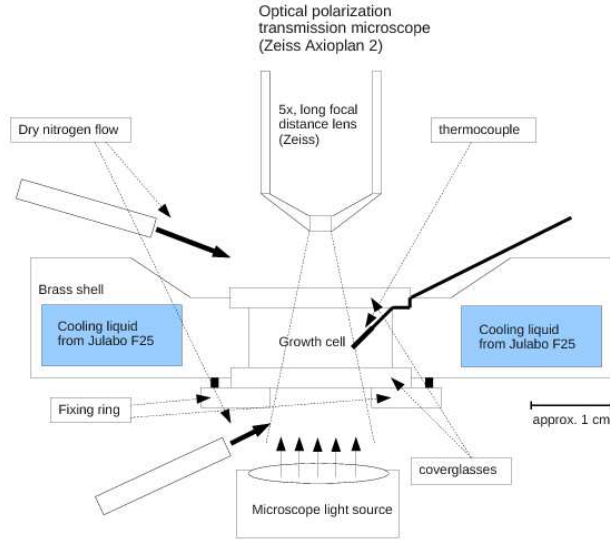


FIGURE 6.2: Setup used to grow dihydrate crystals for the morphology determination and the growth rate experiments.

### 6.2.3 Morphology and growth rate

Dihydrate crystals were grown in the closed growth cell, which was filled with a saturated sodium chloride solution. The solution was immediately cooled down, resulting in a solution supersaturated with respect to the dihydrate form. The supersaturation is defined as:

$$\sigma(\%) \equiv \frac{c - c_{sat}(T)}{c_{sat}(T)} \times 100, \quad (6.1)$$

in which  $\sigma$  is the supersaturation in %,  $c$  the concentration and  $c_{sat}(T)$  the saturation concentration, which is a function of the temperature  $T$ . For sodium chloride solutions saturated at 20 °C, the solubility is 359 g/l. Using the temperature dependence of the solubility of sodium chloride dihydrate,  $c_{sat}$  (see Figure 6.1), the supersaturation depends on the temperature  $T$  (in °) as:

$$\sigma(\%) = \frac{T - 1.16}{-0.00737T - 1.383}. \quad (6.2)$$

The temperature in the cell was approximately 10 degrees warmer than the recirculating fluid, which could be cooled down to  $-18^{\circ}\text{C}$ . At this temperature, the temperature in the growth cell is  $-8^{\circ}\text{C}$ , corresponding to a supersaturation of the dihydrate of approximately 7%, according to equation 6.2. The lowest possible supersaturation is reached at  $0.1^{\circ}\text{C}$ , corresponding to a supersaturation of 0.8%. By controlling the temperature of the cooling liquid, the supersaturation could therefore be varied between 0.8 and 7%.

Clean dihydrate crystals were grown from a clean saturated sodium chloride solution without any additives present. These crystals were used to determine the morphology of the dihydrate crystals. It was not possible to index the faces of the crystals using an optical goniometer, since the crystals are very unstable at room temperature. Therefore we had to index the faces by obtaining micrographs and using the symmetry of the crystal structure. Such micrographs were obtained from the top face of the crystals, and some crystals were placed on the side to obtain side view micrographs.

In addition, the growth rates of the various crystal faces were measured by taking micrographs of individual crystals with an interval of approximately 100 seconds. Even though the growth of the crystals should lower the supersaturation and thus the growth rate, the growth rate was found to be nearly constant for at least 2000 seconds. Therefore, the growth did not deplete the solution rapidly, enabling us to measure the growth rate of several crystals sequentially in the same sample. This was necessary due to the large spread in the observed growth rates.

Saturated sodium chloride solutions were prepared at room temperature and filtered in order to remove solid sodium chloride remaining. First, we measured the growth rate of dihydrate crystals in clean saturated solution. Then, the influence of additives was

studied. The additives were dissolved in the saturated solution at a concentration of 100 parts per million (ppm, molar) relative to the sodium chloride. This concentration is higher than the concentrations used in industrial practice. However, in order to detect any influence on the growth rate, such high concentrations were needed.

The additives used were the anticaking agents potassium ferrocyanide (**A**), iron(III) *meso*-tartaric acid ( $\text{Fe}^{\text{III}}$ -mTA, **B**) and iron(III) citrate (**C**), and other known crystal growth inhibitors for sodium chloride like cadmium(II) chloride (**D**), lead(II) chloride (**E**) and potassium ferricyanide (**F**). Furthermore, we investigated related compounds like iron(II) *meso*-tartaric acid ( $\text{Fe}^{\text{II}}$ -mTA, **G**), iron(II) citrate (**H**), iron(III) *LD*-tartaric acid ( $\text{Fe}^{\text{III}}$ -LDTA, **I**) and iron(III) *L*-tartaric acid ( $\text{Fe}^{\text{III}}$ -LTA, **J**). The pH of all iron citrate and iron tartrate solutions was set at 4.5 by adding sodium hydroxide, since this is the pH at which  $\text{Fe}^{\text{III}}$ -mTA and  $\text{Fe}^{\text{III}}$ -citrate are active anticaking agents for anhydrous sodium chloride. Note that no molecular or crystal structures are known for any of the iron(III) tartrates, however, the iron(III) citrate complex is a binuclear complex with antiferromagnetically coupled iron atoms [17, 18]. The structure of the  $\text{Fe}$ -mTA complex and its relation to the iron(III) citrate complex will be discussed elsewhere [19].

Some additional substances were tested as well. Trehalose (**K**), a sugar, was used at 1000 ppm because it was reported in the literature to prevent the formation of sodium chloride dihydrate [20]. We also investigated the influence of cerium(III) nitrate (**L**), since the ionic radius of the cerium(III) ion is roughly the same as the ionic radius of the sodium ion. We therefore assumed it might adsorb at sodium locations, while its charge would hamper further growth.

#### 6.2.4 Nucleation rate determination

The nucleation rate of dihydrate crystals was investigated using a freezer operating at  $-18 \pm 1$  °C. Small sample vials were placed in a large petri dish which was partially filled with cooling liquid (40%

ethelyne glycol water mixture) to ensure all samples were cooled to the same temperature.

Since it was not possible to vary the temperature in the freezer, another method of varying the supersaturation was required. The supersaturation of the dihydrate at -18 °C could be set by varying the initial concentration of sodium chloride. All samples contained 10 ml of saturated sodium chloride solution at 20 °C, and a little water was added to set the supersaturation. The supersaturation of the dihydrate solutions prepared in this way depends on the added amount of water as:

$$\sigma(\%) = \frac{154 - 100V}{10 - V}, \quad (6.3)$$

in which  $\sigma$  the supersaturation in percent and  $V$  the volume of water added to the solution, in ml.

We investigated the influence of the supersaturation on the nucleation rate of the dihydrate without additives. A series of samples was made with concentrations corresponding to supersaturations of 5, 10 and 15 percent at -18 °C. A sodium chloride solution, saturated at room temperature, was filtered to remove the solid. Water was added according to equation 6.3 in order to set the supersaturations. The added water results in an undersaturated solution at room temperature, removing all remaining solid NaCl, which would generate nucleation sites and thereby perturb the nucleation experiments.

Due to the stochastic nature of crystal nucleation, multiple samples per supersaturation were required. Therefore, at least 20 samples per supersaturation were used. The samples were checked for the presence of crystals by quickly removing them from the freezer and optical screening. These checks were performed daily, except for some weekend days. Vials containing crystals were counted and removed from the freezer. The vials were handled carefully in order to minimise agitating the solutions. The temperature in the freezer and in a sample vial was monitored using a thermocouple. Typically, the temperature inside the vial would be raised to -11

–  $-12^{\circ}\text{C}$  during the screening. The temperature recovery time was approximately 2 hours.

Subsequently, we investigated the influence of disturbing the solutions on the nucleation time, since agitating the solutions can speed up nucleation [21]. The experiment was performed by duplicating the previously described experiment, however 20 vials per supersaturation were thoroughly shaken after optical screening, and 20 vials were handled as carefully as possible. The data from the carefully handled vials were also used to check the reproducibility of the nucleation experiments. For this experiment, supersaturations of 5, 8, 10 and 15% were used, since the growth rate experiments were performed at 8% supersaturation. Then, we investigated the influence of the screening itself by duplicating the experiment again without shaking. The time between checking was varied between 1 and 12 days.

Finally, the nucleation rate of the dihydrate was studied under influence of various additives, including the anticaking agents for sodium chloride. In order to see the influence of the additives, a supersaturation of 5% was chosen, based on the nucleation rate of the clean system. The additives used were the same as those used in the growth rate experiments: the known anticaking agents for sodium chloride, known crystal growth inhibitors and related compounds at 100 ppm. The trehalose sugar and the active anticaking agents were also studied at 1000 ppm.

## 6.3 Results and Discussion

### 6.3.1 Crystal structure determination

The crystal structure of sodium chloride dihydrate was determined from the X-ray diffraction pattern. We confirm the structure as determined by Klewe *et al.* [9], but the resolution is slightly improved. The crystal structure is monoclinic with space group  $P2_1/c$  and  $\beta = 114.4252(1)^{\circ}$ ,  $a = 6.32184(7)$  Å,  $b = 10.11135(8)$  Å and  $c = 6.50351(4)$  Å, and  $Z = 4$ . The refined crystal structure will be submitted to the Inorganic Crystal Structure Database

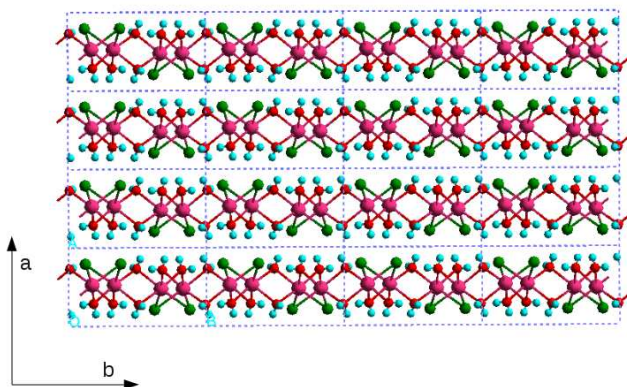


FIGURE 6.3: Crystal structure of the dihydrate crystals, viewed along the  $c$ -axis, showing layers parallel to the  $(100)$  plane and no bonds in the  $\langle 100 \rangle$  direction. Only weak  $O-H-Cl$  hydrogen bonding occurs. Green: chloride, purple: sodium, red: oxygen, blue: hydrogen.

(ICSD). This crystal structure shows layers of atoms connected by strong bonds in the  $bc$  or  $(100)$  plane. However, only weak interactions exist in the  $a$  or  $\langle 100 \rangle$  direction, as shown in Figure 6.3.

### 6.3.2 Morphology Determination

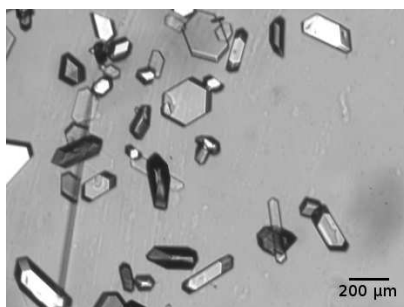


FIGURE 6.4: Several dihydrate crystals, most of them with the same face upward.

As can be seen from Figure 6.4, most dihydrate crystals grow with the same, nearly hexagonal face upward. This face is flanked

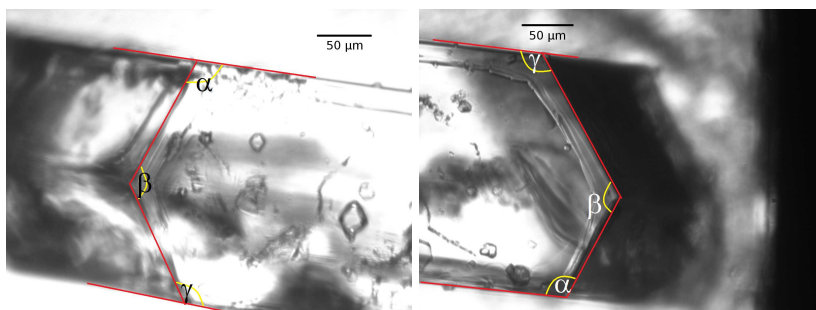


FIGURE 6.5: Detailed micrographs of the perpendicular side face of a typical dihydrate crystal, showing a two-fold rotation axis perpendicular to it. a) Left and b) Right side of the same side face.

by four side faces under an obtuse angle and two faces perpendicular to it. The crystals are usually quite thin compared to the size of the top face, especially when grown at  $-18^{\circ}\text{C}$ . The crystals are less plate-like when grown in the growth cell of Figure 6.2, which is probably due to the higher temperature and corresponding lower supersaturation.

In order to determine the Miller indices of the faces, micrographs of the top and side faces of a dihydrate crystal were made. Figure 6.5 shows micrographs of the perpendicular side face of a dihydrate crystal. The top angle,  $\beta$ , between the tilted side facets is  $124^{\circ}$ , the angle to the left of  $\beta$ ,  $\gamma$ , is  $122^{\circ}$ . The angle to the right of  $\beta$ ,  $\alpha$ , is  $114^{\circ}$ . This reveals the two-fold rotation axis perpendicular to this face, identifying it as a  $\{010\}$ -face.

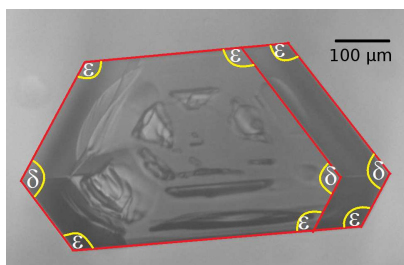


FIGURE 6.6: Detailed micrograph of the top face of a typical dihydrate crystal.

The angles of the top face were also measured, as shown in Figure 6.6. The angles were  $114.7 \pm 0.2^\circ$  for the angle  $\delta$  between the tilted side faces and  $122.4 \pm 0.6^\circ$  for the other side angles  $\epsilon$ . Therefore, the mirror plane of the  $2/m$  point group is perpendicular to this face.

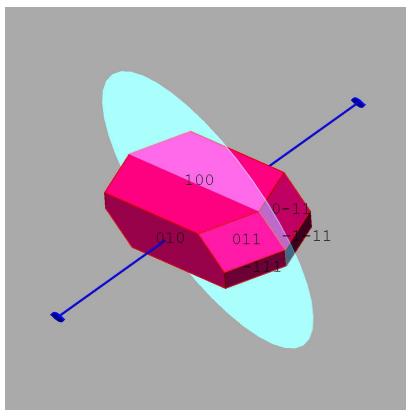


FIGURE 6.7: Calculated morphology of dihydrate crystals using the programme Shape<sup>©</sup> [22]. The top and bottom faces are the  $\{100\}$  faces, the perpendicular side faces are the  $\{010\}$  faces and the tilted faces are the  $\{110\}$  and  $\{11\bar{1}\}$  faces.

Using the program Shape<sup>©</sup> [22], crystal shapes were calculated from the crystal structure parameters. Using the angles determined from the micrographs, the other facets could be indexed. The top face is a  $\{100\}$ -face and the tilted side faces are the  $\{11\bar{1}\}$ -faces and the  $\{110\}$ -faces. A schematic representation of this morphology is shown in Figure 6.7.

This morphology is in agreement with the layered crystal structure: since these layers are parallel to the  $(100)$  plane it is likely that the growth rate of directions parallel to this plane are high compared to the direction perpendicular to it, resulting in thin plate-like crystals. This also explains why almost all crystals grow with the  $\{100\}$  face upward, since the initial nucleus will be thin in the  $\langle 100 \rangle$  direction, and will therefore lie flat on the bottom.

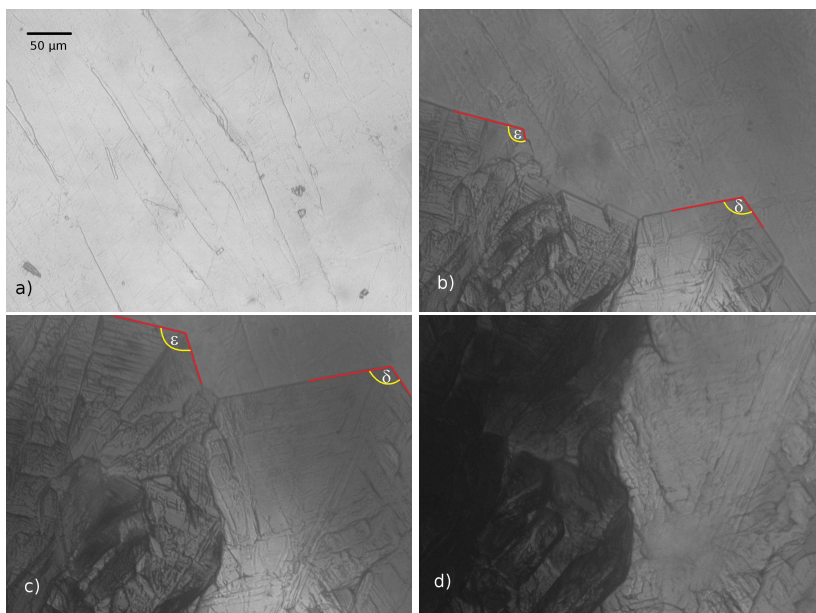


FIGURE 6.8: Formation of a dihydrate layer on an anhydrous sodium chloride crystal surface. Angles of corners correspond to the angles  $\delta$  and  $\epsilon$  of the  $\{100\}$ -faces (Figure 6.6). The time interval between the images is 15 minutes.

### 6.3.3 Dihydrate formation on sodium chloride

We tested our hypothesis that at temperatures below 0 °C a layer of dihydrate is formed on cubic, anhydrous sodium chloride crystals. Figure 6.8 shows the formation of a dihydrate layer on a cleaved sodium chloride  $\{100\}$  surface. The angles of the forming crystals match the angles  $\delta$  and  $\epsilon$  on the top face of the dihydrate crystal (see Figure 6.6), making the top face of the covering layer the  $\{100\}$  face of the dihydrate crystal.

This clearly shows that dihydrate does form on top of sodium chloride crystals and explains why the anticaking agents which interact with the sodium chloride crystal surface do not work very well at freezing temperatures. Since the outward face of the dihydrate crystals is the  $\{100\}$  face, an anticaking agent for these crystals should inhibit the growth of this face.

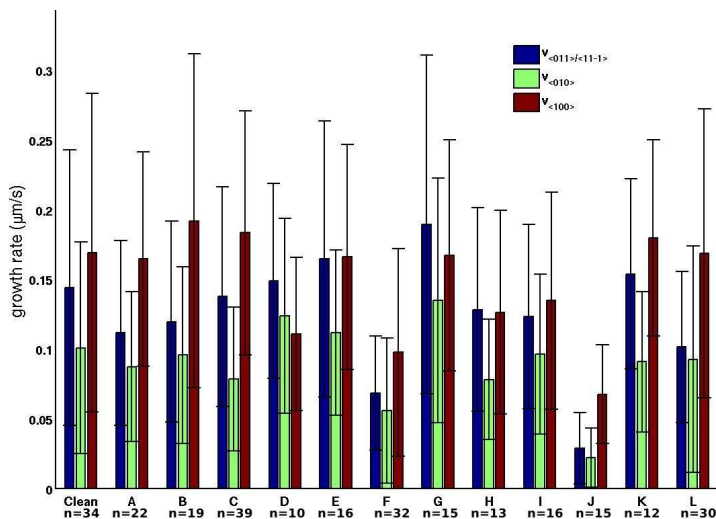


FIGURE 6.9: Growth rates of dihydrate crystals in the various crystal directions,  $v_{\langle 011 \rangle} / v_{\langle 11\bar{1} \rangle}$ ,  $v_{\langle 010 \rangle}$  and  $v_{\langle 100 \rangle}$ . Each set of bars represents the three growth rates in the presence of an additive. The first set shows the clean system, the others are **A**: ferrocyanide, **B**:  $\text{Fe}^{\text{III}}$ -mTA, **C**:  $\text{Fe}^{\text{III}}$ -citrate, **D**: cadmium chloride, **E**: lead chloride, **F**: ferricyanide, **G**:  $\text{Fe}^{\text{II}}$ -mTA, **H**:  $\text{Fe}^{\text{II}}$ -citrate, **I**:  $\text{Fe}^{\text{III}}$ -LDTA, **J**:  $\text{Fe}^{\text{III}}$ -LTA, **K**: trehalose and **L**: cerium(III) nitrate. All concentrations are 100 ppm, except trehalose at 1000 ppm. The number of measurements,  $n$ , is indicated below each set of bars.

### 6.3.4 Growth rate measurements

Dihydrate crystals were grown at a supersaturation of 8% in the growth cell. Their growth rate was measured in the various crystal directions. These are the  $\langle 100 \rangle$ ,  $\langle 010 \rangle$  and the  $\langle 011 \rangle / \langle 11\bar{1} \rangle$  directions projected on the  $\{100\}$  plane. Because of the shape of the crystals and the view along the  $\langle 100 \rangle$  direction, we could not distinguish between the  $\langle 011 \rangle$  and  $\langle 11\bar{1} \rangle$  directions in situ, but these growth rates must be very similar because of the similar size of the  $\{011\}$  and  $\{11\bar{1}\}$  faces. The growth rates parallel to the  $(100)$  plane were determined directly from the crystal size. However, due to the view along the  $\langle 100 \rangle$  direction, the growth rate in that direction could not be observed directly. This growth rate was determined from the increase in size of the tilted side faces, the  $\{011\}$  and  $\{11\bar{1}\}$  faces.

Figure 6.9 shows the results for the growth rate of dihydrate crystals in the various crystal directions.  $v_{\langle 011 \rangle} = v_{\langle 11\bar{1} \rangle} = 0.14 \mu\text{m/s}$ ,  $v_{\langle 100 \rangle} = 0.10 \mu\text{m/s}$  and  $v_{\langle 100 \rangle} = 0.17 \mu\text{m/s}$ . These growth rates also show that the crystals are not plate-like at this supersaturation of 8%, in contrast to crystals grown at higher supersaturation.

Most of the tested anticaking agents and other impurities do not lower the growth rate of dihydrate crystals. Figure 6.9 shows that the growth rates in the various directions are not significantly influenced by most impurities. All growth rates were compared with the blank growth rates, using the Mann–Whitney U-test [23]. Only ferricyanide and Fe(III)–LTA lower the growth rate of dihydrate significantly in all three directions, by about 50 and 75% respectively. Cadmium(II) chloride significantly lowers the growth rate in the  $\langle 100 \rangle$  direction by 35% and cerium(III) nitrate significantly lowers the growth rate in the  $\langle 011 \rangle$  and  $\langle 11\bar{1} \rangle$  directions by 30%. Therefore, Fe(III)–LTA seems to be the best candidate for preventing caking of NaCl in freezing conditions.

However, as can be seen from the error bars in Figure 6.9, the spread in the data is quite large. This is partly an intrinsic property of the growth, since the growth rate of crystals measured simultaneously and very close to each other can vary a lot. This could be caused by differences in dislocation density between crystals. Another cause for the large spread are local variations in the supersaturation of the solution. This is due to a concentration gradient caused by other crystals depleting the growth solution and due to convection. The supersaturation is also influenced by the temperature gradient in the growth cell: the temperature is about 0.5 °C lower near the metal frame than in the centre of the cell, resulting in a variation of about 0.4% in supersaturation.

### 6.3.5 Nucleation rate experiments

#### Clean nucleation experiments

Figures 6.10a and b show the cumulative nucleation probability of dihydrate crystals observed for clean solutions at supersaturations of 5, 10 and 15%. As expected, nucleation occurs faster at higher

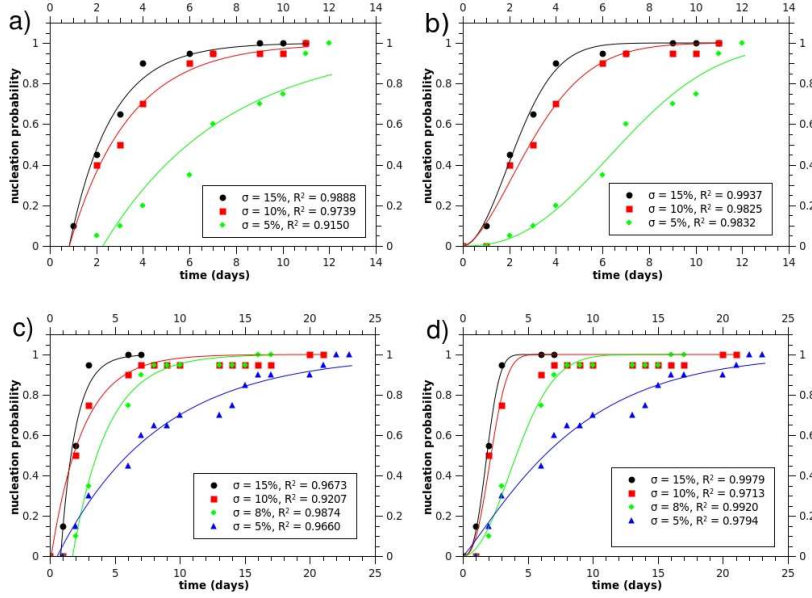


FIGURE 6.10: Nucleation rates of dihydrate crystals at various supersaturations. a) The data fitted with the kinetics predicted by the classical nucleation theory [24], in which the nucleation rate is independent of time. b) The data fitted by a cumulative Weibull distribution [25], where the nucleation rate can be fitted dependent of time. c) and d) Same analysis as in a and b, data taken from the experiment to determine the influence of disturbing the samples, but using only the undisturbed samples. In c, the data are fitted using equation 6.4, in d using equation 6.5.

$\sigma$	$J(d^{-1}l^{-1})$	$t_g$ (d)	$R^2$	$k$	$\lambda$ (d)	$R^2$	$\mu$ (d)	VAR (d)
5	$19 \pm 3$	$2.3 \pm 0.4$	0.9150	$2.4 \pm 0.2$	$7.9 \pm 0.2$	0.9832	7.0	3.1
10	$39 \pm 4$	$0.8 \pm 0.2$	0.9739	$1.7 \pm 0.2$	$3.6 \pm 0.2$	0.9825	3.2	1.9
15	$55 \pm 4$	$0.8 \pm 0.1$	0.9888	$1.9 \pm 0.2$	$2.8 \pm 0.1$	0.9937	2.5	1.4
5	$13 \pm 1$	$0.6 \pm 0.4$	0.9660	$1.2 \pm 0.1$	$8.6 \pm 0.3$	0.9794	8.1	6.8
8	$37 \pm 2$	$1.8 \pm 0.1$	0.9874	$2.1 \pm 0.2$	$4.9 \pm 0.2$	0.9920	4.3	2.2
10	$40 \pm 6$	$1.1 \pm 0.4$	0.9207	$2.5 \pm 0.5$	$2.5 \pm 0.1$	0.9713	2.2	0.9
15	$87 \pm 18$	$0.8 \pm 0.1$	0.9673	$2.7 \pm 0.2$	$2.1 \pm 0.1$	0.9979	1.9	0.7

TABLE 6.1: Results of fits to blank nucleation experiments in Figure 6.10, using equations 6.4 and 6.5. Top: first experiment at 5, 10 and 15% supersaturation. Bottom: data from unshaken experiment at 5, 8, 10 and 15% supersaturation. The parameters are explained in the text.

supersaturations. The mean nucleation time is very long in all cases, in the order of 2 – 8 days. Also the variation within each condition was quite large, in the order of 1 – 7 days.

In Figure 6.10a, the data are fitted using an equation derived from the classical nucleation theory assuming a constant nucleation rate, which describes the cumulative nucleation probability versus time [24]. This equation,

$$P(t) = 1 - \exp(-JV(t - t_g)), \quad (6.4)$$

in which  $P(t)$  is the cumulative nucleation probability,  $J$  is the nucleation rate in  $\text{d}^{-1}\text{l}^{-1}$ ,  $V$  the volume in litres,  $t$  the time in days and  $t_g$  the growth time in days before a crystal is identified by visual inspection. When fitting using equation 6.4, all zero values of the nucleation probability at the start of the experiments are ignored. Since the nucleation rate seems to increase with time, as can be seen from the "S-shape" in the data, the data are also fitted using the cumulative Weibull distribution [25],

$$P(t) = 1 - \exp\left(\frac{-t}{\lambda}\right)^k, \quad (6.5)$$

in which  $P(t)$  is the cumulative nucleation probability,  $k$  the shape parameter and  $\lambda$  the scale parameter. These fits are shown in Figure 6.10b. The fit parameters are given in Table 6.1. Equation 6.4 fits the data reasonably, however, equation 6.5 fits the data better in every case, as can be seen from the corresponding  $R^2$ -values. These fits suggest that the nucleation rate is increasing with time, since  $k > 1$  in all fits using equation 6.5.

From the fitting parameters  $k$  and  $\lambda$ , the mean and variance can be calculated, which are used to evaluate the fitting results. The mean value,  $\mu$ , which is the expectation value for the nucleation time, is given by

$$\mu = \lambda \Gamma\left(1 + \frac{1}{k}\right), \quad (6.6)$$

while the corresponding variance (VAR), representing the spread in the nucleation time around  $\mu$  within a data set, can be calculated using

$$\text{VAR} = \lambda^2 \Gamma\left(1 + \frac{2}{k}\right) - \mu^2, \quad (6.7)$$

in which  $k$  and  $\lambda$  are the fitting parameters from the Weibull distribution,  $t$  is again the time in days and  $\Gamma$  is the Gamma function. Since  $\mu$  corresponds to a mean nucleation time, it is approximately inversely related to the nucleation rate  $J$ .

The classical fit also gives an estimation of the growth time before detection,  $t_g$ . This value, ranging from 0.8 to 2.3 days, is not in agreement with the growth rates for dihydrate crystals which are of the order of 0.1 micrometer per second in each direction, as shown in Figure 6.9: a crystal of detectable size (1 – 2 millimetres) would take about 1.5 – 3 hours to form. Almost in all cases, quite large crystals were detected of 5 – 20 mm, having completely depleted the supersaturation, so nucleation must have occurred in between the observation moments. Thus the resulting growth time  $t_g$  should have been approximately 0.5 days, due to the observation interval of one day.

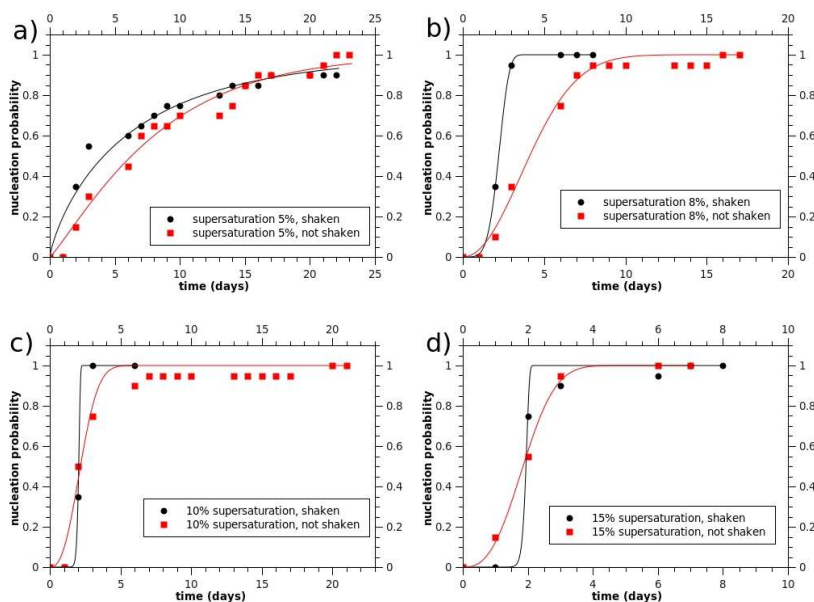


FIGURE 6.11: The influence of shaking the vials vigorously after each observation moment, at different supersaturations. The corresponding fitting parameters are given in Table 6.2.

condition	$k$	$\lambda$ (d)	$R^2$	$\mu$ (d)	VAR (d)
$\sigma = 15\%$ , shaken	$24 \pm 9.2$	$2.0 \pm 10$	0.9900	2.0	0.1
$\sigma = 15\%$ , not shaken	$2.7 \pm 0.2$	$2.1 \pm 0.1$	0.9979	1.9	0.7
$\sigma = 10\%$ , shaken	$21 \pm 1$	$2.1 \pm 0.1$	1.0000	2.0	0.1
$\sigma = 10\%$ , not shaken	$2.5 \pm 0.5$	$2.5 \pm 0.1$	0.9713	2.2	0.9
$\sigma = 8\%$ , shaken	$4.8 \pm 0.1$	$2.4 \pm 0.1$	0.9998	2.2	0.5
$\sigma = 8\%$ , not shaken	$2.1 \pm 0.2$	$4.9 \pm 0.2$	0.9920	4.3	2.2
$\sigma = 5\%$ , shaken	$0.8 \pm 0.1$	$6.5 \pm 0.5$	0.9541	7.4	9.3
$\sigma = 5\%$ , not shaken	$1.2 \pm 0.1$	$8.6 \pm 0.3$	0.9794	8.1	6.8

TABLE 6.2: *fitting parameters corresponding to the fits shown in Figure 6.11, showing the influence of disturbing the solutions*

The influence of disturbing the solutions was investigated in order to explain the long nucleation times. However, the data from the undisturbed vials were also used to check the reproducibility of the nucleation experiment. They were fitted using equations 6.4 and 6.5 and are given in 6.10c and d, while the fitting parameters are given in Table 6.1. Again, equation 6.5 fits the data better than equation 6.4, as can be seen from the corresponding  $R^2$ -values. Also, the growth times  $t_g$  are again in disagreement with our observations. Therefore, further data are only fitted using equation 6.5. The shape parameter  $k$  resulting from the fit using equation 6.5 is again larger than 1 in all cases, indicating that the nucleation rate is really increasing with time.

### Nucleation rate in disturbed solutions

Figure 6.11 shows the influence of disturbing (i.e. shaking) the solutions after each observation, compared to handling the solutions as carefully as possible. The data are fitted using equation 6.5. In the disturbed solutions, the shape parameter  $k \gg 1$  at 8, 10 and 15% supersaturation. The data from these experiments cannot be properly fitted using equation 6.4. Only at 5% supersaturation,  $k < 1$ , so the nucleation rate does not increase with time in this case, though the quality of this fit is poor ( $R^2 = 0.9541$ ).

From the fitting results it can be seen that disturbing the solutions does not increase the nucleation rate effectively. Only at 8% supersaturation the nucleation rate increases, almost by a fac-

tor 2. However, the variance of the data is decreased significantly, except at 5% supersaturation. Overall, the influence of disturbing the solutions on the nucleation rate is limited, and therefore the long nucleation times and the time dependence of the nucleation rate cannot be explained by it.

### The influence of the observation intervals

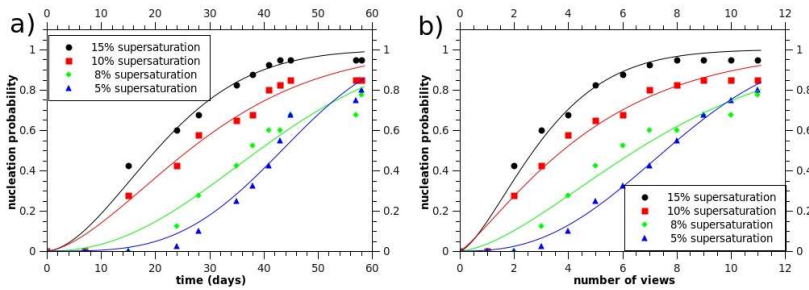


FIGURE 6.12: The influence of varying the observation intervals (1 – 12 days). a) The nucleation probability plotted as a function of time. b) The nucleation probability as a function of the number of observations. It is clear that the nucleation time is greatly increased, compared to the nucleation experiment shown in Figure 6.10. However, when plotted as a function of observations, the difference is much smaller.

$\sigma$	time						views				
	$k$	$\lambda$	$R^2$	$\mu$	VAR		$k$	$\lambda$	$R^2$	$\mu$	VAR
15	$1.7 \pm 0.2$	$25 \pm 1$	0.9836	22	14		$1.5 \pm 0.2$	$3.5 \pm 0.2$	0.9750	3.2	2.1
10	$1.6 \pm 0.2$	$33 \pm 1$	0.9783	30	19		$1.2 \pm 0.1$	$5.2 \pm 0.2$	0.9741	4.9	4.1
8	$2.2 \pm 0.3$	$46 \pm 2$	0.9574	41	20		$1.6 \pm 0.2$	$8.2 \pm 0.3$	0.9661	7.4	4.7
5	$3.4 \pm 0.4$	$48 \pm 1$	0.9645	43	14		$2.5 \pm 0.1$	$8.8 \pm 0.1$	0.9947	7.8	3.3

TABLE 6.3: The fitting parameters from the fits to the data in Figure 6.12, using equation 6.5. Fitting to the data as a function of time results in acceptable fit quality. Fitting to the data as a function of views also gives acceptable fit qualities, with nucleation "times" more comparable to those in Table 6.1.

Figure 6.12 shows the results from the experiment in which the interval between observations has been varied in order to study its influence. The data are plotted as a function of time (Figure 6.12a) and as a function of the amount of views (Figure 6.12b). Equation 6.5 is fitted to the data, in Table 6.3 the resulting fit parameters are given. Both methods of fitting result in good fit qualities, however, at low supersaturation the fit quality is better when plotted as a function of views.

It can also be seen that increasing the time between observations greatly increases the nucleation time, since the mean values ( $\mu$ ) are much higher when plotted as a function of time than in the corresponding experiments in Figure 6.10, and when the data are plotted as a function of views. So viewing the vials speeds up nucleation, even though it is not caused by disturbing the solutions, as was concluded from the shaking experiments (Figure 6.11). Therefore, we propose that nucleation is inhibited by some metastable prenucleation phase. This phase hinders the subsequent nucleation of dihydrate crystals, by increasing the nucleation barrier and/or by lowering the effective supersaturation, as is illustrated in Figure 6.13.

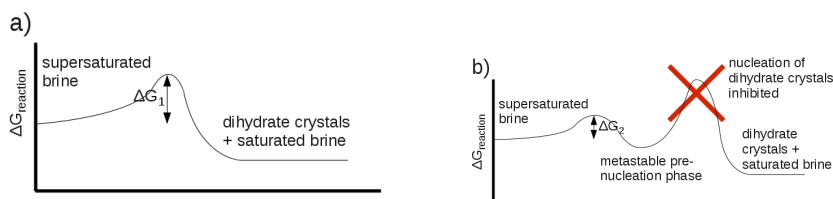


FIGURE 6.13: a) The classical energy diagram for crystal nucleation with a single energy barrier between the supersaturated solution and the dihydrate crystalline phase. b) The energy diagram for nucleation with a nucleation inhibiting prenucleation phase. This phase would explain the long nucleation times as well as the time dependence of the nucleation rate. The activation barrier for the classical route is larger than that of the first step in the two-step model ( $\Delta G_1 > \Delta G_2$ ).

The unusually long nucleation times could be explained by the presence of a nucleation inhibiting prenucleation phase. Also, such a phase could explain the observation that the nucleation time depends on the interval between observations, as well as the time dependence of the nucleation rate. If such a phase is present, it would consume the supersaturation available for nucleation, thereby hindering the formation of dihydrate crystals. It could also explain the time dependence of the nucleation rate, since checking the vials for crystals raises the temperature in the vials by 6 – 7 °C. This temperature change could dissolve the prenucleating phase, giving the system a new chance on nucleating dihydrate crystals, for instance, via the classical route (Figure 6.13a). In this way, also the

dependence of the nucleation rate on the interval between views would be explained.

The prenucleation phase could be a densified liquid phase by liquid–liquid separation, or a nanocrystalline phase which cannot grow out to macroscopic size. However, it cannot be the anhydrous form of sodium chloride (normal NaCl), since the solutions at 5%, 8% and 10% supersaturation (for the dihydrate) are undersaturated for the anhydrous form. The existence of prenucleation phases in crystal nucleation, also known as the two-step nucleation model, has been shown previously in protein and other macromolecular systems [26, 27]. More recently such phases have also been detected in the crystallisation of small organic molecules and therefore, the two-step nucleation mechanism may underlie many crystallisation processes from solution [28]. However, in this case the prenucleation phase is not followed by nucleation, probably because it is too stable, and therefore it inhibits nucleation. The presence of such a phase should be investigated further, using an in-situ technique.

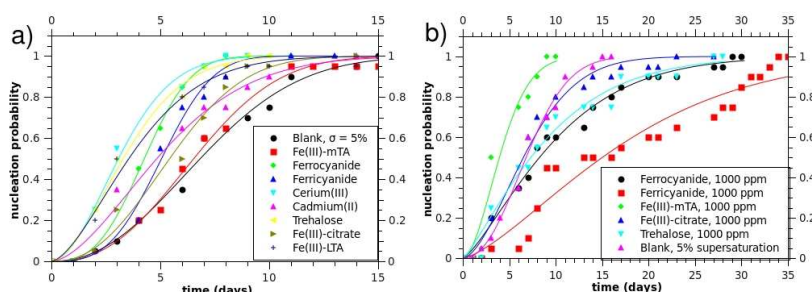


FIGURE 6.14: Nucleation rates of dihydrate crystals in presence of various additives; supersaturation is 5% in all cases. a) Additive concentration 100 ppm. b) Additive concentration 1000 ppm.

### Nucleation rate in presence of additives

Figure 6.14 shows the influence of several additives on the nucleation of dihydrate crystals at 100 and 1000 ppm and at a supersaturation of 5%, including the clean nucleation rate at 5% supersaturation for reference (from Figure 6.10b). The corresponding

Additive	$k$	$\lambda$ (d)	$R^2$	$\mu$ (d)	VAR (d)
Ferrocyanide 1000 ppm	$1.3 \pm 0.1$	$10.9 \pm 0.3$	0.9872	10.1	7.8
Ferricyanide 1000 ppm	$1.4 \pm 0.1$	$19 \pm 0.1$	0.9483	17.3	12.5
Fe(III)–mTA 1000 ppm	$1.8 \pm 0.3$	$4.8 \pm 0.4$	0.9650	4.3	2.5
Fe(III)–citrate 1000 ppm	$1.7 \pm 0.2$	$8.1 \pm 0.3$	0.9823	7.2	4.4
Trehalose 1000 ppm	$1.2 \pm 0.1$	$9.8 \pm 0.4$	0.9770	9.2	7.7
Ferrocyanide 100 ppm	$2.9 \pm 0.1$	$4.8 \pm 0.1$	0.9994	4.3	1.6
Ferricyanide 100 ppm	$3.1 \pm 0.4$	$5.7 \pm 0.1$	0.9861	5.1	1.8
Fe(III)–mTA 100 ppm	$2.5 \pm 0.2$	$7.6 \pm 0.2$	0.9915	6.7	2.9
Fe(III)–citrate 100 ppm	$2.3 \pm 0.3$	$6.4 \pm 0.2$	0.9889	5.7	2.6
Fe(III)–LTA 100 ppm	$1.6 \pm 0.1$	$4.5 \pm 0.2$	0.9867	4.0	2.6
Trehalose 100 ppm	$1.8 \pm 0.2$	$4.1 \pm 0.2$	0.9898	3.6	2.1
Cerium(III) Nitrate	$1.8 \pm 0.2$	$3.8 \pm 0.2$	0.9886	3.4	1.9
Cadmium(II) Chloride	$1.7 \pm 0.2$	$6.0 \pm 0.2$	0.9860	5.4	3.2
Blank, $\sigma = 5\%$	$2.4 \pm 0.2$	$7.9 \pm 0.2$	0.9832	7.0	1.4

TABLE 6.4: The fitting parameters resulting from fitting equation 6.5 to the nucleation rate data for additives added at 100 and 1000 ppm to a growth solution at 5% supersaturation, shown in Figure 6.14.

fit parameters, using equation 6.5, are given in Table 6.4, also including the corresponding clean nucleation experiment at 5% supersaturation (from Table 6.1, line 1). From the data it can be concluded that at 100 ppm all tested additives either slightly increase the nucleation rate or have no significant influence. At 1000 ppm, Fe–mTA increases the nucleation rate of the dihydrate crystals, while Ferricyanide delays the nucleation somewhat, though the quality of this fit is rather poor. The other additives have no significant influence on the nucleation rate at this concentration. Even though Ferricyanide may inhibit nucleation of dihydrate crystals somewhat, nucleation inhibition may therefore not be a feasible method to prevent caking of NaCl at low temperatures.

## 6.4 Conclusion

The crystal structure of sodium chloride dihydrate crystals was checked and it was shown that these crystals are formed on top of NaCl crystals under freezing conditions. Therefore, it is very likely that the strong tendency for caking of NaCl powders at low temperatures is caused by the formation of dihydrate crystals, forming solid bridges between NaCl particles.

A method was developed to grow dihydrate crystals while observing them using the microscope, resulting in clear pictures of nicely faceted crystals during growth. This method allowed the determination of the morphology of these crystals, using the crystal structure and symmetry. It also allowed measurements of the growth rate of these crystals in various directions. We investigated the influence of anticaking agents and other additives on the growth rate, resulting in a candidate for anticaking of sodium chloride at freezing temperatures: Fe(III)–LTA.

Finally, the nucleation behaviour of dihydrate crystals was investigated. The nucleation rate was found to be extremely low and also found to increase with time. This is possibly caused by the formation of a nucleation inhibiting metastable prenucleation phase. This phase explains the dependence of the nucleation rate on time as well as on the solution temperature increase during inspection of the crystals. In the latter case, the prenucleation phase dissolves, which allows the nucleation of dihydrate crystals. This hypothesis requires further investigation. Additives were found to have a limited effect on the nucleation rate. Fe(III)-mTA was found to increase the nucleation rate, whereas Ferricyanide delays the nucleation of dihydrate crystals.

## Acknowledgement

We would like to acknowledge Akzo Nobel Industrial Chemicals and the Dutch Ministry of Economic Affairs for funding (EOS–KTO program, AgentschapNL).

## References

- [1] D.W. Kaufmann. *Sodium Chloride: the production and properties of salt and brine*. Reinhold, (1960).
- [2] M.A. van Damme-van Weele. *Influence of additives on the growth and dissolution of sodium chloride crystals*. PhD thesis, Technische Hogeschool Twente, Enschede, (1965).

- [3] R.M. Geertman. Use of carbohydrate-based metal complexes in non-caking salt compositions. US patent WO 00/59828, (2006).
- [4] Y.L. Chen and J.Y. Chou. *Powder Technol.*, (1993), **77**, 1–6.
- [5] A.A.C. Bode, V. Vonk, D.J. Kok, F.J. van den Bruele, A. Kerkenaar, M. Mantilla, S. Jiang, J.A.M. Meijer, W.J.P. van Enkevort, and E. Vlieg. *Cryst. Growth Des.*, (2012), **12**, 1919–1924.
- [6] A.A.C. Bode, S. Jiang, J.A.M. Meijer, W.J.P. van Enkevort, and E. Vlieg. *Cryst. Growth Des.*, (2012), **12**, 5889–5896.
- [7] V. Novotny, D. Muehring, D.H. Zitomer, D.W. Smith, and R. Facey. *Water Sci. Technol.*, (1998), **38**, 223–230.
- [8] A.N. Winchell and H. Winchell. *The microscopic characters of artificial inorganic solid substances: optical properties of artificial minerals*. Academic Press, New York, (1964).
- [9] B. Klewe and B. Pedersen. *Acta Cryst. B*, (1974), **30**, 2363–2371.
- [10] T.G. Zijlema, R.J.A.J. Hollman, G.J. Witkamp, and G.M. van Rosmalen. *J. Crystal Growth*, (1999), **198–199**, 7890795.
- [11] B. Light, R.E. Brandt, and S.G. Warren. *J. Geophys. Res.*, (2009), **114**, C07018.
- [12] T. Kottke and D. Stalke. *J. Appl. Crystallogr.*, (1993), **26**, 615–619.
- [13] A.M.M. Schreurs, X. Xian, and L.M.J. Kroon-Batenburg. *J. Appl. Crystallogr.*, (2010), **43**, 70–82.
- [14] G.M. Sheldrick. *SADABS*. University of Göttingen, Germany, (2008).
- [15] G.M. Sheldrick. *Acta Crystallogr. A*, (2008), **64**, 112–122.
- [16] A.L. Spek. *Acta Crystallogr. D*, (2009), **65**, 148–155.
- [17] I. Shweky, A. Bino, D.P. Goldberg, and S.J. Lippard. *Inorg. Chem.*, (1994), **33**, 5161–5262.

- [18] X. Hao, Y. Wei, and S. Zhang. *Transit. Met. Chem.*, (2001), **26**, 384–387.
- [19] A.A.C. Bode, S.J.C. Granneman, M.C. Feiters, P. Verwer, J.A.M. Meijer, W.J.P. van Enkevort, and E.Vlieg. Manuscript in preparation.
- [20] V. Ragoonanan, T. Wiedmann, and A. Aksan. *J. Phys. Chem. B*, (2010), **114**, 16752–16758.
- [21] J.W. Mullin and K.D. Raven. *Nature*, (1961), **190**, 251.
- [22] E. Dowty. Shape for windows professional edition, (1999).
- [23] F. Wilcoxon. *Biometrics Bull.*, (1945), **1**, 80–83.
- [24] S. Jiang and J.H. ter Horst. *Cryst. Growth Des.*, (2011), **11**, 256–261.
- [25] G.W. Weibull. *J. Appl. Mech*, (1951), **18**, 293–297.
- [26] Y.G. Kuznetsov, A.J. Malkin, and A. McPherson. *J. Cryst. Growth*, (2001), **232**, 30–39.
- [27] P.G. Vekilov. *Cryst. Growth Des.*, (2004), **4**, 671–685.
- [28] D. Erdemir, A.Y. Lee, and A.S. Myerson. *Accounts Chem. Res.*, (2009), **42**, 621–629.



## Chapter 7

# Summary

Anticaking agents are additives which prevent the agglomeration of a crystalline material into lumps, a process called caking. However, how they prevent caking is not known. In general, it is assumed that they inhibit crystal growth, thereby preventing solid bridge formation and thus caking. In this work, we investigate how anticaking agents work in more detail, using sodium chloride as a model system.

In chapter 2 surface X-ray diffraction is applied to show how the ferrocyanide ion adsorbs onto the surface of the sodium chloride crystal. It replaces a sodium ion and five surrounding chloride ions. We propose that because of the charge of the ferrocyanide ions adsorbed on the surface, the crystal can only continue growing by leaving a sodium vacancy, or by desorption of the ferrocyanide ion. As a consequence, the ferrocyanide ion blocks further growth of the crystals, thereby preventing caking.

In the third chapter, we show how the growth of sodium chloride crystals is inhibited by the anticaking agents ferrocyanide and iron(III) *meso*-tartaric acid. Using in-situ atomic force microscopy, it is shown how steps flow on clean crystals and how the step flow is inhibited by the anticaking agents. At sub-monolayer coverages, steps are temporarily pinned, while at higher coverages, no step movement is observed at all.

In chapter 4 the structure of the anticaking agent iron(III) *meso*-tartrate is discussed, as well as its interaction with the crystal surface. We derive its molecular structure using experimental techniques as well as molecular modelling. We show that the active complex is a binuclear iron(III) complex with two bridging *meso*-tartrate ligands. In solution, a water molecule coordinates to each iron atom. Probably this water molecule can be replaced when the complex adsorbs on the sodium chloride crystal surface. This adsorption results in step pinning, which in turn explains the anticaking activity of the iron(III) *meso*-tartrate complex.

Chapter 5 describes the effectivity of anticaking agents at a larger length scale compared to the preceding chapters. The anticaking agents ferrocyanide, ferricyanide and iron(III) *meso*-tartaric acid were studied at the powder scale and on a two-crystal scale. Results at the powder scale agree well with industrial experience with these anticaking agents, while at the two-crystal scale higher dosages of anticaking agents are required to prevent caking. This is caused by an increase in the number of contact points due to a change in surface morphology, which is in turn caused by the applied anticaking agents. Therefore it is not only the surface area but also the number of contact points, and thus the particle size distribution, which are critical in determining the optimal dosage of anticaking agents.

The final chapter focuses on the caking of sodium chloride at low temperatures, which is caused by the formation of solid bridges of sodium chloride dihydrate in between the powder particles. Using the crystal structure, the morphology of the dihydrate crystals was determined. Also the growth rate of these crystals was determined, as well as the influence of anticaking agents on the growth rate. A likely candidate for the inhibition of dihydrate growth was found: iron(III) *L*-tartaric acid. In addition, the nucleation behaviour of dihydrate crystals was investigated. The nucleation rate was found to be extremely low and to increase with time. This is probably caused by the formation of a metastable prenucleation phase, which inhibits the nucleation of dihydrate crystals. The influence of the same additives on the nucleation rate was found to be limited.

## Hoofdstuk 8

# Samenvatting

Antiklontermiddelen zijn stoffen die voorkomen dat kristallijne materialen klonteren. Echter, het is niet goed bekend hoe dat werkt. In het algemeen wordt aangenomen dat antiklontermiddelen de kristalgroei afremmen, waardoor er geen vast materiaal kan neerslaan tussen de kristallen. Dan ontstaan er geen vaste verbindingen tussen de kristallen en wordt het klonteren van het materiaal voorkomen. In dit proefschrift achterhalen we in meer detail hoe deze antibakmiddelen werken, met natriumchloride als modelsysteem.

In hoofdstuk 2 is oppervlakte röntgendiffractie toegepast om te laten zien hoe het antiklontermiddel ferrocyanide adsorbeert op het oppervlak van natriumchloride. Het vervangt een natriumion en vijf omringende chloride-ionen. Op basis hiervan stellen wij voor dat het de lading van het ferrocyanide ion is waardoor het kristal niet verder kan groeien, tenzij er een natriumvacature ontstaat of het ferrocyanide-ion desorbeert. Op deze manier blokkeert het ferrocyanide-ion de groei van het kristal en wordt klonteren voorkomen.

In het derde hoofdstuk laten we zien hoe de groei van natriumchloridekristallen wordt geblokkeerd door de antiklontermiddelen ferrocyanide en ijzer(III) *meso*-wijnsteenzuur. Er is gebruik gemaakt van atomaire krachtmicroscopie om te laten zien hoe stapranden zich over het oppervlak van schone kristallen voortbewegen

en hoe dit wordt afgeremd door de antiklontermiddelen. Bij bedekkingen van minder dan één monolaag worden de stapranden tijdelijk vastgezet. Bij hogere bedekkingsgraden staan de stapranden volledig stil en vindt er geen groei plaats.

In hoofdstuk 4 wordt de structuur van het nieuwe antiklontermiddel, ijzer(III) *meso*-wijnsteenzuur, besproken, evenals de interactie van dit molecuul met het zoutoppervlak. De moleculaire structuur van het antiklontermiddel is achterhaald met experimentele technieken en moleculaire modellering. Hiermee is bepaald dat het molecuul een binucleair ijzer(III) complex is met twee bruggende *meso*-wijnsteenzuur liganden. De ijzeratomen zijn antiferromagnetisch gekoppeld. In de oplossing coördineert één watermolecuul aan elk ijzeratoom. Waarschijnlijk kan dit watermolecuul verwijderd worden als het complex adsorbeert aan het zoutoppervlak. Het geadsorbeerde molecuul hindert de verplaatsing van stapranden, wat de antiklonterwerking van dit molecuul verklaart.

Hoofdstuk 5 beschrijft de effectiviteit van antiklontermiddelen op een grotere lengteschaal dan in de voorgaande hoofdstukken. In dit hoofdstuk wordt de invloed van de antiklontermiddelen ferrocyanide, ferricyanide en ijzer(III) *meso*-wijnsteenzuur onderzocht op het klonteren van een poeder en op het samenklonteren van twee kristallen. De resultaten met het poeder komen goed overeen met de ervaringen met deze middelen in de industrie. Om het aan elkaar klonteren van twee kristallen te voorkomen zijn hogere doseringen antiklontermiddel nodig dan normaal. Dit wordt veroorzaakt door een toename van het aantal contactpunten tussen de kristallen, wat op zijn beurt wordt veroorzaakt door de antibakmiddelen zelf. Hieruit blijkt dat niet alleen de hoeveelheid oppervlak, maar ook het aantal contactpunten en dus ook de deeltjesgrootteverdeling belangrijk zijn voor het bepalen van de juiste dosering antiklontermiddel.

Het laatste hoofdstuk gaat in op het klonteren van natriumchloride bij lage temperaturen, wat wordt veroorzaakt door de vorming van natriumchloride dihydraat, dat vaste bruggen vormt tussen de poederdeeltjes. Vanuit de kristalstructuur is de morfologie van de

dihydraatkristallen bepaald. Ook de groeisnelheid en de invloed van antiklontermiddelen hierop is bepaald. Een mogelijke kandidaat voor het voorkomen van klonteren bij lage temperatuur is gevonden: ijzer(III) *L*-wijnsteenzuur. Daarnaast is ook aandacht besteed aan de nucleatie van de dihydraatkristallen. De nucleatiesnelheid is extreem laag en neemt toe in de tijd. Dit wordt waarschijnlijk veroorzaakt door de vorming van een metastabiele prenucleatiefase die de nucleatie van dihydraatkristallen hindert. De invloed van antiklontermiddelen op de nucleatiesnelheid van dihydraat is gering.



## Hoofdstuk 9

# Dankwoord

Na vier jaar werken op de afdeling Vaste Stof Chemie (het leek zoveel langer), zijn er heel wat figuren de revue gepasseerd. Enorm veel mensen hebben in die tijd een grote of wat kleinere bijdrage geleverd aan het tot stand komen van dit proefschrift. Ondanks dat ik mijn best doe, zit de kans er natuurlijk in dat ik iemand zal vergeten, bij voorbaat excuses daarvoor.

Als eerste gaat mijn dank uit naar mijn promotor, **Elias**. Dank je wel voor het vertrouwen dat je mij gaf door mij de kans te geven dit onderzoek te doen. Je liet me zeer vrij om mijn onderzoek zelf in te richten, maar wanneer er sturing nodig was, dan stond je deur altijd open. Voornamelijk als het ging over je grote liefde, oppervlakediffractie, heb je me erg veel geholpen.

Daarnaast had ik het geluk om ook nog de hulp te hebben gehad van twee copromotores. **Willem**: goeroe als het gaat om kristalgroei, maar ook extreem handig met microscopen en direct enthousiast als je een mooi glimmend kristalletje hebt! Dank je voor alle ondersteuning. **Jan Meijer**: op iets meer afstand maar niet minder belangrijk was jouw ondersteuning. Van jou en bij Akzo leerde ik veel over de industriële kant van het vak. Je hielp enorm bij het vertalen van academische abstractie naar industrieel nut. Het heeft zeker geholpen om mijn onderzoek ook nog een beetje nuttig te houden.

Onmisbaar was de handigheid van onze technicus **Jan van Kessel**, manusje van alles. Ook **Erik**, je hebt Jan zo goed opgevolgd, het zou ons Jan bijna volledig doen vergeten! **Wiesiek**, altijd behulpzaam als er iets gemaakt moest worden, en natuurlijk toen ik de AFM weer (definitief) gesloopt had...**Elizabeth**, dank je voor het handhaven van de koffie- en vooral taartdiscipline binnen de afdeling! En alle andere bijdragen die je geleverd hebt. **Hugo**, altijd in het donker maar altijd behulpzaam bij thermodynamische vraagstukken, maar ook als ik een kabeltje miste of een zekering nodig had. Daarnaast wil ik **René de Gelder** en **Jan Smits** bedanken voor hun hulp bij de poederdiffractie en structuurbepalingen.

In vier jaar tijd zijn er een boel collega's gekomen en weer gegaan. **Wim**, bedankt voor je enthousiaste begeleiding tijdens mijn stages, dankzij jou ben ik überhaupt gaan promoveren! Ik kan "The Big Lebowski" niet meer kijken zonder aan m'n stage terug te denken... **Paul Tinnemans**, **Vedran**, **Rienk**, **Fieke** en **Wester**: bedankt voor de vele potjes tafelfootbal, hopelijk wordt het tafelfootbalopleidingsinstituut in ere gehouden. **Alaa**, **René**, **Laura**, **Rita** en **Eline**, jullie waren wat minder te porren voor het sportieve intermezzo, maar bedankt voor alle interessante discussies aan de koffietafel en daarbuiten. Vedran en Fieke wil ik daarnaast nog extra bedanken voor de vele uren hulp tijdens (en na) bundeltijd, gelukkig heeft het succes opgeleverd in hoofdstuk 2.

Daarnaast wil ik de collega's van AMS niet onvernoemd laten: **Paul Hageman**, **John**, **Gerbe**, **Günther**, **Niek**, **Tim**, **Jon** en alle **technici**, bedankt voor de gezelligheid tijdens de gemeenschappelijke activiteiten.

Verder wil ik graag **Jan Gerretsen** bedanken voor alle hulp met de AFM, **Martin Lutz** voor de structuurbepaling van het dihydraat, **Martin Feiters** voor de hulp met de structuurbepaling van het mTA, **Paul Schlebos** en **Bas de Bruin** voor de EPR spectra en **Jelle Eygensteyn** voor ICP-MS metingen.

Als laatste wil ik alle mensen van AKZO-Nobel met wie ik heb samengewerkt bedanken. **Maartje Steendam**, **Sjanfeng Jiang** en **Henk Bakkenes** voor de vele discussies. **Martin Jansen** voor de samenwerking met de caking-proeven, **Paul Verwer** voor de

computersimulaties van het mTA-complex, **Kees van Leerdam** voor de samenwerken met de ToF-SIMS experimenten; hopelijk wordt dit project nog voortgezet en **Ed de Jong** en **Jurjen ter Maat** voor de discussies rond wegzout en dihydraat.

Natuurlijk mogen ook alle studenten die zo gek zijn geweest bij mij stage te willen lopen niet onvernoemd blijven. **Sanne Granne-man**, zowel in je bachelorstage als in je masterstage heb je erg nuttig werk (zie hoofdstuk 4) gedaan en bijzonder veel werk verzet. Bedankt daarvoor! **Dirk**, jij was mijn eerste student en hebt veel verkennende proeven gedaan en natuurlijk bedankt voor je bijdrage aan het diffractie-experiment in Karlsruhe (hoofdstuk 2). **Ward**: ondanks tegenslagen (dihydraat is lastiger te groeien dan we dachten) heb je wel de aanzet gegeven voor het succes (hoofdstuk 6) in dit project! En **Melvin**, jij kan bijzonder goed doen alsof je weinig doet en stiekem erg goed bezig zijn... Zo goed als al het werk aan hoofdstuk 5 is van jouw hand. **Jorien**, bedankt voor jouw bijdrage. **Paul Pulles**: jij hebt laten zien dat een korte stage toch bijzonder nuttig kan zijn! Als laatste wil ik **Anne Kerkenaar** nog bedanken voor haar hulp bij het diffractie-experiment in Grenoble, wat uiteindelijk mocht leiden tot hoofdstuk 2, en natuurlijk **alle overige stage-studenten** die in die vier jaar gepasseerd zijn. Allemaal hebben jullie een steentje bijgedragen aan de prettige sfeer en de fijne koffie- en lunchpauzes. En niet te vergeten bij de studenten-AIO-postdoc-etentjes.

Gelukkig is er meer in het leven dan werk, zelfs tijdens een promotietraject. Ik had het geluk om te beschikken over een brede vriendenkring, vrienden die me gedurende die tijd ondersteund, afgeleid en vermaakt hebben. Natuurlijk de vaste club mensen van de falafel-etentjes: **Joep & Minke**, **Marijn & Lieke**, **Frans**, **Pim Tempelaars & Elisa**, **Pim van der Asdonk**, **Lisa & Sven**, **Roel** en **Peter**. Bedankt voor de gezelligheid, en natuurlijk de lunches bij Theo!

Ook wil ik graag **Alex & Brenda**, **Linda & Roman** en **Inge & Richard** bedanken voor de vele etentjes en stapavonden en **Yael & Giovanni**, **René** en **Corine** voor de vele bezochte festivals, carnavals en stapavonden. **Dirk**, bedankt voor de lange vriendschap sinds ergens op de basisschool en ook voor de vele fijne avonden

en nachten in Eindhoven. **Arne & Angela**, ook bedankt voor de etentjes en stapavonden.

Als laatste maar zeker niet het minste zijn er nog de vrienden die al sinds de middelbare school meegaan: **Eric & Yu-Chia**, **Merlijn & Martine**, **Stefan & Emma** en **Marcel & Maresa**. Dank jullie wel voor de leuke vakanties, het mannenweekend, de Utrechtse stapavonden en de FIFA-avonden. En extra wil ik **Alex en Dirk** bedanken omdat jullie vandaag mijn paranimfen willen zijn!

Vrienden zijn fijn, maar zonder een goede basis ben je nergens. En die basis is toch je familie. In de eerste plaats wil ik mijn ouders, **Geert** en **Hannie**, bedanken voor de fijne jaren en de goede opvoeding. Ook mijn zussen, **Renske** en **Nienke**, moet ik zeker noemen. Ondanks dat ik jullie niet vaak genoeg zie, zijn jullie beide enorm belangrijk voor mij! En natuurlijk **Jeroen** en **Bernard**, omdat jullie mijn zussen gelukkig maken! Ook tante **Paulien**, **Eric** en **Marloes** en alle ooms, tantes, neven en nichten van de Vinken wil ik bedanken voor de interesse in mij en wat ik doe. Verder voelt de familie Meeuwissen ondertussen als familie. **Henri**, **Els**, **Esther** en **Jurrian**, bedankt voor jullie interesse in mij en in mijn onderzoek.

Als slot blijf jij over, **Silvie**, en zeker niet op de minste plek. Dankzij jou ben ik überhaupt afgestudeerd, jij bent al jaren mijn motivatie én mijn discipline. Jij bent mijn drijfveer en kompas, elke dag weer, dankjewel voor alles!

## Chapter 10

# List of Publications

- W.L. Noorduin, H. Meekes, A.A.C. Bode, W.J.P. van Enckevort, B. Kaptein, R.M. Kellogg and E. Vlieg, “Explanation for the Emergence of a Single Chiral Solid State during Attrition–Enhanced Ostwald Ripening: Survival of the Fittest”, *Crystal Growth and Design* **2008**, *8*, 1675–1681
- W.L. Noorduin, A.A.C. Bode, M. van der Meijden, H. Meekes, A.F. van Etteger, W.J.P. van Enckevort, P.C.M. Christianen, B. Kaptein, R.M. Kellogg, Th. Rasing and E. Vlieg, “Complete Chiral Symmetry Breaking of an Amino Acid Derivative by Circularly Polarised Light”, *Nature Chemistry*, **2009**, *1*, 729–732
- W.L. Noorduin, P. van der Asdonk, A.A.C. Bode, H. Meekes, W.J.P. van Enckevort, E. Vlieg, B. Kaptein, M.W. van der Meijden, R.M. Kellogg and G. Deroover, “Scaling Up Attrition–Enhanced Deracemization by Use of an Industrial Bead Mill in a Route to Clopidogrel (Plavix)”, *Organic Process Research and Development*, **2010**, *14*, 908–911
- R.E. Algra, M.A. Verheijen, L.F. Feiner, G.G.W. Immink, W.J.P. van Enckevort, A.A.C. Bode, W.L. Noorduin, E. Tancredi, A.E.F. de Jong, E.P.A.M. Bakkers and E. Vlieg, “Formation of Wurtzite InP Nanowires Explained by Liquid–Ordering”, *Nano Letters*, **2011**, *11*, 1259–1264

- A.A.C. Bode, V. Vonk, F.J. van den Bruele, D.J. Kok, A.M. Kerkenaar, M.F. Mantilla, S. Jiang, J.A.M. Meijer, W.J.P. van Enkevort and E. Vlieg, “Anticaking Activity of Ferrocyanide on Sodium Chloride Explained by Charge Mismatch”, *Crystal Growth and Design* **2012**, *12*, 1919–1924
- A.A.C. Bode, S. Jiang, J.A.M. Meijer, W.J.P. van Enkevort and E. Vlieg, “Growth Inhibition of Sodium Chloride Crystals by Anticaking Agents: In Situ Observation of Step Pinning”, *Crystal Growth and Design*, **2012**, *12*, 5889–5896

## Chapter 11

# Curriculum Vitae

Name:	Arno Alfred Christiaan Bode
Date of birth:	12 December 1981
1994-2000:	Secondary school "Lorentz Casimir Lyceum", Eindhoven
2000-2001:	Study Architecture at Technical University Eindhoven, discontinued
2001-2004:	Study Physics at Radboud University Nijmegen, discontinued
2004-2009:	Study Chemistry at Radboud University Nijmegen, Cum Laude
Bachelor Thesis Subject	Solid State Chemistry <i>"Complete chiral purity through enhanced Ostwald Ripening"</i>
Master Thesis Subject	Solid State Chemistry <i>"Breaking Chiral symmetry and amplifying chiral asymmetry and Polymorph steering using grinding techniques: inverting Ostwald's Rule of Stages"</i>

- 2009-2013: PhD research at Radboud University Nijmegen at the department of Solid State Chemistry
- Subject *“The Mechanism of Anticaking Agents for Sodium Chloride”*
- Supervisors Prof. Dr. E. Vlieg, Dr. W.J.P. van Enckevort and Dr. J.A.M. Meijer
- 2013 – Scientist Solid State at MSD/Aspen Pharmacare, Oss